PONTIFICIA UNIVERSIDAD CATÓLICA DE CHILE
ESCUELA DE INGENIERÍA

INSAR COMPATIBLE GROUND MOTIONS FOR NORTHERN CHILE

JOSÉ ANTONIO ABELL MENA

Thesis submitted to the Office of Research and Graduate Studies
in partial fulfillment of the requirements for the degree of
Master of Science in Engineering

Advisor:
JUAN CARLOS DE LA LLERA M.

Santiago de Chile, August 2009

PONTIFICIA UNIVERSIDAD CATÓLICA DE CHILE
ESCUELA DE INGENIERÍA

INSAR COMPATIBLE GROUND MOTIONS FOR NORTHERN CHILE

JOSÉ ANTONIO ABELL MENA

Members of the Committee:
JUAN CARLOS DE LA LLERA M.
CHARLES W. WICKS
RAFAEL RIDDELL C.
MARIO DURAN T.
GONZALO PIZARRO P.

Thesis submitted to the Office of Research and Graduate Studies
in partial fulfillment of the requirements for the degree of
Master of Science in Engineering

Santiago de Chile, August 2009

To my beloved wife, Claudia.

ACKNOWLEDGEMENTS

The work presented here briefly summarizes the main ideas collected during more than two years of work in the subject, a large part of which was made possible due to the efforts and support of people other than me to which I owe my gratitude. My apologies if, in what follows, I have inadvertently omitted anyone to whom acknowledgement is due.

The idea of finding new applications to InSAR technology in the field of civil engineering emerged jointly from my advisor, Dr. de la Llera, and Dr. Charles W. Wicks from USGS. Dr. de la Llera was kind enough to trust me with this task under his careful supervision, which I deeply thank and hope that the results have been satisfactory, I've gained from him much more than just the knowledge reflected herein. During my visit to USGS, I was offered a most complete support by Dr. Charles Wicks who exposed me to real life InSAR processing scenarios and made his years-long experience in the subject available to me, along with providing me with a sense of belonging in an, otherwise, completely foreign country. My thanks to Dr. Wicks and his family who gave me great support.

Funding for this project came from CONICYT/PBCT Proyecto Anillo de Investigación en Ciencia y Tecnología ADI#30/2006 (Chile), directed by Dr. Mario Duran who trusted us with funds, despite the long time it took to produce tangible results, without which the whole project would have been impossible. Also I am in great debt to my university, Pontificia Universidad Católica de Chile, which provided the necesarry shelter, space and peace to research. And also to the members of my defense committee Dr. Rafael Riddell and the representantive of the Office of Research and Graduate studies of the university, Dr. Gonzalo Pizarro, for their helpful advice and patience.

I would also like to acknowledge European Space Agency, which provided the raw SAR images under the Category-1 contract which were used in this study; and Dr. Urs Wegmuller and Dr. Mauritzio Santoro from GAMMA-Remote Sensing for their hospitality and support.

To my friends, engineering classmates and colleagues, with whom I had endless discussions of my work which lead to results I wouldn't have imagined. To my family which endured me in the hours of my toughest work, and provided the love and care that kept me going. Special thanks goes to my father and mother-in-law who understood, took care and more than supported me during times I had nothing to offer; their unsolicited love and trust makes me forever grateful and indebted.

Finally, my biggest thanks to my wife, Claudia, the greatest support and motivation of all, to whom I dedicate each and every hour of work in my life.

TABLE OF CONTENTS

LIST OF FIGURES

LIST OF TABLES

ABSTRACT

Design of tall buildings and flexible structures requires a better characterization of long period ground motion spectra than the one provided by current seismic building codes. Motivated by that, a methodology is proposed and tested to generate synthetic ground motions that are consistent with the observed co-seismic displacement field obtained from interferometric synthetic aperture radar (InSAR) analysis of image data in Northern Chile and Perú. This field data, in conjunction with a finite fault model of crustal deformation and inverse analysis, is used to identify fault slip distributions, which are used together with a stochastic model to predict the high frequency content of the ground motion (above 1 Hz). Additionally, the low frequency content of the signal is included by a deterministic parametric pulse which integration leads to the observed co-seismic displacement values. These synthetic signals provide an estimate for the velocity and displacement spectra, which are essential for tall-building design. In this case, inferred synthetic acceleration histories are blindly compared with recorded motions, and pseudo acceleration spectra of corrected data from the 2007 Tocopilla ($M_w = 7.7$) and Pisco ($M_w = 8.0$) earthquake events.

Keywords: InSAR; co-seismic displacement; stochastic method; velocity pulse; finite-fault inversion

RESUMEN

El diseño de edificios de gran altura y otras estructuras flexibles requiere una mejor caracterización del espectro de respuesta de diseño para períodos largos que la existente en actuales códigos de diseño. Motivado por esto, se propone y prueba una metodología para corregir registros de aceleraciones y generar registros sintéticos consistentes con el el campo de desplazamiento co-sísmico observado, obtenido mediante análisis de interferometría en imágenes de radar de apertura sintética (InSAR) obtenidas en el Norte de Chile y sur del Perú. Este campo, junto con un modelo de falla-finita de la deformación cortical y análisis inverso, se utiliza para identificar las distribuciones de deslizamiento en la falla permite conjuntamenete a un modelo estocástico, predecir el contenido de altas frecuencias del movimiento del suelo (sobre 1 Hz). El contenido de bajas frecuencias de la señal generada se modela mediante un pulso deterministico parametrizado cuya integración lleva a los valores de desplazamientos co-sísmicos observados. Estas señales sintéticas poveen una estimación para el espectro de pseudo-velocidad y desplazamiento relativo, que son herramientas esenciales para el diseño de estructuras flexibles. En este caso, los acelerogramas sintéticos se comparan con los movimientos registrados y el espectro de desplazamientos obtenido después de la corrección para los terremotos de Tocopilla ($M_w = 7.7$) y Pisco ($M_w = 8.0$) de 2007.

Palabras Claves: InSAR; desplazamiento co-sísmico; método estocástico; pulso de velocidad; inversión; falla finita

I. INTRODUCTION

I.1. Motivation

Tall building and flexible structure design in seismicly active regions requires a correct characterization of long-period ground motion which current codes have not been able to provide. The main cause of this is that accelerograph data, used to derive the response spectra that appear in the codes, presents low frequency noise that is filtered during routine data conditioning and baseline correction process, which consistently annihilates the long-period components of the records. Records thus processed usually integrate to give a near-zero final ground displacement which significantly alters the PGD and displacement sensitive portions of the response spectra. Records in the very near field, where there can be noticeable crustal deformation (co-seismic) due to the earthquake (fling-step motion), show the greatest inconsistency when corrected by simple filtering.

Many methodologies have been proposed to perform baseline correction (Boore & Bommer, 2005; Trifunac & Todorovska, 2001; Ansari, Noorzad, & Zare, 2007), although there are few that aim at recovering co-seismic displacement, literature in the subject (Boore, 2001; Chanerley & Alexander, n.d.), shows that, in general, the recovered co-seismic displacement is not-unique and, therefore, cannot be trusted. Advances in rotational ground motion seismology suggest that the measurement of all six components of ground motions is enough to recover permanent ground displacements (Trifunac & Todorovska, 2001), although these type of recordings are very infrequent. In addition to the final static offset, the PGD value of a record is affected by how the correction is done and the relative displacement response spectrum can be severely under-estimated for long oscillator periods ($>$ 20 sec or even as low as 6 sec) or over-estimated if no correction is done. Despite advances, research is still inconclusive about the period threshold beyond which the displacement response spectra is sensitive to low-period components of ground motion, more so if incursions into non-linear behavior are expected.

The existence of long period pulses leading to co-seismic displacements in the near-field was demonstrated in a recent publication (Emore, Haase, Choi, Larson, & Yamagiwa, 2007) where a guided baseline correction of strong-motion data was performed by using data from nearby continuous GPS stations (1 to 30 Hz sampling rate). This new data source showed the long-period evolution of the seismic motions and yielded seismic records with near-perfect long period components. The temporal evolution of such motions is of interest since its speed is in direct relation to which type of structures are affected. In general the final static co-seismic displacement is reached gradually and occurs mainly within the interval of strongest motion. Since these effects cannot be recovered from strong motion records directly, a-priori knowledge of the static co-seismic displacement is vital to the retrieval of the correct baseline correction and, with that, better accuracy in the long-period components.

Generation of synthetic ground motion records which are to be reliable in a broad frequency range provides additional interest in the co-seismic displacement field. Long-period consistency of such synthetics would necessarily have to include some information on the co-seismic displacement and how it scales with magnitude and attenuates with distance.

Therefore, the interest in measuring the static co-seismic displcament field due to an earthquake is twofold: first it proves vital for record correction, and second for synthetic ground motion record generation which include long-period effects. Traditionally, such precise measurements have not been available to civil engineers, but they are routinary for Earth scientists. Interferometric synthetic aperture radar (InSAR) and differential GPS are some of the main tools used for recovery of crustal displacements, which are then used to infer the processes which generate them. InSAR can provide high resolution images of deforming areas but can only measure surface change projected along the radar line-of-sight (LOS). Differential GPS measures all three components of ground motions, but its spatial resolution restricted to a few points depending on the campaign design. Both these tools, can be used to identify a model of the earthquake size, geometry and slip distributions along with the corresponding deformation field.

Thus, the main interest of this thesis is to develop awareness of the existing framework for quantification of the effect of the co-seismic displacement field, and interpret it in ways useful for the civil engineer. This displacement field information can be used to either correct recorded ground motions or generate new synthetic ones which show a higher lever of consistency in the long-period portions of the response spectrum. Additionally, it provides a means for exploring earthquake mechanisms, which can help improve the existing models for ground motion prediction. The main analysis tools that are used herein are not the devise of the author; the novelty is the use of this new source of information to improve what is currently done in processing and generation of seismic records in the context of hazard assessment for flexible structures.

I.2. Objectives

The objectives of this work are, first, to produce interferometric images corresponding to the co-seismic displacement field produced by large earthquakes in Northern Chile and Southern Perú, which have a value per se. Second, to use this data to identify the fault mechanisms of these earthquakes and generate consistent surface deformation fields. And third, capture the long-period ground motion components and their effects by correction of the existing strong-motion record in a manner consistent with the observed static co-seismic displacements, and use these to test a methodology to produce synthetic ground motion data starting from a model of the earthquake and propagation medium. The objective is to reproduce relevant features of the ground motion at rock sites, with statistics of peak ground values useful for the engineering earthquake resistant design, not to replicate actual ground motions.

The method will be calibrated and tested with the Tocopilla 2007 earthquake and compared with the available strong-motion records on rock sites. The results will be extrapolated to the Pisco 2007 earthquake and blindly compared with any available recorded motions. Additionally, for completeness, the predicted ground motions for the Antofagasta 1995 earthquake will be generated.

I.3. Bibliographical revision

The proposed methodology borrows from three distinct areas of research. The first is the use of InSAR to measure the crustal displacement due to rupture of active tectonic faults in seismic regions; second, the use of this geodetic data to identify and model earthquake mechanisms, and explore rupture processes, and develop models of crust deformation; and third, the use of pre-existent earthquake models to predict ground motions at any given site or to correct those which are independently measured.

InSAR uses a space-borne imaging radar to produce images called interferograms, which are related to surface and other changes between acquisitions within the imaged region. InSAR is a well understood subject in both the electrical engineering and geophysics research field. Good references in Synthetic Aperture Radar (SAR) are found in (Curlander & McDonough, 1991) and (Soumekh, 1999). With respect to interferometric SAR, the textbook by Hanssen (Hanssen, 2001) and the review article by P. Rosen (Rosen et al., 2000) are recommended. The basic SAR and InSAR terminology and concepts are reviewed in Appendix A and B, respectively, with references to the most relevant technical articles in the field.

Earthquake models from co-seismic displacements field, measured with InSAR, are produced by using inverse theory and models of earthquake-induced crustal deformation. The main idea is to identify the faulting mechanism geometry and slip distribution by using independent observations of it's effects. Theory of elasticity lends itself well to produce theoretic model of this crustal deformation due to dislocations occurring in the interior of an elastic media. Of particular interest is a set of closed-form solutions to the involved elastic equations in elastic homogeneous half-spaces (Okada, 1985), though modeling higher levels of complexity are possible such as layered models (He, Wang, & Yao, 2003; R. Wang, Martín, & Roth, 2003). With the forward model, it is possible to produce a set of nonlinear simultaneous equations are used to fit the earthquake model parameters to the observed displacement field (e.g. (Jonsson, Zebker, Segall, & Amelung, 2002)). Finally, physically

based heuristics, additional information about the earthquake and inverse mathematical theory (e.g. (Sambridge & Mosegaard, 2002)) are used to provide a solution. Formal aspects of the algorithms used herein can be found in Chapter 2, along with relevant references.

Many methodologies exist to produce synthetic records both in the civil engineering and geophysics research areas. Civil engineering frameworks traditionally tend to ignore the presence of these long-period motions since they are based mostly on preexistent acceleration records which are processed by filtering, although, since the fields interest is shifting to ever more flexible structures, some studies (Paolucci et al., 2008; H. Wang, Xie, Tao, & Li, 2006; Jalali & Trifunac, 2008; Bray & Rodriguez-Marek, 2004) have included the response of structures to near-field pulses which are modeled with simple mathematical waves. Geophysicists use complex finite-difference, finite-element or boundary element method models to predict motions by solution of the wave propagation equations, which would be overly-complex for civil engineering purposes where the goals are practical design solutions instead of accurate description of ground motion. Strong ground motion simulations via wave propagation is impractical for two reasons: first, the discretization requirements for modeling frequencies over 1Hz would lead to small element sizes and, hence, several millions of degrees-of-freedom with the corresponding increase in computational expense; and, second, the origin of the high-frequency portions of a strong-motion record is partly explained by the heterogeneities in the slip process which are difficult to quantify and later represent in a model. Additional sources of complexity are the inelastic behavior of crust at the frequencies of interest, which often show frequency dependent effects; geometric spreading of wavefronts; and refraction and reflection of the seismic waves in the heterogeneous media. Hence, the best methods for strong-ground motion synthesis are stochastic in nature and can only provide peak ground motion values in average. A simplified methodology based on physical facts would suffice for prediction and hazard assessment. The so-called 'stochastic method' (Boore, 2003) is based on the observation that the source Fourier spectrum for small to intermediate size earthquakes is easily described by a ω^2-shaped spectrum that scales with moment magnitude and fault size. This spectrum is used to filter a windowed Gaussian noise wave which models the observed complexities

and randomness in the process. Larger extended ruptures are modelled as an ensemble of small events which are delayed according to the propagation of the waves from source to site. This stochastic framework can simulate observed complexity while still providing the average properties predicted by mathematical models and observation. This method has been used with success to model different earthquake scenarios and has been improved in different directions (for example in (Beresnev & Atkinson, 1997; Motazedian & Atkinson, 2005; Halldorsson & Papageorgiou, 2005; Atkinson & Boore, 2006; Beresnev & Atkinson, 1999, 1998; Boore, Joyner, & Wennerberg, 1992; Assatourians & Atkinson, 2007; Guatteri, Mai, Beroza, & Boatwright, 2003)) to provide a solid framework to simulate ground motions of medium to large earthquakes for frequencies between 1 and 25 Hz.

If the objective is modelling a wider frequency band, then below the 1 Hz barrier the stochastic method can be complemented with other approaches into the so-called 'broad-band' approach (Pacor, Cultrera, Mendez, & Cocco, 2005; Graves & Pitarka, 2005; G.-Q. Wang & Zhou, October 2006). The idea is to create a partition of the spectral energy and the way different frequencies are modeled. Hence high frequencies are treated as stochastic (eg. by the stochastic method) and low-frequencies are modeled by an elastic finite-difference model of wave propagation in a layered medium. These are rather complex and detailed models which require great computational capacity and are intended to study local effects and produce a precise reconstruction of displacement time-histories. An alternative to the hybrid methods, which is embraced partly but not yet adequately by engineers, is to use a simple deterministic expression(Mavroeidis & Papageorgiou, 2003), a wavelet, to capture near-field long period effects that can be calibrated using a database of strong motion records, to model some simple pulse characteristics.

I.4. Methodology

A diagram of the proposed methodology is shown in Figure II.1. The analysis starts with raw SLC images of the region which span the occurrence of an earthquake. The earthquake interferograms are obtained by applying the techniques shown in Chapter 2 section 2, and in greater detail in Appendix B. The next step is to produce a model of

the earthquake. Conceptually, the parameters which control the earthquake model may be split into two categories: (i) source parameters that control the earthquake rupture process and its geometry (moment, dip, strike, rupture speed, etc.), and (ii) regional parameters and attenuation relationships that control the seismic propagation from the source to the receiver. The first category will be obtained by joint use of readily available information of the event (e.g. CMT solutions, NEIC hypocenters, and teleseismic finite-fault inversions) and InSAR inversion techniques to refine the modelled displacement field as shown in Chapter 2 section 4.

At this point, the earthquake model is identified and the next step is to use this to correct existing records and produce new synthetic ones. Available strong-motion records are corrected by using the information of the derived displacement field from InSAR and model results as shown in Chapter 2 section 5. Finally, these records are used to calibrate the attenuation and duration model for Northern Chile and Southern Perú and the resulting stochastic simulations are compared in Chapter 2 section 6.

I.5. Thesis structure

This thesis is structured into six chapters. The first chapter is the present and provides an overall look at the thesis objectives, methodology and main results.

Chapter two is a self-contained chapter which presents the paper 'InSAR compatible ground motions for Northern Chile' and comprises the main body of this work.

The final chapters are complementary to the main chapter. Chapter 3 discusses the main sources of error to which the presented methodology is prone. Chapter 4 offers additional conclusions which complement those presented in the main paper. And Chapter 5 discusses possible future work in this line of research.

Appendix A provides further detail into the subject of SAR analysis and processing techniques which should allow the reader to better understand the main article, Appendix B is concerned with expanding the subject of InSAR analysis, both Appendix A and B are self-contained chapters which extend what is available in Chapter 2, hence they contain

information which is also present in that Chapter. Appendix C shows, in greater detail, the subject of the generation of synthetic ground motions. C.1 covers the stochastic finite-fault method, it's main parameters, interpretations and limitations, C.2 shows the model for low-frequency pulse adopted herein, C.3 shows how the calibration of the deterministic pulse is done, and C.4 discusses the combination of both waves. Finally, Appendix D presents additional results of this thesis and is provided for completeness.

II. INSAR COMPATIBLE GROUND MOTIONS FOR NORTHERN CHILE

Abstract

Tall buildings and flexible structures require a better characterization of long period ground motion spectra than the one provided by current seismic building codes. Motivated by that, a methodology is proposed and tested to generate synthetic ground motions that are consistent with the observed co-seismic displacement field obtained from interferometric synthetic aperture radar (InSAR) analysis of image data in Northern Chile and Perú. This field data, in conjunction with a finite fault model of crustal deformation and inverse analysis, is used to identify fault slip distributions, which are used together with a stochastic model to predict the high frequency content of the ground motion (above 1 Hz). Additionally, the low frequency content of the signal is included by a deterministic parametric pulse which integration leads to the observed co-seismic displacement values. These synthetic signals provide an estimate for the velocity and displacement spectra, which are essential for tall-building design. In this case, inferred synthetic acceleration histories are blindly compared with recorded motions, and pseudo acceleration spectra of corrected data from the 2007 Tocopilla ($M_w = 7.7$) and Pisco ($M_w = 8.0$) earthquake events.

II.1. Introduction

Design of flexible structures in seismic regions requires a more consistent characterization of low-frequency ground motion components which are not well represented by design spectra in current building codes. Recorded acceleration data used to derive the response spectra has built-in low frequency noise that is filtered during baseline correction and signal processing, which in turn annihilates also the true low-frequency contents of the record (Boore, 2001). Thus, acceleration records usually integrate to near-zero residual ground displacement, distorting the PGD value and the displacement control region of the

response spectra. This effect is accentuated in the near field where the crustal deformation may reach from a few centimeters to meters.

Several methodologies have been proposed for acceleration record processing aiming to recover co-seismic displacement (Akkar & Bommer, 2006; Boore & Akkar, 2003; Paolucci et al., 2008; Ansari et al., 2007; Darragh, Silva, & Gregor, n.d.). In a recent publication (Emore et al., 2007), strong-motion data was corrected by using measurements of continuous GPS stations (1 to 30 Hz sampling rate). This data showed the low-frequency behavior of the seismic motions and enabled a guided baseline correction of the available acceleration records. These studies show that fling-pulse type recorded motions can be attributed to co-seismic displacement reached gradually from the onset of strong motion. Therefore, knowledge of the static co-seismic displacement field is a tool to improve consistency of ground motion records and spectra at low-frequencies.

A promising alternative to determine the co-seismic displacement field is the use of synthetic aperture radar interferometry (InSAR) (Rosen et al., 2000). In this technique the phase of two interfered satellite radar images of the region affected by an earthquake is the basis to derive the change in surface geometry during the earthquake in the direction of look of the satellite (Zebker, Rosen, Goldstein, Gabriel, & Werner, 1994; Fialko, Simons, & Agnew, NaN; Fialko, 2004). The displacements inferred by the procedure have different uses, such as output for an inverse determination of a finite-fault earthquake slip distribution (Pritchard, Simons, Rosen, Hensley, & Webb, 2002; Pritchard & Fielding, 2008; Jonsson et al., 2002; Motagh et al., 2008), the identification of local site-effects and activation of secondary faults, and morphology studies (inflation and deflation) at regional level (Wicks, Thatcher, Monastero, & Hasting, NaN; Lu et al., NaN; Wicks, Thatcher, Dzurisin, & Svarc, 2006). Moreover, the wide coverage of satellite images and the sub-centimeter accuracy (Ferretti et al., 2007) of the differential InSAR technique (D-InSAR), makes it a powerful tool for global analysis of seismic regions.

Knowing the earthquake slip distribution at a fault, current state-of-the-art strong-motion seismology provides different methods for the generation of consistent synthetic

ground motions. For instance, the 'stochastic method' described elsewhere (Boore, 2003), considers the earthquake-source Fourier spectrum of small to intermediate size earthquakes described by a ω^2-shaped spectrum. Yet, strong motion records show complexities that are difficult to describe by a theoretical model, at least within the frequency band at which these motions are recorded (0.5 to 100 Hz). These complexities arise from the inelastic behavior of the crust together with frequency dependent effects, geometric spreading, and refraction and reflection of seismic waves in the heterogeneous media. Thus, the stochastic framework is capable of modelling the random nature of the process while keeping its physical basis (Beresnev & Atkinson, 1997; Motazedian & Atkinson, 2005; Halldorsson & Papageorgiou, 2005; Beresnev & Atkinson, 1999, 1998; Boore et al., 1992; Assatourians & Atkinson, 2007; Guatteri et al., 2003). Although the method seems to work reasonably well for frequencies above 1 Hz, the low-frequency components are better represented by deterministic models based on elastic wave-propagation theory. Thus, broadband approaches tend to use a hybrid stochastic-deterministic approach (e.g. (Pacor et al., 2005; Graves & Pitarka, 2005; G.-Q. Wang & Zhou, October 2006)). A more simplistic approach consists in using a deterministic wave (Mavroeidis & Papageorgiou, 2003) calibrated and incorporated into the model to account for effects below 1 Hz. which proves to be a low computational-cost alternative to the hybrid method. This last approach will be tested herein with recent recorded seismicity in Northern Chile and Southern Perú.

In summary, the purpose of this work is three-fold. First, to determine the interferograms and co-seismic displacement fields for the 2007 Tocopilla (Chile) and Pisco (Perú) earthquakes. That information has a value per se, which goes beyond the other objectives of this work. Second, generate slip inversions to identify finite-fault models corresponding to these events and use them to test the quality of predictions of the synthetic ground motions generated by the stochastic method. And third, to process the database of available ground-motion records using the derived co-seismic displacement information and correction of available strong-motion records.

A flowchart summarizing the methodology used in this research is presented in Figure II.1. Step 1 involves InSAR image analysis from raw satellite data to determine co-seismic

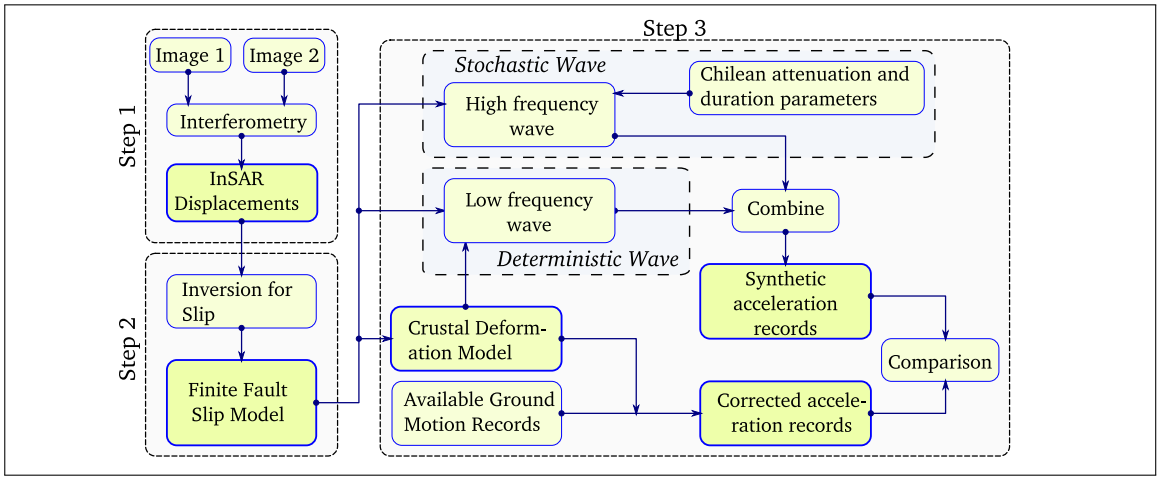

Figure II.1: Flow chart of the methodology used

displacements. Step 2 is the inversion of the co-seismic displacement data to provide a plausible fault geometry and slip distribution. And Step 3 leads to the synthesis of ground motion-data consistent with the identified fault characteristics.

II.2. InSAR Analysis

Basic concepts on Synthetic Aperture Radar (SAR), InSAR and D-InSAR are presented next. A presentation of SAR processing goes beyond the scope of this article and just few key aspects for understanding InSAR analysis are introduced. Interested readers are referred to the excellent literature on the topic (e.g. (Curlander & McDonough, 1991; Soumekh, 1999)).

A radar is an active device that sends an energy pulse and records a delayed and attenuated version of the same transmitted pulse which can be related to target distance. An imaging radar uses electromagnetic waves with frequencies in the microwave band (wavelengths from 2.4 cm to 30 cm) to illuminate a scene and record echoes of reflected waves coming from a target (back-scatterer). The energy of the echoed signal is about eleven orders of magnitude smaller than the transmitted wave. The ability to resolve a target in the range direction (radial distance from the radar source, Figure II.2(a)) is related to the radar

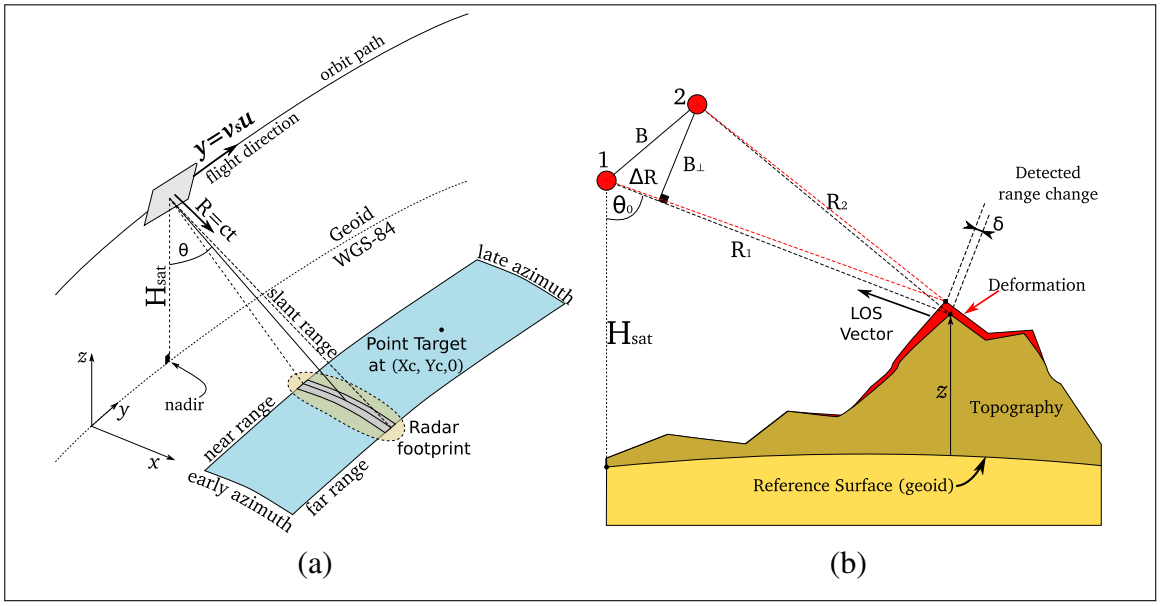

Figure II.2: Schematic view of: (a)SAR imaging geometry; and (b) D-InSAR.

pulse duration and wave speed. Perfect resolution requires sending out a very short energetic pulse (Dirac's delta function) which is physically unfeasible. Instead, a finite duration pulse is sent which limits range resolution.

On the other hand, resolution of an object in the radar cross-range direction is related to the physical size of the antenna, also called radar aperture. Larger antennas lead to improved resolution, but to achieve a usable resolution, unfeasibly large antennas are required. Thus, the idea of SAR is to emulate a larger virtual antenna by repeatedly gathering the information of many pulses which are transmitted by the satellite as it travels along its orbit. The process of taking the recorded echoes and producing the image is called SAR focusing. The target scene is de-focused during echo acquisition and must be processed before interpretation; a de-focused SAR image looks like static on a TV. Different algorithms exist for SAR focusing (Bamler, 1992), but the most intuitive and widely used is the Range-Doppler Algorithm (Bennett & Cumming, 1979) in which the image is sequentially focused in range and azimuth.

The acquisition process is done by transmitting chirp pulses at a Pulse Repetition Interval (PRI) or, inversely, at a Pulse Repetition Frequency (PRF). The process of acquisition is seen as a stop-and-go process since the speed of the pulses (light speed) is far greater than the orbital speed of the satellite. This allows to think in terms of 'radar coordinates', one along the trajectory of the satellite (azimuth, y), and another as the scatterer distance from the sensor (range, R). Shown in Figure II.2(a) are the geometry and variables; an image point is described by a coordinate pair (R, y) and the satellite altitude H_{sat} measured relative to a reference datum (e.g. WGS84) for the Earth surface.

Raw SAR images are naturally organized into an array, which contains in each line the recorded echoes for one pulse after digitalization. Thus, pixels in one line represent objects with different R value and same y value, while pixels in a column represent the opposite. The raw SAR image is said to be unfocused as a result of the SAR acquisition process that blurs the scene due to two effects. First, the transmitted pulse is of finite duration which implies that scatterers which are close to each other will respond by reflecting similar echoes of the transmitted pulse which will overlap in time at the receiving antenna if the transmitted pulse duration is longer than the time needed for the wave to travel the distance that separates the targets. Second, the radar ground footprint illuminates a nonzero width strip of land (radar footprint in Figure II.2(a)), so echoes from scaterrers at the same range yet different azimuth will also overlap at the receiver and, more important, the same target will be imaged more than once if the PRF is high enough (Soumekh, 1999).

Blurring of the image depends on the system acquisition parameters (PRF, antenna size, antenna pattern, etc.), platform motion, and viewing geometry. In the Range-Doppler algorithm, processing of the image in the range and azimuth directions is done independently (Figure II.3). Focusing yields a Single Look Complex image (SLC image), in which each pixel represents a specific point in the target area. The image point is associated with a complex number $I(R, y) = \sigma(R, y) \exp\{j\phi(R, y)\}$. Its magnitude $\sigma(R, y)$ is related to the measured reflectivity of the scattering area and its phase $\phi(R, y)$ is related to the average range of all objects within the pixel. Due to the periodicity of the exponential function, the measured phase ϕ can only be recovered in the interval $(0, 2\pi)$. For a given pixel with

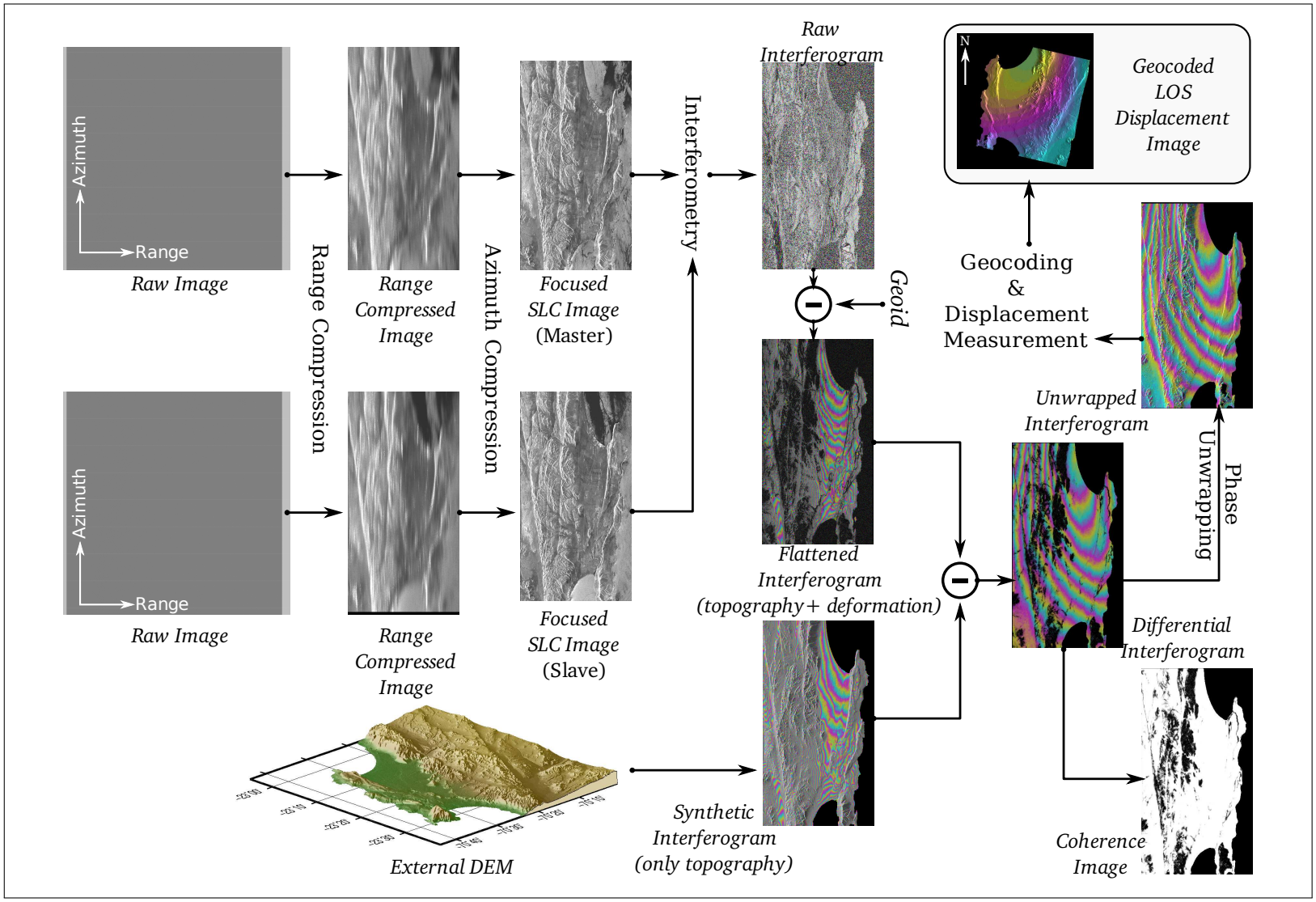

Figure II.3: Data flowchart for SAR, InSAR and D-InSAR processing

geographical coordinates (Φ, Λ), the phase is proportional to the number of wavelengths that fit in twice the distance traveled from the antenna to the target, i.e.

$$\phi(\Phi, \Lambda) = 2\pi \frac{2R_{\text{ave}}(\Phi, \Lambda)}{\lambda} \mod 2\pi \tag{II.1}$$

where R_{ave} is the average range of all objects within a pixel. As shown, objects separated in range by one wavelength λ will present the same phase value. Since the wavelength λ is small (≈ 5cm) compared to the pixel dimensions and sizes of objects inside, several cycles of the $(0, 2\pi)$ interval occur for the phase within any given pixel. This results in a very random-looking phase image with a speckle-pattern.

It is now possible to introduce InSAR analysis using these basic SAR concepts. The complete sequence of steps for InSAR and D-InSAR analysis is described in Figure II.3, please refer to this Figure for the rest of this section. As with SAR, literature in the topic is vast (e.g. (Hanssen, 2001; Rosen et al., 2000; Eineder, 2003)). Consider two Single Look Complex (SLC) images I_1 and I_2 of a certain geographic location on Earth obtained at different times to allow for surface deformation to occur. The images are rectangular grids with a complex scalar value defined per pixel, i.e.

$$I_1(\Phi, \Lambda) = \sigma_1(\Phi, \Lambda) \cdot \exp\{j \cdot \phi_1(\Phi, \Lambda)\} \qquad I_2(\Phi, \Lambda) = \sigma_2(\Phi, \Lambda) \cdot \exp\{j \cdot \phi_2(\Phi, \Lambda)\} \tag{II.2}$$

where σ_i and ϕ_i are the terrain reflectivity and complex phase of the i-th image. The process of transforming from radar coordinates (R, y) to geographical coordinates (Φ, Λ) is called geocoding. It is an important factor for successful interferometry that pixels in either image represent the same geographical point.

An interferogram is formed by complex multiplication of the first image (reference or master image) with the conjugate of the second (slave image).

$$I_{1,2}(\Phi, \Lambda) = I_1 \cdot I_2^* = \sigma_1 \sigma_2 \exp\{j \cdot (\phi_1 - \phi_2)\} = \sigma_1 \sigma_2 \exp\{j \cdot (\Delta\phi)\}$$

where $\Delta\phi$ is called the interferometric phase. With reference to Figure II.2(b), if the radar sends pulses with wavelength c/f_c – f_c is radar frequency and equals 5.35 GHz for ERS-1/2

and ENVISAT satellites– then according to Equation (II.1) the phase at which the signal of the i-th image is received back from the scatterer ϕ_i is proportional to twice distance traveled by the pulse, $2R_i$, and, hence, the phase difference is proportional to the change in range

$$\Delta\phi = \phi_1 - \phi_2 = \frac{4\pi}{\lambda}(R_1 - R_2) = \frac{4\pi}{\lambda}\Delta R \tag{II.3}$$

The change in range ΔR in Equation II.3 is the essence of interferometric analysis. In practice, SAR satellites never repeat an exact orbit track, implying a distance between orbits which is denoted as the baseline B in Figure II.2(b). The baseline can be projected into a parallel and perpendicular component to the line of sight (LOS), $B_{\parallel}$ and $B_{\perp}$. On one hand, the existence of a nonzero baseline generates the difference in perspective needed for topographic mapping (Madsen, Zebker, & Martin, 1993); on the other, it becomes a source of error in measuring surface displacements. There is also a theoretical upper limit to the baseline distance for useful interferometry which ranges from 600m to 2km depending on the radar wavelength and other characteristics. Interferometry for displacement mapping requires smaller $B_{\perp}$ values to ensure that most of the relevant signal present in the interferogram comes from the displacement signature. Consequently, the measured interferometric phase $\Delta\phi_m$ may be thought as a sum of several sources (Rosen et al., 2000)

$$\Delta\phi_m = -\frac{4\pi}{\lambda}\left(\Delta R_{\text{datum}} - \frac{B_{\perp}}{R\sin\theta}z - \delta\right) + \phi_{\text{noise}} + n\cdot 2\pi \tag{II.4}$$

The term ΔR_{datum} in Equation (II.4) corresponds to the change in range attributed to the reference surface (geoid) from which topography of the image point is measured (Figure II.2). This term is called the 'flat earth trend' and the process of removing it, 'interferogram flattening'. The second term in Equation II.4 is due to topography, i.e. elevation z measured from the reference geoid. By using a digital elevation model (DEM) from another source, this term may be approximately removed to reveal the phase contribution of the rest of the terms. Since this term depends on the perpendicular baseline $B_{\perp}$, it is essential for its estimation that accurate orbital state vectors and/or an image offset estimation, e.g. by intensity cross-correlation of the two images, be available. The third phase term δ is our target surface displacement vector projected along the radar LOS. This term may

be produced by crustal deformations, say co-seismic, but also from any other activity that may change the surface of the Earth. The term δ is considered positive pointing towards the satellite sensor; hence co-seismic uplift is indicated by a positive δ-value while subsidence by a negative one. Together with instrument and atmospheric noise that causes a phase change ϕ_{noise}, there is also a phase unwrapping term $2\pi n$. As indicated before, phase is wrapped in the interval $[0, 2\pi]$ during interferometric processing. The process of recovering this term is called 'phase unwrapping' and is an area of active research in InSAR; popular approaches include the Branch-Cut (Zebker & Chen, 2008) and the Minimum Cost Flow (MCF) algorithm (Costantini, 1998), which is the one used herein.

II.3. Earthquake Interferograms

By using the procedure indicated in Figure II.3, SLC images of Northern Chile and Southern Perú were interfered to obtain co-seismic displacements for 2 recent earthquakes, Tocopilla (Chile, 2007, $M_w = 7.7$) and Pisco (Perú, 2007, $M_w = 8.0$). Although not included herein, results were also contrasted with an available interferogram for the Antofagasta (Chile, 1995, $M_w = 8.0$) earthquake presented elsewhere (Pritchard et al., 2002). For the sake of brevity and information quality, the Tocopilla event will be used as a benchmark case for the analysis since several acceleration records are available on rock sites for this event.

The raw radar scenes were obtained from the European Space Agency (ESA) and satellites ERS-1/2 and ENVISAT. ALOS satellite data was obtained from the WINSAR Consortium (UNAVCO) data pool. The scenes and data used in this study are presented in the Appendix. The resulting unwrapped interferograms for the two events are shown in Figure II.4. Different satellite scenes were taken, and for each of them, interferograms computed. Interferograms show fringe patterns associated with the LOS displacement component and with colors that cycle according to a scale of 5cm indicating relative displacement between equal fringe colors. Positive values indicate movement towards the sensor (uplift). Fringes represent iso-displacement contours, which can be used to find relative displacements between any points within the map. For instance, Path 096 (Tocopilla) shows a coastal zone

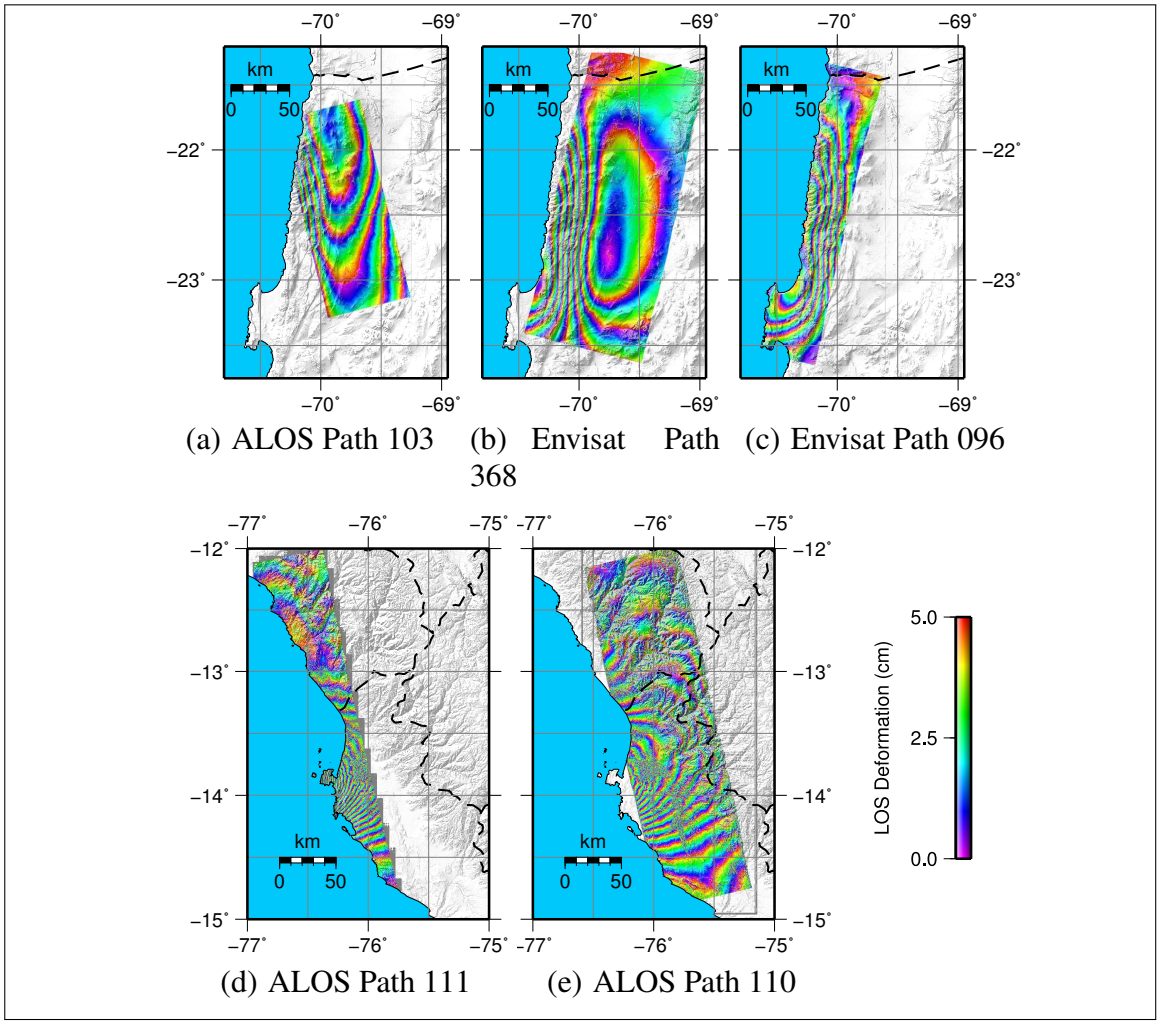

Figure II.4: Computed interferograms for Tocopilla (2007) and Pisco (2007) events: (a), (b) and (c) correspond to Tocopilla, and (d) and (e) to Pisco

of the crust that uplifts during the event while 368 confirms this and also shows a zone in the central valley that has subsidence. Northward there is a zone of little deformation that can be used as a reference point for measuring displacements (zero displacements). By counting fringes from this point toward the central valley, it is possible to identify almost 4 fringes, i.e., nearly 20 cm of LOS subsidence. Instead, by moving toward the coast the fringe count is nearly 6, i.e., 30 cm of LOS relative uplift. The different images presented in this Figure, a), b) and c) correspond to the same displacement field, but seen from a different LOS corresponding to the satellite pass. The different LOS vectors explain why

the fringe patterns look different for the different interferograms and the same earthquake event. All this will become apparent as the complete theoretical co-seismic displacement fields are determined.

Analogously, shown in Figures II.4(d)-(e) are the unwrapped interferograms obtained for the Pisco earthquake. The event was larger in magnitude than the Tocopilla event as it can be seen from the co-seismic displacement field, and the higher fringe rates. Relative coastal LOS uplift for this event is estimated to be about 100 cm using fringe counting. Due to the shallow dipping seismogenic mechanism that characterizes this earthquake there is no clear secondary subsidence lobe further inland as confirmed by Motagh (Motagh et al., 2008) in a wide-swath InSAR study of the same event. In addition, Figure II.4 provides the basis for the inversion analysis and testing of the synthetic ground motion generation procedure presented next.

II.4. Inversion for fault slip using InSAR

The forward problem used next for inversion of the fault geometry and slip distribution corresponds to the static displacement occurring on the surface of an elastic half-space due to a buried shear dislocation (Okada, 1985), which are

$$u_i = \frac{1}{F}\int\int_{\Sigma} \Delta u_j \left[\lambda\delta_{jk}\frac{\partial u_i^n}{\partial \xi_n} + \mu\left(\frac{\partial u_i^j}{\partial \xi_k} + \frac{\partial u_i^k}{\partial \xi_j}\right)\right] n_k \mathrm{d}\,\Sigma \qquad i,j,k = 1,2,3 \qquad \text{(II.5)}$$

where $u_i(x_i)$ is the i-th component of the displacement field due to a dislocation $\Delta u_j(\xi_i)$ occurring in the j-th direction at the fault surface Σ; and x_i and ξ_i are global and local (fault) coordinates respectively; λ and μ are the Lamé constants; δ_{ij} is the Kronecker delta; and n_k is k-th component of the direction cosine of the normal to the faulting surface element $\mathrm{d}\,\Sigma$. The field u_i^j represents the i-th component of the displacement at point x_i due to a point force of magnitude F in the j-th direction at ξ_i. Equation (II.5) can be demonstrated by using the principle of complementary virtual work or Betti's theorem. Please notice also that this equation is linear in the fault slip $\Delta u_j(\xi_i)$.

Closed-form integration of Equation (II.5) for a rectangular fault is used to assemble larger and more complex faults with variable slip distribution and, hence, a better representation of the fault characteristics. However, the objective is the solution of the inverse problem, i.e., to identify fault parameters (strike, dip, fault slip and dimensions) from the InSAR co-seismic displacement field. Because the problem is linear in the slip parameters, once discretized into rectangular sub-faults, it can be stated as (Steketee, 1958)

$$\mathbf{u}(\mathbf{x}, \mathbf{g}, \mathbf{m}, \nu) = \mathbf{G}(\mathbf{x}, \mathbf{g}, \nu)\mathbf{m} = \mathbf{d}(\mathbf{x}) \tag{II.6}$$

where $\mathbf{d}(\mathbf{x})$ is the vector of known co-seismic displacements at points $\mathbf{x}$; $\mathbf{G}$ is the static Green function matrix containing in each column the static displacement at $\mathbf{x}$ for a unit slip in each patch element of the fault; $\mathbf{g}$ represents geometric parameters of the model, namely fault location, orientation (strike and dip), dimensions and discretization; and ν the crustal Poisson ratio obtained from a 1D model of the crust in this region (Crust 2.0 (C., Laske, & Masters, 2000)) together with other elastic parameters; and $\mathbf{m}$ collects the unknown slip parameters associated with the chosen patch discretization to be identified.

In order to simplify the problem numerically it is common to reduce the number of unknowns by using some additional physical assumptions or known information. For example, it is usual to have a centroid moment tensor solution (CMT) for the earthquake being studied, which provides information of the fault location (hypocenter and depth), the fault plane orientation (strike and dip), and expected seismic moment. By using this information, the geometry of the fault is constrained and the linear inverse problem is solved for the faulting parameters. Details of this methodology have been presented earlier in the literature (Jonsson et al., 2002).

In this study, strike and dip angles along with and hypocenter location were obtained from previous studies using wavelet-domain inversion (Ji, Wald, & Helmberger, 2002) of teleseismic waves due to each event. Faulting extent in strike and dip direction are adjusted manually until the identified slip distribution is completely contained within the identified fault. By discretizing the slip and observed co-seismic displacement field, and

under the assumptions described, the linear inversion problem is $\mathbf{G}\ \mathbf{m} = \mathbf{d}$, where $\mathbf{G}$ is constant; $\mathbf{d}$ is given by the observed LOS co-seismic displacements; and $\mathbf{m}$ is the vector of unknown model parameters defining the strike and dip components of slip for each fault patch. Equation (II.6) is over determined since model parameters are in the few hundreds whereas InSAR displacements are in the millions of observation pixels.

Solutions to this problem should provide smooth 2D slip distributions as well as account for modelling errors produced by incorrect InSAR baseline estimations and other factors. The final inverse problem to be solved may be written as (Jonsson et al., 2002)

$$\begin{bmatrix} \mathbf{G} & \mathbf{Q} \\ \kappa^2\mathbf{D} & 0 \end{bmatrix} \begin{bmatrix} \mathbf{m} \\ \mathbf{m}_Q \end{bmatrix} = \begin{bmatrix} \mathbf{d} \\ 0 \end{bmatrix} \tag{II.7}$$

where $\mathbf{D}$ is a smoothing discretized Laplacian matrix acting on the slip distribution; κ^2 is a smoothing parameter determined by minimizing the tradeoff between smoothing and solution error (Jonsson et al., 2002); $\mathbf{Q}$ is a matrix that models the propagation of baseline errors into InSAR displacements, and is usually assumed to be a quadratic function of the space coordinates; and $\mathbf{m}_Q$ is a vector of the parameters for this function.

Data reduction techniques are also employed to down-sample the InSAR image by selecting points or spatial averages in areas of the image with impact on the resolution of the slip distribution, such as areas with high deformation gradients; on the other hand, areas with low quality interferometric signal (low coherence) are usually masked out of the scene.

Equation (II.7) was solved using a constrained linear least-squares solver (Coleman & Li, 1996), which reinforces expected slip directions. In this subduction zone, the slip was constrained to reverse faulting and to left-lateral strike slip motion (positive strike and dip-slip). The fault mechanisms identified for the Tocopilla (2007) and Pisco (2007) earthquakes are shown in Figure II.5 together with the resulting co-seismic displacement field. Arrows reflect horizontal displacements while contours reflect vertical displacements. The Tocopilla event was an underthrusting earthquake that ruptured the Nazca-South American plate interface with an epicenter roughly 40 km south east of the coastal town of Tocopilla,

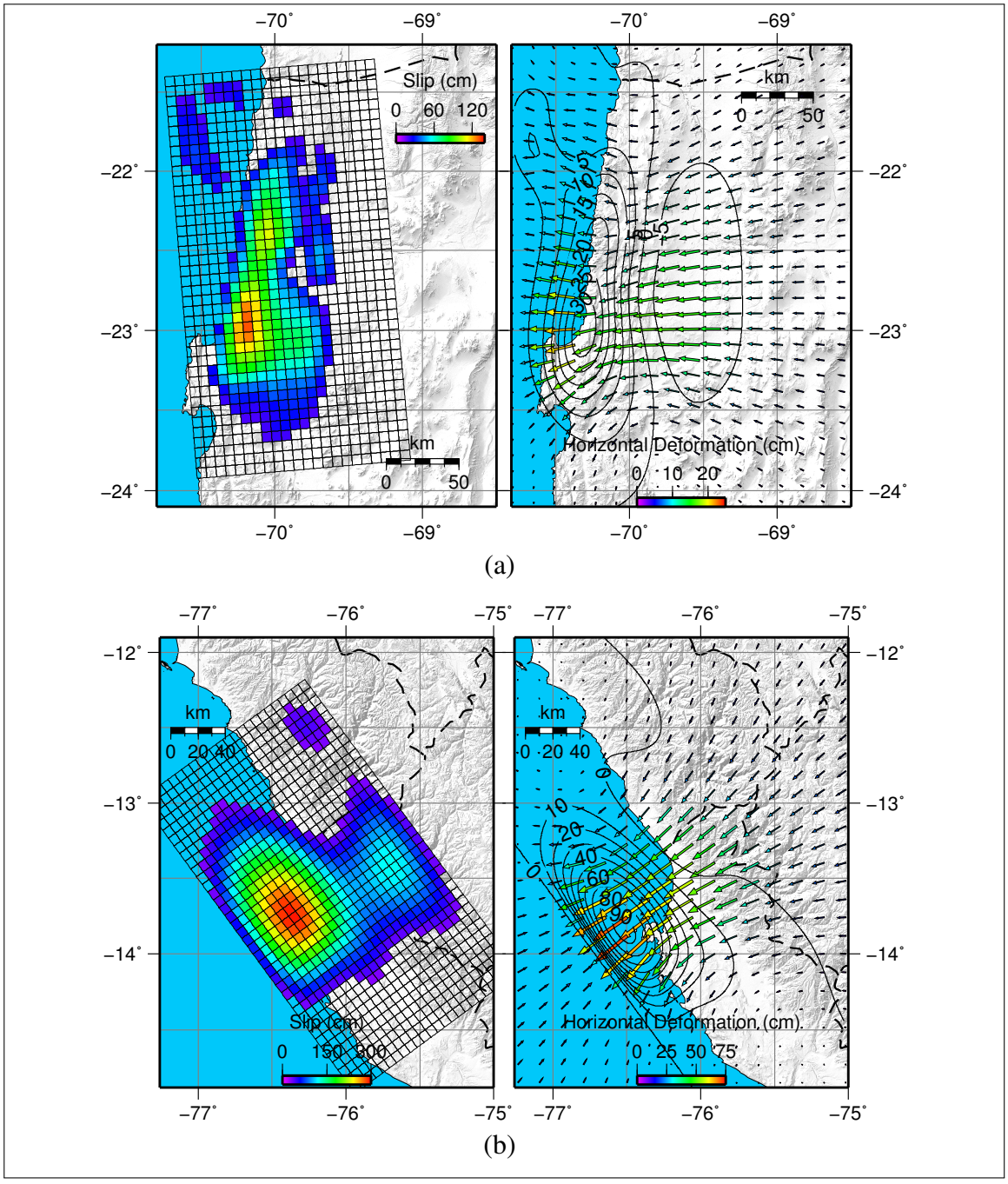

Figure II.5: Inferred slip model from InSAR earthquake displacements: (a) Tocopilla (2007), and (b) Pisco (2007)

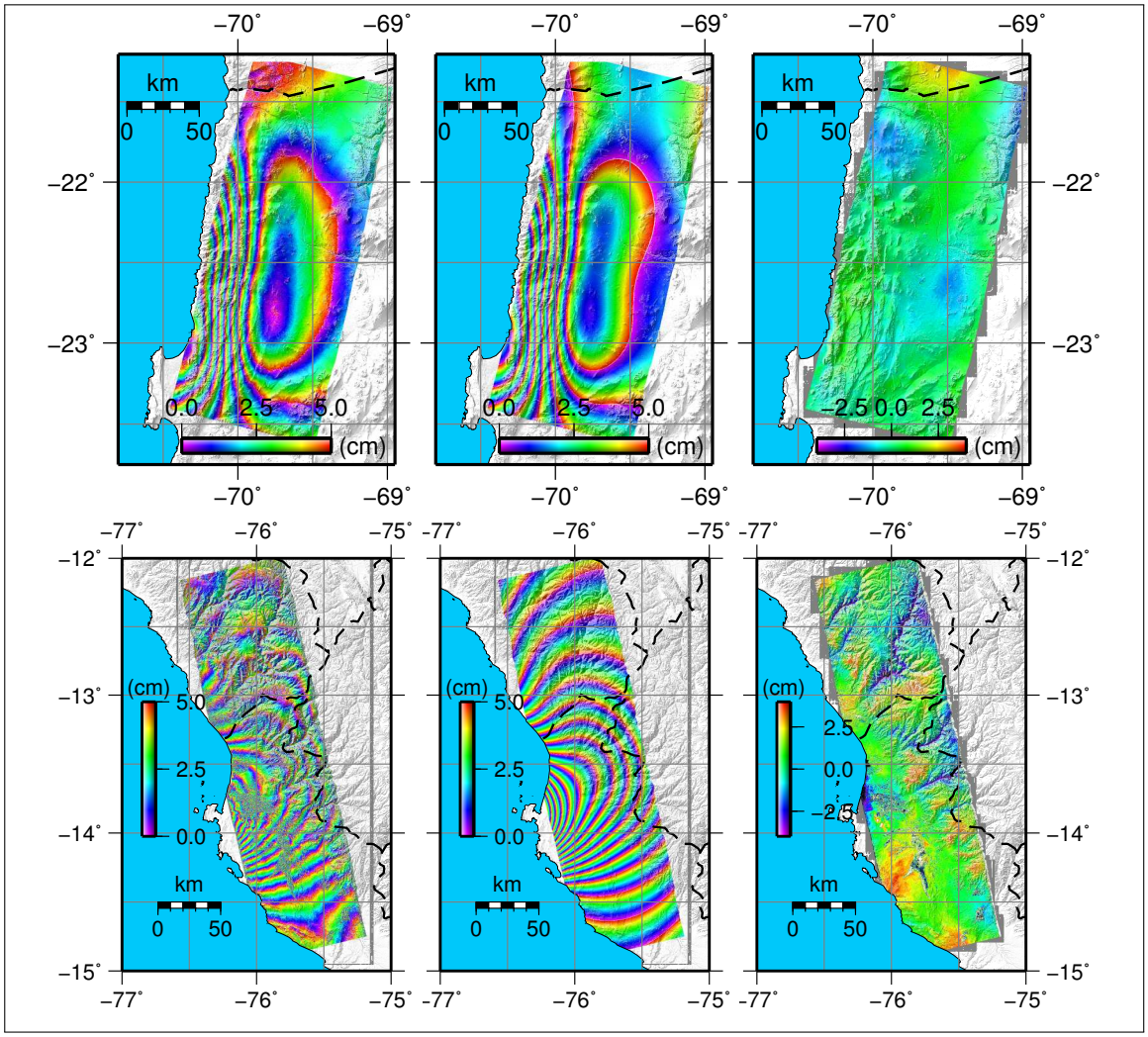

Figure II.6: Comparison between predicted InSAR interferograms and measured results with first, second and third columns showing measured data, synthetic interferogram, and inversion residuals for ENVISAT (path 096) Tocopilla, and ALOS (path 110) Pisco

Chile; the rupture is a northward continuation of the 1995 Antofagasta earthquake. The identified slip distribution shows slip concentration in two zones which is consistent with other studies (Delouis, Pardo, Legrand, & Monfret, 2009; Zeng, (UCSB), & (NEIC), 2007). The seismic moment obtained from the inversion was the same to one decimal place as the one reported in these studies ($M_w = 7.7$). Observed slip and surface displacements for Pisco (2007) are about 3 times larger than for Tocopilla. A double event was also inferred

which is consistent with strong-motion and teleseismic data, and results from other studies (Norabuena et al., 2008; Motagh et al., 2008; Pritchard & Fielding, 2008).

Shown in Figure II.4 is the comparison between the LOS displacement images for the InSAR co-seismic and synthetic co-seismic displacements generated by the identified fault model for one satellite path of the Tocopilla and Pisco events. Also shown at the right column are the modeling errors or residuals between the real and synthetic interferograms, which show fine accuracy for the displacement estimations.

II.5. Recorded accelerations and displacements

Acceleration data for the Tocopilla 2007 event was obtained from the Integrated Plate-Boundary Observatory in Chile (IPOC), a network of broadband seismometers, accelerometers, and GPS stations coordinated by GFZ Potsdam and the Institut de Physique du Globe de Paris (IPGP) in collaboration with local institutions, Universidad Católica del Norte and Universidad de Chile. Eleven stations located in bedrock, denoted as PB01-02, PB04-08 and HMB, PSG, MNM and PAT, are corrected for co-seismic displacement and used next to test the procedure to generate synthetic ground motions.

Instrumental response was first removed from the measured data by using the instrument zero-pole-gain parameters provided by the manufacturers (Guralp CMG5 for the GFZ stations, and Kinemetrics ETNA for the IPGP stations). The instrument corrected accelerations present low-frequency noise that alters the baseline of the records. The usual procedure to eliminate this noise is to high-pass filter the record; however, in this process, the final co-seismic displacement is lost, which affects the PGD and displacement response spectra.

To asses the implications of this filtering process, two different procedures were used for baseline correction of recorded accelerations. First, a standard band-pass filtering of the signal is used and, second, a modified version of a procedure proposed earlier (Boore, Stephens, & Joyner, 2002) that accounts for the known co-seismic displacement field. The latter procedure subdivides the record into three intervals, namely $I_1 : t \in [t_s, t_1]$, $I2 : t \in$

$[t_1, t_2]$ and $I_3 : t \in [t_2, t_e]$, where t_s and t_e are start and end times of the record defined by its cumulative 1% and 99% Arias intensity. If $a_0(t)$ is the instrument corrected data and $a_c(t)$ the acceleration baseline, the corrected acceleration is $a(t) = a_0(t) - a_c(t)$. The proposed baseline $a_c(t)$ is a piecewise constant function for each interval, a_i for $t \in I_i$ with $i = \{1, 2, 3\}$.

Details of the procedure to compute a_1, a_2 and a_3 are found elsewhere (Boore et al., 2002), but it proposes in general parabolic fits to the uncorrected displacements within certain subintervals of I_1 and I_3 (leading to a_1 and a_3) and velocity continuity for the displacement fits (leading to a_2).

The intermediate interval times t_1 and t_2 are free parameters to be chosen so that the final displacement provides the observed co-seismic displacement. Possible bounds for t_1 range from t_s to the PGA time of the record, whereas for t_2 range from the PGA time till the end of the record, t_e. A baseline correction is determined for each time pair (t_1, t_2) and the co-seismic displacement (average for the final seconds of the record) is compared with the InSAR value. Because many (t_1, t_2) pairs meet this criterion, the one with the least RMS velocity over the entire record is chosen. Most of the co-seismic displacement occurs in the onset of the strong motion portion of the record (interval I_2) and the acceleration baseline exhibits in this interval a complicated path that in average is represented by a_2 (Boore et al., 2002).

As an example, Figure II.7(a) shows the east-west corrected components of rock acceleration and displacement recorded during the Tocopilla (2007) earthquake. Only stations with significant ground motion are presented. The decay of the co-seismic displacement with distance is apparent. Also note that the PGD values are significantly modified by the correction procedure, while the PGA and PGV values are less affected (Table II.1). Values in Table II.1 within parenthesis correspond to direct filtering of the record without accounting for the co-seismic displacement.

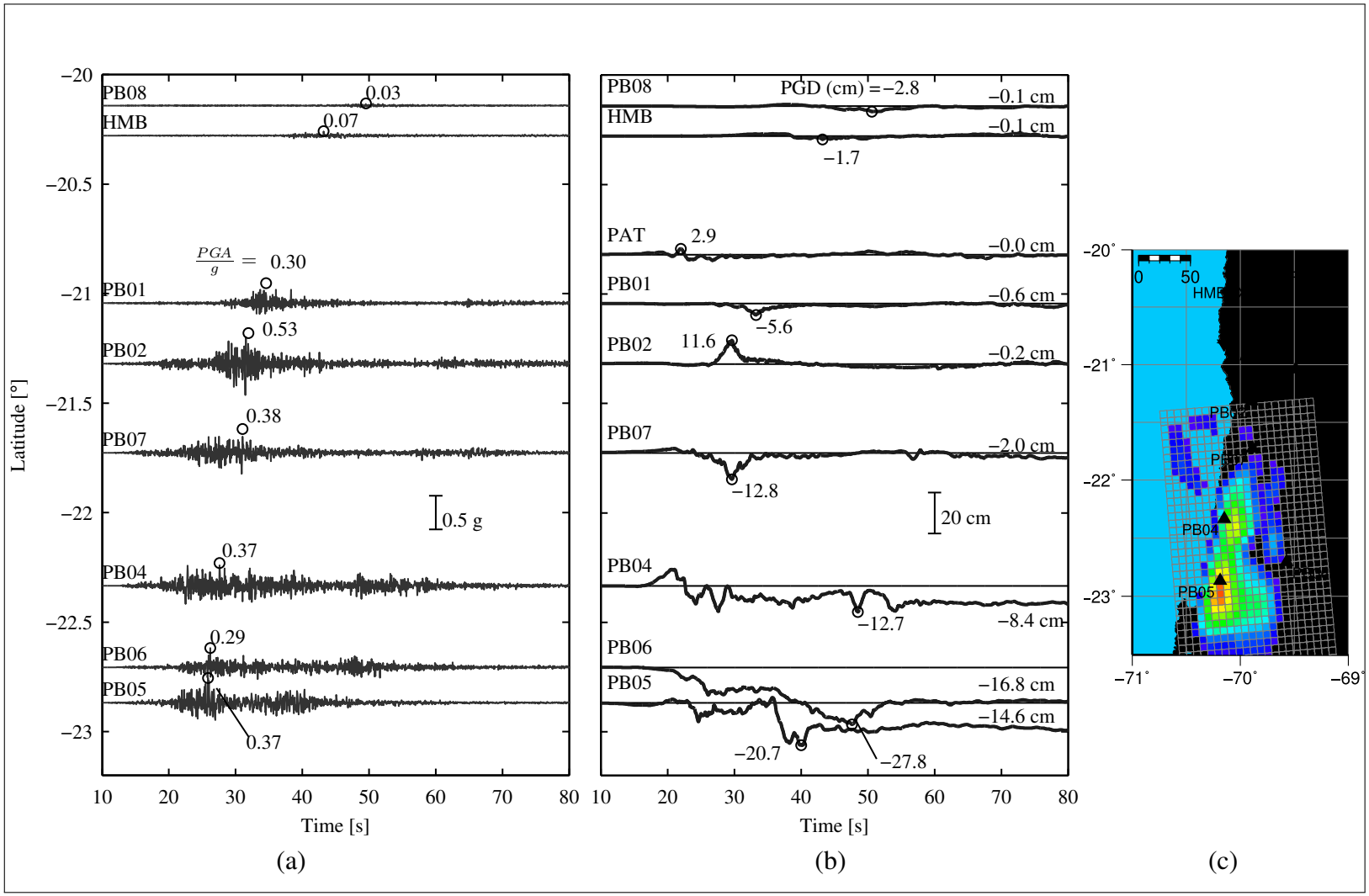

Figure II.7: Baseline-corrected ground motions for the Tocopilla (2007) earthquake in the east-west direction: (a) acceleration; (b) displacement

Table II.1: Summary of peak ground values and co-seismic displacements inferred from InSAR. (Values in parenthesis are those obtained by high-pass filtering)

Station	PGA (g)			PGV (cm/s)			PGD (cm)			Co-seismic (cm)		
	x	y	z	x	y	z	x	y	z	$u_{x\infty}$	$u_{y\infty}$	$u_{z\infty}$
PB01	0.296 (0.294)	0.120 (0.121)	0.114 (0.117)	9.7 (9.2)	5.6 (4.5)	4.3 (4.5)	5.6 (1.5)	4.8 (0.7)	3.7 (0.6)	-1.3	-1.0	-0.5
PB02	0.533 (0.486)	0.409 (0.399)	0.390 (0.352)	24.4 (23.3)	14.9 (14.5)	14.0 (13.8)	11.6 (3.5)	7.8 (1.7)	3.4 (1.2)	-2.9	-0.4	-0.0
PB04	0.372 (0.342)	0.482 (0.393)	0.295 (0.266)	28.4 (23.7)	13.2 (12.5)	10.5 (10.5)	12.7 (6.6)	4.4 (2.8)	27.3 (1.7)	-9.4	1.4	19.7
PB05	0.369 (0.325)	0.555 (0.554)	0.193 (0.167)	26.5 (20.8)	13.2 (13.3)	9.4 (7.3)	20.7 (5.0)	18.4 (2.7)	32.1 (1.3)	-13.3	-1.8	25.2
PB06	0.285 (0.288)	0.299 (0.309)	0.145 (0.139)	12.7 (13.9)	13.3 (12.0)	7.3 (7.5)	27.8 (2.7)	7.2 (1.3)	4.4 (1.3)	-15.2	-2.4	-8.5
PB07	0.377 (0.357)	0.457 (0.436)	0.477 (0.355)	20.3 (23.1)	16.0 (14.4)	14.6 (11.4)	12.8 (3.5)	7.9 (2.0)	5.7 (1.8)	-5.2	-0.3	0.7
PB08	0.032 (0.031)	0.041 (0.041)	0.019 (0.018)	2.4 (1.9)	2.8 (2.4)	2.8 (2.1)	2.8 (0.6)	3.6 (0.7)	5.9 (0.8)	-0.3	-0.3	-0.2
HMB	0.067 (0.067)	0.072 (0.071)	0.039 (0.037)	3.6 (3.0)	4.3 (4.0)	2.8 (2.5)	1.7 (0.6)	2.0 (0.6)	2.1 (0.8)	-0.1	-0.0	-0.2
PAT	0.089 (0.088)	0.098 (0.097)	0.052 (0.051)	8.4 (7.6)	5.9 (6.1)	5.1 (4.9)	2.9 (2.7)	2.6 (1.2)	3.8 (1.8)	-0.4	0.2	-0.2
PSG	0.023 (0.023)	0.020 (0.021)	0.014 (0.013)	2.2 (1.6)	1.4 (1.5)	1.0 (0.9)	2.8 (0.4)	1.2 (0.3)	1.6 (0.3)	-0.0	0.0	-0.1

Shown in Figure II.7 is a typical displacement response spectra for one arbitrary station, PB06, with and without correction to account for the co-seismic displacement. Discrepancies in spectral displacement ordinates become apparent starting at about 3 to 4 s and may be significant at longer periods. Another alternative representation of the corrected normalized response spectra for the different Tocopilla stations in rock is shown in Figure II.5. The east-west and up-down components have been normalized relative to their corresponding PGA and PGD. The average spectral value is indicated in the darker line and the rectangles reflect the standard deviation associated with the mean estimations. Values outside the unit square imply acceleration and displacement amplifications. The 45° lines indicate normalized period $\hat{T} = T/T_0$ where $T_0 = 2\pi\sqrt{PGD/PGA}$ takes different values for the spectrum at each station.

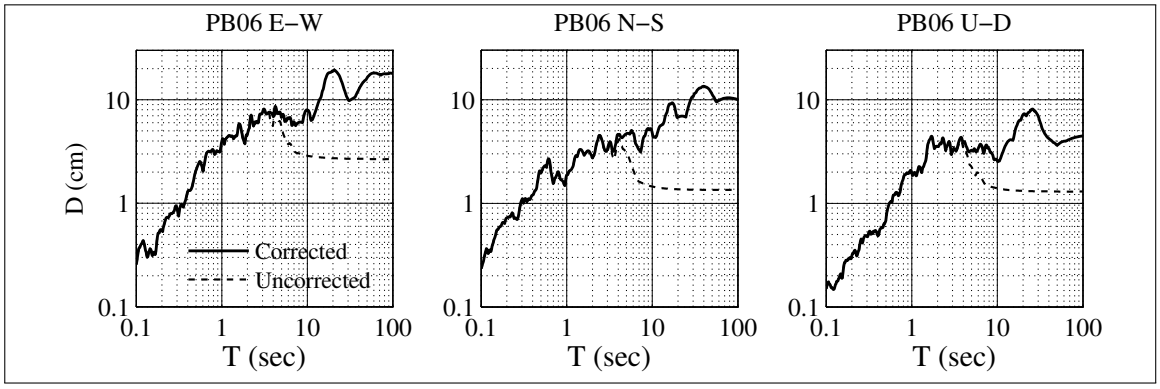

Figure II.8: Comparison between PB06 displacement response spectra corrected by accounting for co-seismic displacement and by regular filtering

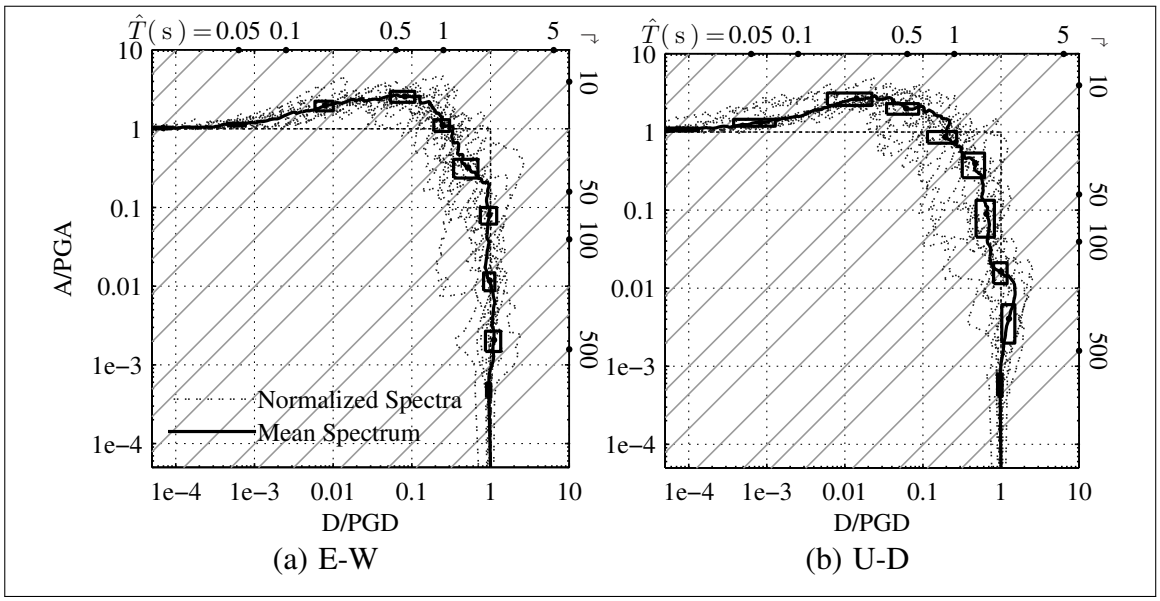

Figure II.9: Dual acceleration–displacement spectra for all stations

II.6. Generation of synthetic records

Next, a slight modification of an existing methodology (Motazedian & Atkinson, 2005) is used to generate synthetic ground motions compatible with the observed co-seismic displacement field. The analysis splits the high-frequency (> 1 Hz) and low-frequency (< 1 Hz) components of the signals. The high frequency component will be generated by an

existing finite-fault formulation of the stochastic method with an underlying ω^2 source spectrum and dynamic corner frequency (Beresnev & Atkinson, 1997, 1998, 1999). The finite-fault model geometry and slip distribution are directly imported from InSAR inversion results, and the attenuation and duration models calibrated to reproduce as an example the recorded motions of the Tocopilla 2007 earthquake; some model parameters are obtained from previous research (Delouis et al., 2009; Chlieh et al., 2008; Zeng et al., 2007). The low-frequency signal component is attributed to near-field effects and is represented by a one-sided velocity pulse (Mavroeidis & Papageorgiou, 2003) that can be directly related to co-seismic displacement. Because the detail of the stochastic method may be found in previous research (Boore et al., 1992; Boore, 2003; Beresnev & Atkinson, 1997, 1998; Motazedian & Atkinson, 2005; Assatourians & Atkinson, 2007), the presentation next only provides some essential concepts of the technique.

The basis of the stochastic finite fault method (SFFM) is to subdivide the main event, which exhibits extended faulting and a non-uniform slip distribution throughout the fault, into a discrete model composed of smaller sub-faults with uniform slip. Simulated ground motions from each sub-fault are added with proper time-delays (rupture propagation) at the observation point. Different versions of the SFFM differ mainly in how the ground motion due to one elemental sub-fault is computed. In the the SFFM procedure used herein, an elemental fault is modelled as a point source, and the ground motion synthesized at an observation site is described by the cascade frequency domain transfer function (Boore, 2003), $Y(f, R, M_0) = E(M_0, f)\, P(R, f)\, G(f)\, I(f)\, W(f)$, where E is the earthquake-source spectra, P represents path dependent effects, G is a site specific transfer function, I the instrument response, $M_0 = \mu A \bar{u}_\infty$ is the moment release of the sub-event, R is the hypocentral distance between the site and the source, and $W(f)$ is the Fourier transform of a windowed realization of a Gaussian white-noise process. Each of these terms and the parameters involved have considerable analysis in the literature and readers are referred to that work for details (Boore, 2003).

The low-frequency component of the synthetic acceleration record was modeled using a deterministic velocity pulse wavelet (Mavroeidis & Papageorgiou, 2003)

$$v(t) = \frac{A}{2}\left[1+\cos\left(\frac{2\pi f_p}{\gamma}(t-t_0)\right)\right]\cos\left(2\pi f_p(t-t_0)+\psi\right) \quad t_0-\frac{\gamma}{2f_p}\le t\le t_0+\frac{\gamma}{2f_p} \tag{II.8}$$

and zero elsewhere. This wavelet corresponds to an amplitude modulated cosine with a prevailing frequency parameter f_p; A controls the peak velocity of the pulse (PGV); γ determines the oscillatory nature of the pulse; t_0 is the time of occurrence of the peak of the wavelet envelope; and ψ is the phase shift of the modulated signal. By integrating this velocity pulse with zero initial displacement, the final value of the static displacement is

$$\Delta_{\text{static}} = \frac{A}{2\pi f_p}\cdot\frac{\sin(\pi\gamma)}{1-\gamma^2}\cos(\psi) \tag{II.9}$$

which is taken equal to the final co-seismic InSAR displacement. The main hypothesis behind this model is that the PGD is controlled by this deterministic pulse.

The estimation of the five wavelet parameters A, f_p, γ, t_0 and ψ in Equation (II.9), should be done ideally using a suite of recorded velocity traces which incorporate the effect of near fault directivity and co-seismic displacement by using the proposed baseline correction criterion. Unfortunately, a complete database of records with these characteristics is not yet available for the region, and estimations of these parameters need to be based on a mixture of available information, recorded data, some reasonable physical assumptions, and also some judgement. As an alternative, physical wave-propagation models could be used to capture the scaling relation of these parameters with event magnitude, distance and site to source geometry, but this is beyond the scope of this article. A summary of the parameters chosen for this model is presented in Annex C.

The superposition of the low and high frequency models yields the final simulated records. Because as presented, the SFFM is unable to predict different ground motion components, the only difference in synthetic record components will be found in the long-period range which must integrate to a different co-seismic displacement value.

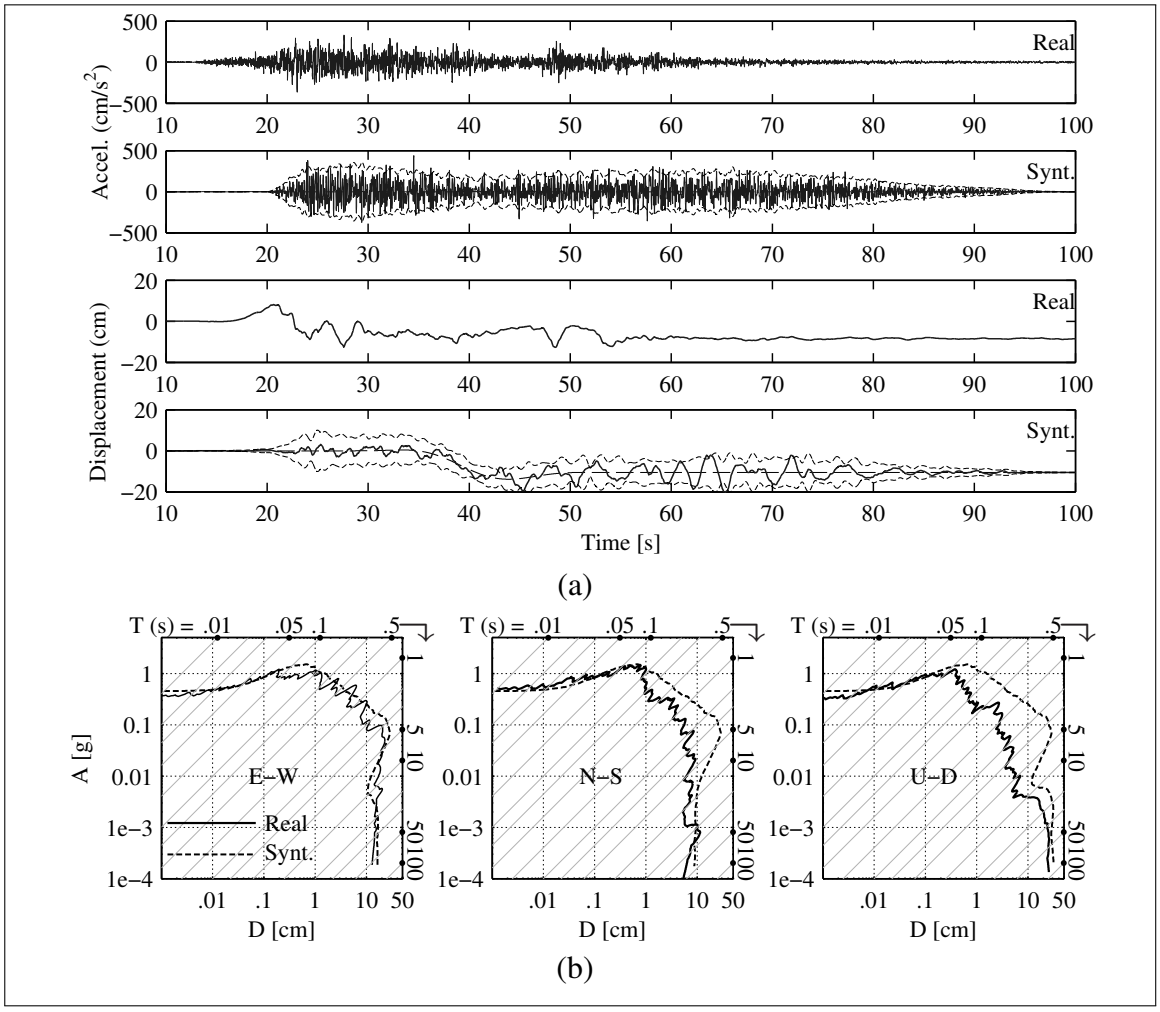

Figure II.10: Comparison between: (a) the recorded E-W component at site PB04 and simulated realization; and (b) corresponding dual spectra

Shown in Figure II.10 is a typical comparison of one realization of a synthetic acceleration record, and the resulting mean response spectrum for 20 synthetic record realizations plotted against the recorded signal and spectrum for site PB04 (Tocopilla). This site is located in the near field above the identified faulting plane. Twenty realizations per component and per station were deemed enough to capture the variability of the stochastic nature of the method. The point to point differences in time series are apparent, yet the co-seismic displacement is equal. The average PGA values also show discrepancies but the general trends of the spectrum are such that the synthetic ground motions tend to be conservative at

all frequencies. Results for other near field stations show similar trends and are presented elsewhere (see Annex). They show that the model tends to lead to a better approximation in average sense for near field stations than for far-field ones.

II.7. Conclusions

In this paper interferometric analysis of two recent earthquakes in northern Chile and south Perú was performed. Based on these interferograms, the co-seismic displacement field was obtained for the two regions affected, and used to identify the fault parameters and slip distribution. Besides, the identified slip distribution was used to correct existing ground motion data for the two earthquakes and test a stochastic methodology to compute synthetic ground motion realizations, which are compatible with the 'measured' data. As an example, corrected base-rock ground motion data obtained at different sites for the Tocopilla (2007) earthquake was qualitatively compared with synthetic accelerograms for the same locations. Results show consistent trends in the near field, but less consistent in the far field. Because more analysis of similar data and testing of other ground motion synthesis models are probably required before stating certain general trends, we have intentionally avoided proposing herein a design spectrum compatible with co-seismic displacement for the region under study. However, such result would be straight forward, and though approximate, much closer to reality than current design spectra derived from ground motion records with this co-seismic displacement filtered.

InSAR results are extraordinary in terms of their simplicity and resolution quality. There is a promissory future for this technique in connection with practical seismic engineering. Interferograms also allow to monitor uninstrumented areas, and show peculiarities attributed to local site effects, such as the activation of secondary faults, local subsidence or inflation, topographic amplification, that are difficult to capture by localized instrumentation. A shortcoming, however, is the inability of the method to resolve the time effects on the faulting process, which needs to be assumed. Although not presented herein, the Antofagasta (1995) (Pritchard & Fielding, 2008) inversions also show similar characteristics with that of Tocopilla (2007) and Pisco (2007), and the three form a good database

to develop interesting regional studies of seismic hazard. Please note that although the results herein were derived by the authors, they were possible thanks to the application of ideas, developments, and procedures devised by many other researchers from the area of geophysics. The goal was to bring a structural engineering perspective and practical application to all these relevant results, take advantage of InSAR technology, and move forward in the direction of proposing a consistent design spectrum for the design of flexible structures in the range of 3-10 seconds period.

II.8. Acknowledgements

This work was supported by CONICYT/PBCT Proyecto Anillo de Investigación en Ciencia y Tecnología ADI#30/2006 (Chile), the authors wish to acknowledge the commission. This research was also partially funded by Fondecyt project 1085282. The authors are very grateful of the support of Dr. Matthew Pritchard, who provided us with the inversion results and insight for the Antofagasta 1995 earthquake; of Dr. Gail Atkinson and Dr. Dariush Motazedian, authors of the stochastic simulation software EXSIM used herein; and Dr. Sergio Ruiz who provided us with the Tocopilla records and the instrument information to correct them.

III. SOURCES OF ERROR

One key aspect of the proposed model is the use of InSAR data to identify finite fault models of real events. In this regard, and despite Northern Chile being such a favorable area for InSAR studies(Pritchard et al., 2002), there are a number of possible aspects that conspire against the use of InSAR data to derive slip models, most importantly the sources of error in the models. Additionally, there are aspects of InSAR images which are not errors in the image yet contribute to a sub-optimal inverse solution. All of the aspects discussed herein must be taken into consideration when using InSAR images for seismic source inversion.

D-InSAR images include deformation from all sources of surface change which occurred during the time-span between the two acquisitions that conform the interferogram. This includes pre-event deformation if any; post-event relaxation; the superposition of all deformation due to foreshocks and aftershocks; localized site-specific effects such as liquefaction, compaction, land-slides, etc.; human activity, and so on. It is important to asses how these signals affect the inferred model. According to to Pritchard (Pritchard et al., 2002), the post-event crustal relaxation accounts for less than 90% in a year, and, since the time-span of the images used here is a few months in separation, it should not have a significant effect on the performed inversions. The fore and aftershocks in the case of all the studied events were relatively low magnitude events (up to $M_w = 6.0$) located on the primary rupture plane. The displacement field due to these events was found negligible compared to the main event's.

Another source of error is the possible atmospheric distortion of data. As discussed in Appendix B, atmospheric disturbances can be compensated only in very ideal cases, in general it will contribute to the noise structure of the image. In Northern Chile, the most significant effect is due to persistent cloud cover near the coast, called 'Camanchaca', atmospheric disturbances are seldom present inland due to the all year round weather stability. The inaccurate knowledge of satellite orbital state-vectors and sensor parameters also contributes to changes in the image content. Since these state-vectors can only be

known with a limited level of accuracy the quality of the perpendicular baseline estimate is directly compromised, affecting the process of elimination of topography and flat-earth effect from the interferogram. To reduce this effect, accurate orbital state-vectors (obtained from the Delft university website) were used in this study to compute a preliminary estimate of the baseline which was further enhanced by image intensity cross-correlation during co-registration. Additional considerations for incorrect baseline were made during the inversion process as explained in the main article. In any case, both effects, atmospheric and baseline estimation errors, produce artifacts in the image which can be difficult to assess to the inexperienced user.

The high degree of interferometric coherence shown in the desertic area of Northern Chile and Southern Perú is mainly due to the low level of human activity and vegetation in the area. Some areas of low coherence are found in dune fields and where the topography produces geometric distortions in the data such as layover or shadow effects (Rosen et al., 2000). In the region of interest to this study, these areas of high de-correlation tend to occur towards the coast which features both dunes and abrupt changes in topography in the so-called 'Cordillera de la Costa'. It is in this very region where the most important part of the dataset lies due to the proximity of the seismogenic layer reflected in higher deformation gradients for any event. The net-effect of these distortions is to mask out areas of high deformation, thus, lowering the resolution of the inversion method.

Regarding the inversion scheme, the partial observation of the displacement field due to water coverage degrades the method's ability to resolve the slip distribution. Resolution, for these type of inversion problems, is defined as the ability to resolve a known slip distribution given only the corresponding theoretical displacement field which in the most ideal of cases is limited. In the case of the Nazca-South American subduction zone the problem is greater since the regions of greatest displacement values and gradient values are usually underwater, masked out by the Pacific Ocean. Moreover, the method's resolution worsens with fault depth (Pritchard et al., 2002), which increases inland towards the east. These two effects can be somewhat mitigated by varying the elemental patch size with depth and

using spatial sampling techniques aimed at optimizing slip-resolution (Lohman & Simons, 2005).

D-InSAR based source inversion schemes resolve the gross aspects of the faulting mechanism and are very good at constraining the earthquake geometry for large events. Yet the finer slip detail and the temporal evolution of fault slip, which are critical for wave propagation simulation, are lost. Performing joint inversions with other datasets such as strong-motion, teleseismic or GPS data improves resolution, specially of the finer details in the fault slip distribution(Pritchard & Fielding, 2008). Additionally, using more sophisticated forward models for co-seismic ground deformation (such as the multi-layered elastic media instead of homogeneous half-space mentioned earlier) and synthetic ground motion synthesis (both in the far, teleseismic field and in the near strong motion field) provide improved resolution in comparison to coarse models at the cost of more computational effort. The cost of these implementations, both waveform inversion and multi-layered earth models, was such that was not justified for this study.

Finally, if error in the InSAR dataset cannot be avoided but can be characterized in terms of some statistical measure of the pixels, InSAR data inversion can be improved by using this information and knowledge of how it propagates into the slip model. Other authors (Hanssen, 2001; Lohman & Simons, 2005) address this issue which, again for simplicity, has not been implemented in the present work.

IV. CONCLUSIONS

This thesis presents the novel concept of using the information of the co-seismic displacement field, here obtained by InSAR, to improve the long-period spectral characterization of real and synthetic ground motion records. The methodology proposed involves three main steps: (i) measurement of the co-seismic displacement field using InSAR and other methods, (ii) inversion to compute the fault slip distribution, and (iii) correction of available records and generation of synthetic ground motion records. The method was tested for the Tocopilla (2007) earthquake, and synthetic accelerograms were compared with the recorded ground acceleration at difference sites during the earthquake. Additionally, the Pisco 2007 event was explored in less detail.

InSAR results are extraordinary in terms of their simplicity and quality. Although there is a promissory future in this technique, current techniques allow to compute an adequate approximation of the co-seismic displacement field caused by the fault dislocation. Obtained interferograms also show particularities that need further study, such as certain local effects. The identification of the co-seismic displacement field using Okada's expressions is very precise and the inverted slip distributions seem very plausible. A shortcoming however is the incapacity of the method to observe the time effect of the faulting process, which needs to be assumed. Pisco's (2007) and Antofagasta (1995) inversions also show similar characteristics with Tocopilla (2007) that may be used to develop interesting regional studies of seismic hazard.

Most of the results presented herein, although derived by the author, correspond to the application of the developments and procedure devised by other researchers mainly in geophysics. The goal here was to see how far structural engineers could do in using this information to come up with a proper design spectrum estimation that could help design structures in the long period range.

Comparison results for the Tocopilla (2007) earthquake, show reasonable agreement between synthetic models and co-seismic displacement corrected records in the near field, synthetic results are conservative in the far field. While there is more study yet to be

done, the stochastic and deterministic pulse model seem a reasonable possibility to capture the main trends of the seismic response. Additionally, its simplicity and physical basis makes this a satisfactory method for site-specific ground motion prediction within the 0.05-25Hz frequency range. Based on these results it is simple to propose a site-specific spectrum which is consistent throughout the frequency spectrum, and hence, applicable to long-period structures.

It is concluded that the information available in this field is quite beyond what most structural engineers know, and such results may be of extraordinary use to mitigate the devastating effects produced by earthquakes in structures. There is a clear need to bring these disciplines together to solve the problems of interest to societies.

V. FUTURE WORK

The coarse yet modular form in which the proposed methodology is cast into leaves many open ends which can be improved upon by future research. The methodologies used within each of the three main steps of the method can be improved upon or replaced entirely.

SAR, InSAR and D-InSAR processing techniques improve on a daily basis. Improved algorithms for image processing will lead to a better characterization of the phase value used for phase unwrapping which leads to the displacement image. Additionally, phase-unwrapping is one of the most active areas of research in the field. All the latest results should be implemented into the method to improve accuracy of the image formation step of the method.

The inverse problem solved in the present thesis is but the most simple of cases that is still useful. The estimation of the displacement field can be enhanced by using more accurate modelling of the earthquake faulting mechanism and the deforming medium. In this respect, exploring non-linear inversions to locate fault geometry, including a layered deformation model, more accurate fault geometry (including fault curvature for example), and other sources for joint-inversions will all lead to a better representation of the earthquake process than the one provided herein and conform the next step in refining the methodology. The source rupture process can only be captured by using some kind waveform inversion, which would improve greatly the characterization earthquake process and allow more realistic future scenarios to be proposed.

Baseline correction of records here is performed in a very simplistic manner. Refined results can be obtained by applying newer methodologies, for example, those based in wavelet decomposition of the signal energy. Also, the instrument noise is not removed in the present methodology, which can lead to biased results.

The SFFM with deterministic pulse is but one choice from a myriad of methods to produce the synthetic motions. Other methods should be tried and contrasted with this method in order to discriminate which is most appropriate. Additionally, these methods can always be improved upon. One improvement which is important is to provide a rational

means for predicting ground response in softer soil strata starting from the response at the base rock. This requires designing adequate transfer functions to model wave propagation effects from base rock to site through softer soil layers. Additionally, the use of nonlinear simulations of the process is also possible instead of linear system theory.

The method has to be cast into a form which allows seismic hazard assessment to be refined by using these concepts. To accomplish this, many earthquake events must be studied and modelled as accurately as possible and then used to provide credible scenarios for future hazard assessment. This will involve studying factors such as magnitude scaling of events, trends in rupture speed, propagation direction, presence and structure of asperities and heterogeneities, etc.

Finally, it is also necessary to extend the method to other seismic sources, which involves evaluating the different seismogenic mechanisms and modifying the methodology to model them consistently. Since subduction is not the only source of seismicity, in some cases, the design basis earthquake could well be controlled by intra-plate or volcanic-induced faulting event. In this regard, rutinary use of InSAR will immensely facilitate the detection of active faults and volcanoes and help provide a more accurate estimation of the probability of occurrence of natural hazards.

REFERENCES

Aki, K., & Richards, P. G. (2002). *Quantitative seismology. theory and methods* (Second Edition ed.). University Science Books.

Akkar, S., & Bommer, J. J. (2006). Influence of long-period filter cut-off on elastic spectral displacements. *Earthquake Engineering & Structural Dynamics*, *35*(9), 1145–1165.

Ansari, A., Noorzad, A., & Zare, M. (2007). Application of wavelet multi-resolution analysis for correction of seismic acceleration records. *Journal of Geophysics and Engineering*, *4*(4), 362–377.

Assatourians, K., & Atkinson, G. M. (2007). Modeling Variable-Stress Distribution with the Stochastic Finite-Fault Technique. *Bull. Seismol. Soc. Am.*, *97*(6), 1935–1949.

Atkinson, G. M., & Boore, D. M. (2006). Earthquake Ground-Motion Prediction Equations for Eastern North America. *Bull. Seismol. Soc. Am.*, *96*(6), 2181–2205.

Bamler, R. (1992, July). A comparison of range-Doppler and wavenumber domain SAR focusing algorithms. *IEEE Trans. Geosci. Remote Sens.*, *30*, 706–713.

Bennett, J., & Cumming, I. G. (1979). A digital processor for the production of seasat synthetic aperture radar imagery. In *Proceedings surge workshop.*

Beresnev, I. A., & Atkinson, G. M. (1997). Modeling finite-fault radiation from the omega-n spectrum. *Bull. Seismol. Soc. Am.*, *87*(1), 67–84.

Beresnev, I. A., & Atkinson, G. M. (1998). Finsim - a fortran program for simulating stochastic acceleration time histories from finite faults. *Seismological Reasearch Letters*, *69*(1), 27–32.

Beresnev, I. A., & Atkinson, G. M. (1999). Generic finite-fault model for ground-motion prediction in eastern North America. *Bull. Seismol. Soc. Am.*, *89*(3), 608–625.

Boore, D. M. (1986). Short-period P- and S-wave radiation from large earthquakes: Implications for spectral scaling relations. *Bull. Seismol. Soc. Am.*, *76*(1), 43–64.

Boore, D. M. (2001). Effect of Baseline Corrections on Displacements and Response Spectra for Several Recordings of the 1999 Chi-Chi, Taiwan, Earthquake. *Bull. Seismol. Soc. Am.*, *91*(5), 1199–1211.

Boore, D. M. (2003). Simulation of Ground Motion Using the Stochastic Method. *Pure and Applied Geophysics*, *160*(3-4), 635–676.

Boore, D. M., & Akkar, S. (2003). Effect of causal and acausal filters on elastic and inelastic response spectra. *Earthquake Engineering & Structural Dynamics*, *32*(11), 1729–1748.

Boore, D. M., & Bommer, J. J. (2005). Processing of strong-motion accelerograms: needs, options and consequences. *Soil Dynamics and Earthquake Engineering*, *25*(2), 93–115.

Boore, D. M., Joyner, W. B., & Wennerberg, L. (1992). Fitting the stochastic omega-2 source model to observed response spectra in western north America: Trade-offs between Deltasigma and kappa. *Bull. Seismol. Soc. Am.*, *82*(4), 1956–1963.

Boore, D. M., Stephens, C. D., & Joyner, W. B. (2002). Comments on Baseline Correction of Digital Strong-Motion Data: Examples from the 1999 Hector Mine, California, Earthquake. *Bull. Seismol. Soc. Am.*, *92*(4), 1543–1560.

Bray, J. D., & Rodriguez-Marek, A. (2004). Characterization of forward-directivity ground motions in the near-fault region. *Soil Dynamics and Earthquake Engineering*, *24*(11), 815–828.

C., B., Laske, G., & Masters, G. (2000). The current limits of resolution for surface wave tomography in north america. *EOS Trans AGU*, *81*.

Castro, R. R., Anderson, J. G., & Singh, S. K. (1990). Site response, attenuation and source spectra of S waves along the Guerrero, Mexico, subduction zone. *Bull. Seismol. Soc. Am.*, *80*(6A), 1481–1503.

Chanerley, A., & Alexander, N. (n.d.). Obtaining estimates of the low-frequency fling, instrument tilts and displacement timeseries using wavelet decomposition. *Bulletin of Earthquake Engineering*.

Chlieh, M., Rémy, D., Delouis, B., Bonvalot, S., Gabalda, G., Monfret, T., et al. (2008). *The mw 7.7 tocopilla earthquake of november 2007: Characteristics of a subduction earthquake that occurred in the brittle-ductile transition zone of the northern chile seismic gap.* ISAG.

Coleman, T. F., & Li, Y. (1996). A reflective newton method for minimizing a quadratic function subject to bounds on some of the variables. *SIAM Journal on Optimization*, *6*(4), 1040–1058.

Costantini, M. (1998, May). A novel phase unwrapping method based on network programming. *IEEE Trans. Geosci. Remote Sens.*, *36*, 813–821.

Costantini, M., Farina, A., & Zirilli, F. (1999, January). A fast phase unwrapping algorithm for SAR interferometry. *IEEE Trans. Geosci. Remote Sens.*, *37*, 452–460.

Curlander, J. C., & McDonough, R. N. (1991). *Synthetic aperture radar, systems and signal processing* (First ed.). John Wiley & Sons, Inc.

Darragh, B., Silva, W., & Gregor, N. (n.d.). *Strong motion record processing for the peer center* (Tech. Rep.). Pacific Earthquake Engineering Research.

Delouis, B., Pardo, M., Legrand, D., & Monfret, T. (2009). The Mw 7.7 Tocopilla Earthquake of 14 November 2007 at the Southern Edge of the Northern Chile Seismic Gap: Rupture in the Deep Part of the Coupled Plate Interface. *Bull. Seismol. Soc. Am.*, *99*(1), 87–94.

Eineder, M. (2003, June). Efficient simulation of sar interferograms of large areas and of rugged terrain. *IEEE Trans. Geosci. Remote Sens.*, *41*, 1415–1427.

Emore, G. L., Haase, J. S., Choi, K., Larson, K. M., & Yamagiwa, A. (2007). Recovering Seismic Displacements through Combined Use of 1-Hz GPS and Strong-Motion Accelerometers. *Bull. Seismol. Soc. Am.*, *97*(2), 357–378.

Ferretti, A., Savio, G., Barzaghi, R., Borghi, A., Musazzi, S., Novali, F., et al. (2007, May). Submillimeter Accuracy of InSAR Time Series: Experimental Validation. *IEEE Trans. Geosci. Remote Sens.*, *45*, 1142–1153.

Fialko, Y. (2004, Mar 23). Probing the mechanical properties of seismically active crust with space geodesy: Study of the coseismic deformation due to the 1992 m w 7.3 landers (southern california) earthquake. *J. Geophys. Res.*, *109*.

Fialko, Y., Simons, M., & Agnew, D. (NaN). The complete (3-d) surface displacement field in the epicentral area of t he 1999 mw 7.1 hector mine earthquake, california, from space geodetic ob servations. *Geophys. Res. Lett.*, *28*.

Graves, R., & Pitarka, A. (2005, August). Broadband time history simulation using a hybrid approach. In *Proceedings.* (CD-ROM).

Gray, A. L., Mattar, K. E., & Sofko, G. (NaN). Influence of ionospheric electron density fluctuations on satellite radar interferometry. *Geophys. Res. Lett.*, *27*.

Guatteri, M., Mai, P. M., Beroza, G. C., & Boatwright, J. (2003). Strong Ground-Motion Prediction from Stochastic-Dynamic Source Models. *Bull. Seismol. Soc. Am.*, *93*(1), 301–313.

Halldorsson, B., & Papageorgiou, A. S. (2005). Calibration of the Specific Barrier Model to Earthquakes of Different Tectonic Regions. *Bull. Seismol. Soc. Am.*, *95*(4), 1276–1300.

Hanks, T. C., & McGuire, R. K. (1981). The character of high-frequency strong ground motion. *Bull. Seismol. Soc. Am.*, *71*(6), 2071–2095.

Hanssen, R. F. (2001). *Radar interferometry: Data interpretation and error analysis* (First ed.). Springer.

Hartzell, S., Leeds, A., Frankel, A., Williams, R. A., Odum, J., Stephenson, W., et al. (2002). Simulation of Broadband Ground Motion Including Nonlinear Soil Effects for a Magnitude 6.5 Earthquake on the Seattle Fault, Seattle, Washington. *Bull. Seismol. Soc. Am.*, *92*(2), 831–853.

He, Y.-M., Wang, W.-M., & Yao, Z.-X. (2003). Static Deformation Due to Shear and Tensile Faults in a Layered Half-Space. *Bull. Seismol. Soc. Am.*, *93*(5), 2253–2263.

Jalali, R. S., & Trifunac, M. D. (2008). A note on strength-reduction factors for design of structures near earthquake faults. *Soil Dynamics and Earthquake Engineering*, *28*(3), 212–222.

Ji, C., Wald, D. J., & Helmberger, D. V. (2002). Source Description of the 1999 Hector Mine, California, Earthquake, Part I: Wavelet Domain Inversion Theory and Resolution Analysis. *Bull. Seismol. Soc. Am.*, *92*(4), 1192–1207.

Jonsson, S., Zebker, H., Segall, P., & Amelung, F. (2002). Fault Slip Distribution of the 1999 Mw 7.1 Hector Mine, California, Earthquake, Estimated from Satellite Radar and GPS Measurements. *Bull. Seismol. Soc. Am.*, *92*(4), 1377–1389.

Lohman, R. B., & Simons, M. (2005, Jan 25). Some thoughts on the use of insar data to constrain models of surface deformation: Noise structure and data downsampling. *Geochem. Geophys. Geosyst.*, *6*.

Lu, Z., Wicks, C., Dzurisin, D., Thatcher, W., Freymueller, J. T., McNutt, S. R., et al. (NaN). Aseismic inflation of westdahl volcano, alaska, revealed by satellite rad ar interferometry. *Geophys. Res. Lett.*, *27*.

Madsen, S. N., Zebker, H. A., & Martin, J. (1993, January). Topographic mapping using radar interferometry: processing techniques. *IEEE Trans. Geosci. Remote Sens.*, *31*, 246–256.

Mavroeidis, G. P., & Papageorgiou, A. S. (2003). A Mathematical Representation of Near-Fault Ground Motions. *Bull. Seismol. Soc. Am.*, *93*(3), 1099–1131.

Motagh, M., Wang, R., Walter, T. R., Bürgmann, R., Fielding, E., Anderssohn, J., et al. (2008, September). Coseismic slip model of the 2007 august pisco earthquake (peru) as constrained by wide swath radar observations. *Geophys. J. Int.*, *174*, 842–848.

Motazedian, D., & Atkinson, G. M. (2005). Stochastic Finite-Fault Modeling Based on a Dynamic Corner Frequency. *Bull. Seismol. Soc. Am.*, *95*(3), 995–1010.

Norabuena, E. O., Salazar, J., Psencik, K., Quiroz, W., Dixon, T., & Sacks, S. I. (2008, May). Coseismic displacement field of the Pisco 2007 earthquake as inferred from GPS observations. *AGU Spring Meeting Abstracts*, A3+.

Okada, Y. (1985). Surface deformation due to shear and tensile faults in a half-space. *Bull. Seismol. Soc. Am.*, *75*(4), 1135–1154.

Pacor, F., Cultrera, G., Mendez, A., & Cocco, M. (2005). Finite Fault Modeling of Strong Ground Motions Using a Hybrid Deterministic-Stochastic Approach. *Bull. Seismol. Soc. Am.*, *95*(1), 225–240.

Paolucci, R., Rovelli, A., Faccioli, E., Cauzzi, C., Finazzi, D., Vanini, M., et al. (2008). On the reliability of long-period response spectral ordinates from digital accelerograms. *Earthquake Engineering & Structural Dynamics*, *37*(5), 697–710.

Papageorgiou, A. S., & Aki, K. (1983). A specific barrier model for the quantitative description of inhomogeneous faulting and the prediction of strong ground motion. I. Description of the model. *Bull. Seismol. Soc. Am.*, *73*(3), 693–722.

Pritchard, M. E., & Fielding, E. J. (2008, May 15). A study of the 2006 and 2007 earthquake sequence of pisco, peru, with ins ar and teleseismic data. *Geophys. Res. Lett.*, *35*.

Pritchard, M. E., Simons, M., Rosen, P. A., Hensley, S., & Webb, F. H. (2002). Coseismic slip from the 1995 july 30 $m_w = 8.1$ antofagasta, chile, earthquake as constrained by insar an d gps observations. *Geophys. J. Int.*, *150*(2), 362–376.

Rosen, P. A., Hensley, S., Joughin, I. R., Li, F. K., Madsen, S. N., Member, S., et al. (2000). Synthetic aperture radar interferometry. In *Proceedings of the ieee* (pp. 333–382).

Sambridge, M., & Mosegaard, K. (2002, Dec 05). Monte carlo methods in geophysical inverse problems. *Rev. Geophys.*, *40*.

Soumekh, M. (1999). *Synthetic aperture radar signal processing with matlab algorithms* (First ed.). Wiley-Interscience.

Steketee, J. A. (1958). On volterra's dislocation in a semi-infinite elastic medium. *Can. J. Phys.*, *36*, 192–205.

Trifunac, M. D., & Todorovska, M. I. (2001). A note on the useable dynamic range of accelerographs recording translation. *Soil Dynamics and Earthquake Engineering*, *21*(4), 275–286.

Wang, G.-Q., & Zhou, X.-Y. (October 2006). 3d finite-difference simulations of strong ground motions in the yanhuai area, beijing, china during the 1720 shacheng earthquake (ms 7.0) using a stochastic finite-fault model. *Soil Dynamics and Earthquake Engineering*, *26*(10), 960–982.

Wang, H., Xie, L., Tao, X., & Li, J. (2006, Jun 01). Prediction of near-field strong ground motions for scenario earthquakes on active fault. *Earthquake Engineering and Engineering Vibration*, *5*(1), 11–17.

Wang, R., Martín, F. L., & Roth, F. (2003). Computation of deformation induced by earthquakes in a multi-layered elastic crust: Fortran programs edgrn/edcmp. *Comput. Geosci.*, *29*(2), 195–207.

Wicks, C. W., Thatcher, W., Dzurisin, D., & Svarc, J. (2006, Mar 02). Uplift, thermal unrest and magma intrusion at yellowstone caldera. *Nature*, *440*(7080), 72–75.

Wicks, C. W., Thatcher, W., Monastero, F. C., & Hasting, M. A. (NaN). Steady state deformation of the coso range, east central california, infe rred from satellite radar interferometry. *J. Geophys. Res.*, *106*.

Zebker, H., & Chen, C. W. (2008, August). Phase unwrapping for large sar interferograms: Statistical segmentation and generalized network models. *IEEE Trans. Geosci. Remote Sens.*, *40*(8), 1709–1718.

Zebker, H. A., & Chen, K. (2005, April). Accurate Estimation of Correlation in InSAR Observations. *IEEE Geoscience and Remote Sensing Letters*, *2*, 124–127.

Zebker, H. A., Rosen, P. A., Goldstein, R. M., Gabriel, A., & Werner, C. L. (1994, October). On the derivation of coseismic displacement fields using differential radar interferometry: The Landers earthquake. *Journal of Geophysical Research (Solid Earth)*, *99*, 19617–+.

Zeng, Y., (UCSB), C. J., & (NEIC), G. H. (2007). *Preliminary result of the nov 14, 2007 mw 7.7 antofagasto, chile earthquake* (Tech. Rep.). USGS.

VI. ADDITIONAL RESOURCES

Appendix A. SAR Basics

A thorough presentation of Synthetic Aperture Radar (SAR) processing is far beyond the scope of this thesis. Therefore, only few relevant concepts to appreciate the procedure of SAR analysis are introduced. A complete presentation of the technique is included elsewhere (Curlander & McDonough, 1991; Soumekh, 1999).

A radar is an active device that sends energy through a pulse to receive a delayed and attenuated version of the same transmitted pulse. An imaging radar uses electromagnetic waves with frequencies in the microwave band (wavelengths from 2.4 cm to 30 cm) to illuminate a scene and record echoes of reflected waves coming from a target (backscatterer). The energy of the echoed signal is about eleven orders of magnitude smaller than the transmitted wave.

In a regular radar, the ability to resolve a target in the range direction (distance radial from the radar source, Figure VI.1(a)) is related to the radar pulse duration and wave speed. Perfect resolution requires sending out a very short energetic pulse (Dirac delta) which is physically unfeasible. Instead, a finite duration pulse $p(t)$, of length T, is sent so the distance $x_R = cT/2$, range resolution, represents the smallest object that can be resolved in the range direction.

In the cross-range direction of a moving radar, the resolution is related to the physical size L of the antenna, or radar aperture, and the distance R to the target through the expression $x_a = R\lambda/L$, where λ is the wavelength (see (Curlander & McDonough, 1991), equation 1.2.3). For a space-based radar R is about 800Km, $L \approx 6$ m and a wavelength in the so-called C-Band is $\lambda \approx 5.6$ cm. These values yield $x_a \approx 7.5$ Km which is ridiculous and hardly usable. Thus, the idea of SAR is to emulate a virtually larger antenna by using the information of the moving radar which repeats the pulses as it travels. The process of taking the recorded echoes and producing the end image is called SAR focusing. As explained next, targets are de-focused during echo acquisition and must be processed

before interpretation; a de-focused SAR image looks like static on a TV. Different algorithms exist for SAR focusing (Bamler, 1992), but the most intuitive and widely used is the Range-Doppler Algorithm (Bennett & Cumming, 1979) in which the image is sequentially focused in the range and azimuth direction.

The acquisition process is done by transmitting chirp pulses at a Pulse Repetition Interval (PRI) or, inversely, at a Pulse Repetition Frequency (PRF). The process of acquisition is seen as a stop-and-go process since the speed of the pulses (light speed) is far greater than the orbital speed of the satellite platform. This allows to think in terms of two 'coordinates', one along the trajectory of the satellite (azimuth), and the other, the distance from the sensor (range). Times along the range and azimuth coordinates are known as fast and slow-times respectively. Phase information of the signal is preserved by treating it as a complex number and capturing the in-phase (I) and out-of-phase quadrature (Q) components.

Shown in Figure VI.1(a) are the geometry and variable names used in this section. The natural coordinate system in which the data are observed are called 'Radar Coordinates', which are a set of nonlinear transformations of the Cartesian coordinate system. An image point is described by its range R and azimuth y distances to the radar, that form a coordinate pair. This, along with a reference datum (e.g. WGS84) for the surface of earth from which the satellite altitude H_{sat} is measured, uniquely describe the position of a point in space. Radar coordinates are related to fast and slow-time through the transformation $t = R/c$ and $u = y/v_s$, where v_s is the satellite velocity along it path.

A.1. Range focusing

Radar pulses are usually chirp functions in time with a limited amount of energy which is insufficient to see through the atmosphere. This problem is solved by modulating the pulse with a sinusoidal signal of frequency f_c such that the atmosphere becomes transparent to the emmited wave (Curlander & McDonough, 1991), the signal can be written as

$$p(t) = \exp j2\pi \left\{ Kt^2 + f_c \right\} \qquad |t| \leq \frac{T}{2} \tag{A-1}$$

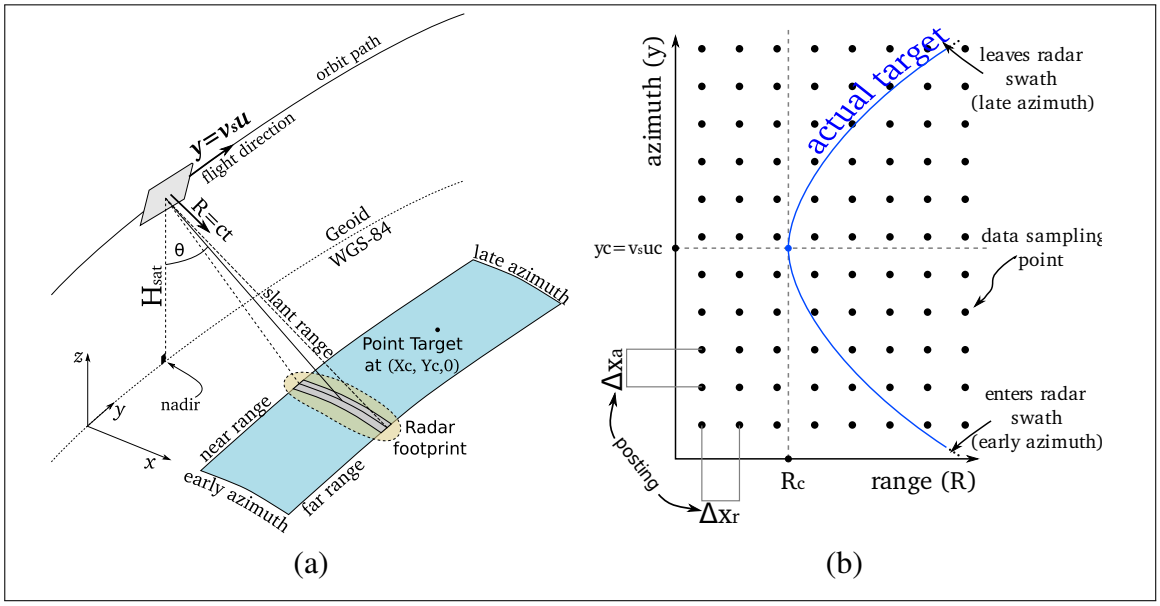

Figure VI.1: (a) SAR imaging geometry, (b) Range migration in image coordinates

where the carrier frequency f_c is usually in the microwave band (MHz-GHz) to provide the required energy level; and K is the chirp frequency rate. These pulses are time and frequency limited, hence of limited energy. A point target will produce a delayed replica of $p(t)$ while it remains in the radar illuminated footprint, it is effectively spread in time. Hence, a spatially distributed object will be spread in time by the pulse, which results in blurring or de-focusing. Conversely, an infinite energy pulse would not present this effect and would faithfully reproduce a distributed target.

If the scene consists of a single point target at a certain distance R_t with a complex reflectivity σ_R, the functional form of the returned signal is

$$s(t) = A(\phi, \theta, R, f)\sigma_R \, p\left(t - \frac{2R_t}{c}\right) \tag{A-2}$$

where A is a scalar (possibly complex) amplitude that includes effects such as signal weakening by geometric spreading with distance (R), illumination intensity variation for targets at different angles (ϕ, θ) with respect to the radar (antenna radiation pattern or illumination footprint), and possibly frequency dependence (f). A naive way of recovering the original

target signal would be by dividing the Fourier Spectrum of the echo by that of the emmited signal. Naturally, this approach fails in the presence of noise, which is inherent to the signal.

The range compression algorithm consists of using a matched filter, i.e. a convolution between the received signal and the complex conjugate of the transmitted signal, to focus the image in the range direction. This could be interpreted as the time correlation between signals that should be maximum where the signals match perfectly, i.e., at the time delay of the echo. The correlation yields a sinc-like signal centered at $t = 2R$ which corresponds to a target position in range $R = ct/2$. The sinc main lobe width is the effective resolution of the algorithm, while the data sampling rate gives the range pixel spacing (called posting).

The range-compressed (matched filtered) signal $s_R(t)$ is

$$s_R(t) = \Lambda \exp\left\{-j\frac{4\pi}{\lambda}R_t\right\} \text{sinc}\,(t^*) \tag{A-3}$$

where $t^* = \pi K T \left(t\frac{2Rt}{c}\right)$, and $\lambda = f_c/c$ the signal wavelength, and the constant Λ gathers several terms that are irrelevant. Equation A-3 approximates the original point target and represents the capacity of the system to resolve a point, a distributed target will be deblurred as efficiently as the point target is. This process is repeated for each line of the image to yield the range-focused image.

A.2. Azimuth Focusing

It is important to note that in general the range to a target is a function of the azimuth position of the satellite because the targets are not always illuminated perpendicularly to the satellite for different azimuth positions, thus relating R with the slow time variable u. The output of range compression would be

$$s_R(t) = \Lambda \exp\left\{-j\frac{4\pi}{\lambda}R(u)\right\} \text{sinc}\,(t^*) \tag{A-4}$$

where t is also a function of u. It can be shown that the t dependence on u in s_R is not relevant, and just the exponential part is useful for azimuth focusing. Now, the target

distance $R(u)$ may be represented on a Cartesian coordinate system, where the closest point of approach to (X_c, Y_c), as Figure VI.1(a)

$$R(u) = \sqrt{{H_{\text{sat}}}^2 + {X_c}^2 + (v_s u - Y_c)^2} \tag{A-5}$$

where v_s is the satellite velocity. In (R, u) coordinates (image coordinates) this can easily be identified as the locus of a hyperbola

$$R(u)^2 - {v_s}^2 \left(u - \left(\frac{Y_c}{v_s} \right)^2 \right) = {H_{\text{sat}}}^2 + X_c^2 \tag{A-6}$$

Equation A-6 illustrates the two main aspects of azimuth focusing. The first one is called range migration and reflects the fact that in the image space targets follow a hyperbolic trajectory (see Figure VI.1(b)) and processing for a specific target (image point) should be done along this trajectory. The second issue comes from the fact that the output signal from the correlator is a signal that depends on two time variables, t and u such that one can rewrite the output as

$$s_R(t,\ u) = \Lambda \exp \left\{ -j \frac{4\pi}{\lambda} \sqrt{{H_{\text{sat}}}^2 + {X_c}^2 + (v_s u - Y_c)^2} \right\} \text{sinc}\,(t^*) \tag{A-7}$$

where s_R evolves with slow-time u. Under reasonable assumptions the target range may be approximated by a second order Taylor series expansion about the time of closest approach u_c

$$R(u) \approx R_c + \dot{R}(u_c)(u - u_c) + \ddot{R}(u_c) \frac{(u - u_c)^2}{2} \tag{A-8}$$

and the signal phase is approximately

$$\phi(u) = -\frac{4\pi}{\lambda} \left(R_c + \dot{R}(u_c)(u - u_c) + \ddot{R}(u_c) \frac{(u - u_c)^2}{2} \right) \tag{A-9}$$

where the terms$f_{Dc} = -2R(u - u_c)/\lambda$ and $f_R = -2R(u - u_c)/\lambda$ can be identified and are called the Doppler centroid and Doppler rate, respectively. These parameters show how the motion of the satellite based sensor produces time changing Doppler frequency shifts on the echoed pulses. The Doppler history of a target is used for discrimination of other targets

in view. Thus, the slow-time signal that approximates the Range compression output is

$$s_R(t,\ u) = \Lambda \exp\left\{-j\frac{4\pi}{\lambda}R_c\right\} \exp\left\{j2\pi\left[f_{Dc}(u-u_c) + f_R\frac{(u-u_c)^2}{2}\right]\right\} \qquad \text{(A-10)}$$

where the $\text{sinc}(t)$ term has been dropped as approximately equal to unity, under the assumption that $|t - 2R(u)/c|/T \ll 1$, which is equivalent to stating that the echo time delay does not vary greatly in azimuth. This is true under the assumption that the product $|K|T^2 \gg 4$ which, in practice, is in the order of 100 (Curlander & McDonough, 1991).

Equation A-10 can be identified as a chirp function in slow time. Given the Doppler centroid f_{Dc} and rate f_R, this function may be used as a reference function to match-filter with the correlator output. By analogy with range compression, the output of this match filter will be a sinc function in slow time centered around the target azimuth. The greatest difficulty in implementing this is that f_{Dc} and f_R depend on the target range R_c, so a different value must be used for each range column that together with the existence of range migration, make the procedure of azimuth focusing more difficult. In some cases, the parameters can be considered constant for a certain interval of R values, which allows the processing to be done efficiently inside 'patches' using algorithms based on the FFT.

All these results are for an unsquinted geometry, i.e. with a sensor aiming perpendicularly to the flight path. The general case of a squinted geometry is derived in a similar way. For instance, Earth's rotation produces an effective squint angle which increases with distance to the Equator. It can be shown that a squinted geometry has the effect of displacing the Doppler centroid which would be equal to zero in the unsquinted case. If f_{Dc} is larger than the PRF of the system, then the Doppler centroid becomes aliased and care must be taken to avoid finding an ambiguous estimate of this parameter that would produce a poor quality image with noisy magnitude and useless phase data.

The result of azimuth focusing is called a Single Look Complex (SLC) image in time coordinates $I(t, u)$ or, since the transformation between range and fast-time is $R = ct$ and the one between slow-time and azimuth $y = v_s u$, in slant-range and azimuth coordinates $I(R, y)$. The image is naturally sampled in azimuth by the PRF, and in range by the

analog-to-digital converter that is used to store the echoes in digital media. After azimuth compression and several auxiliary correction processes, each image pixel contains a complex value which magnitude is the terrain reflectivity and which phase is an average of the distance of all objects lying within the pixel which are larger than the pulse wavelength. Pixel sizes range usually between 5-40m, depending on the radar wavelength which range between 2-30 cm. This leads to a very random-looking phase value like a speckle or 'salt and pepper' pattern. The important feature of this pattern is that it is not random and remains approximately the same for each acquisition. This last feature enables interferometry to be possible between the images.

Appendix B. SAR Interferometry Theory

In contrast with SAR, understanding InSAR is straightforward and only requires basic SAR knowledge to interpret phase information and some geometric considerations. Recommended articles on this subject are found elsewhere (Rosen et al., 2000) and (Eineder, 2003). A recommended book covering much of SAR interferometry is Hanssen's (Hanssen, 2001).

Consider two Single Look Complex (SLC) images of a certain geographic location on Earth which are separated in time to allow for change on the Earth surface. The images, called I_1 and I_2 are rectangular grids with a complex scalar value defined per pixel, i.e.

$$I_1(\Phi,\Lambda) = \sigma_1(\Phi,\Lambda)\cdot\exp\{j\cdot\phi_1(\Phi,\Lambda)\} \qquad I_2(\Phi,\Lambda) = \sigma_2(\Phi,\Lambda)\cdot\exp\{j\cdot\phi_2(\Phi,\Lambda)\} \tag{A-11}$$

where σ_i and ϕ_i are the terrain reflectivity and complex phase of the i-th image; Φ and Λ are geographical coordinates; and I_i is the i-th SLC image. The process of transforming from radar coordinates (R, y) to geographical coordinates is called geocoding and is usually performed after interferogram formation. One important factor for successful interferometry is that the corresponding pixels in each image represent the same geographical point. To achieve this a process called co-registration is performed before interferometry is done which ensures that the images are properly aligned.

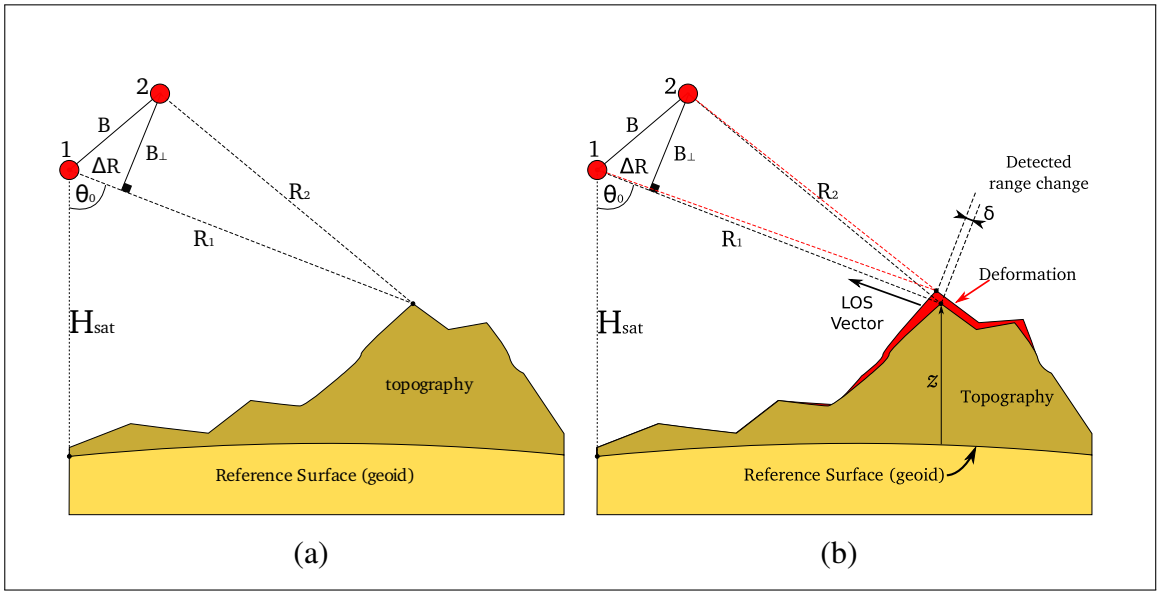

Figure VI.2: (a) InSAR Imaging Geometry, (b) D-InSAR Imaging Geometry showing range change between acquisitions

An interferogram is formed by complex multiplication of the first image (reference or master image) with the conjugate of the second (slave image).

$$I_{1,2}(\Phi,\Lambda) = I_1 \cdot I_2^* = \sigma_1\sigma_2 \exp\{j\cdot(\phi_1-\phi_2)\} = \sigma_1\sigma_2 \exp\{j\cdot(\Delta\phi)\}$$

where $\Delta\phi$ is called the interferometric phase. With reference to Figure VI.2(a), if the radar sends pulses with wavelength $= f_c/c$ (f_c is the radar frequency which is 5.35 GHz for ERS-1/2 and ENVISAT satellites), then the phase at which the signal is received back (echo of the outgoing pulse) is proportional to the distance traveled to the target and back, $2R$, so

$$\phi_i(\Phi,\Lambda) = 2\pi\frac{2R\,(\Phi,\Lambda)}{\lambda} \qquad \text{(A-12)}$$

In this way the interferometric phase will be related to the path difference by

$$\Delta\phi = \frac{4\pi}{\lambda}\Delta R \qquad \text{(A-13)}$$

Though agencies which own SAR capable satellites report 'repeat orbit track' periods of roughly a month, the fact is that a satellite never repeat an orbit track exactly, implying a difference between the orbits which is called the baseline and is schematically shown in Figure VI.2(a). The baseline can be projected into a component which is parallel to the line of sight to the master satellite, $B_{\parallel}$, and a perpendicular component $B_{\perp}$. The existence of a baseline is important since it provides the difference in perspective needed for topographic mapping (Madsen et al., 1993); on the other hand, it becomes a source of error in measuring surface displacements. There is also a theoretical upper limit to the baseline length beyond which the speckle pattern in the image, which was discussed in the previous section, changes excessively and the pixels become uncorrelated rendering the image useless. This critical value is about 1100m for C-Band satellites ($\lambda 5.35$ GHz, like European ERS-1, ERS-2 and ENVISAT satellites) and about 4000m for L-Band satellites ($\lambda = 23$ cm, like the Japanese ALOS satellite). In practice, interferometry for displacement mapping requires smaller values of the perpendicular baseline which ensure that the most relevant signal present in the interferogram belongs to the displacement signature.

An estimate of pixel correlation is called the image coherence and is calculated (Zebker & Chen, 2005)

$$\gamma = \frac{E\{I_1 I_2^*\}}{\sqrt{E\{|I_1|^2\}E\{|I_2|^2\}}} = |\gamma| \cdot \exp\{-j\phi\} \tag{A-14}$$

The expected values are calculated within windows in real interferograms using the complex values of the SLCs; this results in a biased, yet useful, measure of the correlation. The amplitude $|\gamma|$ is called the degree of coherence and is a measure of correlation between the two SAR images. Coherence is normalized between 0 and 1 with 1 meaning perfect pixel correlation. Its counterpart, correlation estimates the reliability of the associated phase value since the standard deviation of phase grows with decreasing correlation (Zebker & Chen, 2005).

Based on Figures VI.2(a) and VI.2(b) and other considerations the measured interferometric phase $\Delta\phi_m$ proceeds from real physical values and consists of several sources

(Rosen et al., 2000)

$$\phi_m = -\frac{4\pi}{\lambda}\left(\Delta R_{\text{datum}} - \frac{B_\perp}{R\sin\theta}z - \delta - \rho\right) + \phi_{\text{noise}} + n\cdot 2\pi \qquad \text{(A-15)}$$

where the term ΔR_{datum} is produced by the change in range of the imaged point located on top of the reference surface from which topography is measured (datum geoid, typically WGS84) that produces different phase values for different ranges even in the absence of other effects. This term is called the 'flat earth trend' and the process of removing it 'interferogram flattening'.

The second term is produced due to topography, elevation z measured from the reference geoid, at different locations. By using a digital elevation model (DEM) from another source, this term may be removed, in the so-called two-pass approach, to reveal the contribution to the phase of the rest of the terms in Equation A-15. Since this term depends directly on the perpendicular baseline $B_\perp$, it is essential to have a good estimation of $B_\perp$ which is obtained from orbital state vectors and/or image offset estimation via cross-correlation of the two (this process is part of image co-registration). A three-pass approach involves using three SLCs, one 'topographic' pair used to derive an interferogram with (hopefully) only altitude information, and a third image to generate the interferogram contains the displacements to be measured. A four-pass approach is also possible in which two different pairs are used to generate the topographic and displacement interferograms. In all cases, $B_\perp$ must be carefully estimated.

The third phase term δ is the surface displacement vector projected along the radar line-of-sight (LOS) and it is our main target. This term is produced by crustal displacements, say co-seismic, and any other activity may that change the surface of the earth such as erosion, subsidence, land-slides, human activity, etc. δ is considered positive towards the sensor, hence co-seismic uplift is indicated by a positive value while subsidence is the opposite. Other authors use other conventions to define this term, in our case positive displacement leads to negative phase change.

The atmospheric delay term ρ is produced by changes in water vapor concentrations in the atmosphere between acquisitions, which can produce a significant echo time delay. Often this term is very much correlated (in the statistical sense) with topography since the time delay depends on the distance traveled by the EM waves through the atmosphere, hence, the length of the atmosphic column which changes with height. A model can be fitted along with altitude information (say a DEM) and the atmospheric artifact removed. This only works if the atmospheric changes are nearly the same for the whole image. In Northern Chile, the coastal cloud cover called the 'camanchaca' usually deteriorates the signal towards the coast. Ionospheric distortions, which depend mainly on solar activity also produce localized phase defects that are difficult to remove, specially for radars operating at longer wavelengths like L-Band (Gray, Mattar, & Sofko, NaN).

Together with instrument noise, there is a phase unwrapping term $n2\pi$. This last term is lost during interferometric processing due to the fact that the phase can only be recovered in the interval $[0, 2\pi]$ because interferometric processing aliases the phase modulo-2π. The process of recovering this term is called 'phase unwrapping' and is an area of active research in InSAR since no robust algorithm exists so far to perform completely automatic phase unwrapping; human intuition is almost always needed for a successful procedure. Popular approaches include the Branch-Cut algorithm (Zebker & Chen, 2008) and the Minimum Cost Flow (MCF) algorithm (Costantini, 1998) which is the one used herein. An alternative approach which is fast and easy to implement, yet less accurate, is also found elsewhere (Costantini, Farina, & Zirilli, 1999).

Appendix C. Generation of Synthetic Records

The generation of synthetic ground motions compatible with the observed static displacement field is done by superposition of high-frequency signals (above 1Hz) and low-frequency ones. The latter capable of representing the final static displacement of the surface. The low-frequency signal representation is based on the procedure proposed by Mavroeidis and Papageorgiou in 2002 (Mavroeidis & Papageorgiou, 2003). In their work, they use a deterministic functional waveform to represent the long-period velocity pulse

characteristic of near-fault ground motions. Velocity pulses can be related, among different sources, to co-seismic displacement, or fling-step displacements on the surface. Since the procedure enables the inclusion of signals with high frequency content (generated by other methods) it may successfully simulate broadband acceleration time series.

In the work by Mavroeidis and Papageorgiou, the long-period waveforms are dependent on various earthquake parameters which have been calibrated using a database of strong ground motion records. The objective is to reproduce only the forward-directivity pulses. Empirical relationships for parameter scaling were derived, and successfully used to reproduce the long-period pulses present in their suite of records. The authors caution against using their results to generate series that include a co-seismic displacement, since their calibrated parameters are only as good as their database. Nevertheless, since the model is purely phenomenological, nothing prohibits the use of different information, ie. the deformation model, to calibrate the pulses. As a model for the high frequency content acceleration signal the authors used the specific barrier model (Papageorgiou & Aki, 1983) and the two waves are merged in a process explained herein.

Motazedian and Atkinson (2005) extended the finite fault formulation of the stochastic method with an underlying ω^2 source spectrum (Beresnev & Atkinson, 1997, 1998; Atkinson & Boore, 2006) to produce sub-sources with a rupture history dependent corner frequency. They also showed how to include long period signals in their procedure but provided no further insight on calibration of the deterministic wave.

In the present work the long-period pulses are calibrated such that the final displacements of the synthetic ground motions are consistent with the observed InSAR static displacements. High-frequency content is provided by the Motazedian-Atkinson procedure with parameters calibrated to reproduce the Tocopilla 2007 earthquake ground motions in an response spectrum average sense.

C.1. High-Frequency Wave

The basis of the stochastic finite fault model is to subdivide the main event, which exhibits extended faulting and a non-uniform slip distribution throughout the fault, into a discrete model with uniform slip smaller sub-faults. Each sub-fault contributes with a correct time delay to the ground responses on a given point, which is computed from the superposition of all sub-fault responses. Thus, the extended fault model (obtained from InSAR) was subdivided into a mesh of point sources, which Fourier spectrum of acceleration $Y(j\omega)$ can be correctly characterized using transfer functions to account for different effects (Boore, 2003) in cascade, i.e.

$$Y(f, R, M_0) = E(M_0, f) \cdot P(R, f) \cdot G(f) \cdot I(f) \tag{A-16}$$

where E is the earthquake-source spectra; P represents path dependent effects; G is a site specific transfer function; and I the instrument response. In A-16 M_0 is the moment release of the event and R is the hypocentral distance between the site and the source.

The stochastic method for a single sub-fault starts with a noise signal, say Gaussian white-noise, which is windowed to yield a finite duration signal. To produce a realization of ground accelerations at high frequencies the windowed noise is then modulated by the appropriate transfer functions described in Equation A-16. In the remaining of this section, the derivation of each independent transfer function is explained.

A complete expression for the displacement in time due to a point shear dislocation in a homogeneneous elastic space is presented elsewhere (Aki & Richards, 2002). The far-field approximation to the displacement function is

$$\mathbf{u}(\mathbf{x}, t) = \frac{\mathbf{A}^{\theta\gamma}}{4\pi\rho\beta^3 R}\mu A\dot{\bar{u}}(t - R/\beta) \tag{A-17}$$

where $\mathbf{A}^{\theta\gamma}$ is the near field radiation pattern vector; μ, ρ and β are the crustal shear modulus, density and shear wave velocity respectively; R is the distance between the observation and the fault; and A the fault area; and u is the mean fault slip vector on A.

Therefore the far field radiation depends on the derivative of the slip time function. Beresnev and Atkinson demonstrate (Beresnev & Atkinson, 1997) that using fault slip function of the form

$$\bar{u}(t) = \bar{u}_\infty \left[1 - (1 + \frac{t}{\tau})e^{-t/\tau}\right] \tag{A-18}$$

where $\bar{u}_\infty$ is the final static displacement of the fault and τ is the source time constant. If the slip velocity function $\dot{\bar{u}}(t) = \dfrac{\bar{u}_\infty}{\tau}\left(\dfrac{t}{\tau}\right)e^{-t/\tau}$ is substituted into Equation A-18 and it's Fourier Transform written, the functional form of the observed displacement Fourier spectrum for far-field point-source radiation, called the ω^2 spectrum, is yielded

$$|\mathbf{u}(\mathbf{x},\ \omega)| = \frac{\mathbf{A}^{\theta\gamma} M_0}{4\pi\rho\beta^3 R}\left[1 + \left(\frac{\omega}{\omega_c}\right)^2\right]^{-1} = \frac{E(M_0,\ f)}{R} \tag{A-19}$$

where the released seismic moment is $M_0 = \mu A \bar{u}_\infty$ and the corner frequency $\omega_c = 1/\tau$. Equation A-19 is the seismic source transfer function divided by R, this $1/R$ factor represents part of the path-effect and is excluded from the earthquake source term. The corner frequency is related to the total seismic moment released and fault geometry, the following equations (Beresnev & Atkinson, 1997) are used to determine ω_c

$$f_c = \frac{y z_\alpha}{\pi}\frac{\beta}{L} \qquad\qquad M_0 = \Delta\sigma L^3 \tag{A-20}$$

where the first equation represents the corner-frequency scaling law, and the second, the seismic moment scaling law; L is an equivalent fault radius or predominant length; y is the ratio of rupture speed to shear wave velocity β; and $z_\alpha = t_\alpha/\tau$ where t_α is the time needed to reach $\alpha = \bar{u}(t_\alpha)/u_\infty\%$ of the final static slip. The equation for M_0 relates seismic moment to the fault radius via the stress drop parameter $\Delta\sigma$, which actually is not physically meaningful since the stress drop across a fault with slip u_∞ is $\Delta\sigma = \mu\bar{u}_\infty/L$ and there is poor knowledge of the elastic parameter μ in the vicinity where the slip occurs. Hence, $\Delta\sigma$ is interpreted as a free model parameter that that is used along with M_0 to select L and, thus, directly influences the corner frequency and the spectral decay at low frequencies. As stated elsewhere (Beresnev & Atkinson, 1997), this is an awkward definition from a physical standpoint since the discretization should be independent of seismic moment and

chosen stress parameter. A practical model should provide the flexibility to choose the fault discretization based on convenience, computational cost, etc.

To resolve this, the corner frequency is treated as a dynamic quantity (Motazedian & Atkinson, 2005) since the radiated seismic moment is a function of time and, hence, so is the corner frequency. It evolves in time from the corner frequency of a single sub-fault to the decreased corner frequency of a fault with the dimensions and seismic moment of the entire fault.

Besides the theoretical $(1/R)$ S-wave attenuation for a homogeneous elastic whole-space, attenuation in practice shows a more complicated structure due to reflection an refraction of traveling waves in the Earth. Where attenuation is also a frequency dependent feature. A usual model of the path effect with distance and frequency dependent terms is (Boore, 2003)

$$P(R,\ f) = Z(R) \exp\left\{-\pi \frac{fR}{Q(f)\beta}\right\} \tag{A-21}$$

where $Z(R)$ includes the geometric attenuation term and the exponential term is the frequency dependent inelastic attenuation with Q possible of the form (Castro, Anderson, & Singh, 1990) $Q(f) = Q_0 f^{\eta}$ or other shapes can be adopted. This operator, in practice, shows low values (attenuation) for high frequencies and for the very low frequencies, a feature that cannot be modelled simultaneously by the chosen functional form. The geometrical attenuation is assumed as a piecewise continuous function of the form

$$Z(R) = \begin{cases} R_0/R & R \leq R_1 \\ Z(R_1)(R_1/R)^{p_1} & R_1 < R \leq R_2 \\ \vdots & \\ Z(R_n)(R_n/R)^{p_n} & R_n < R < \infty \end{cases} \tag{A-22}$$

Based on Equation A-22, complex path effects can be incorporated for a regional scale where not only waves propagate from source to site, but also waves are reflected by discontinuity in the crust and show an attenuation law in the far field which is different from

$1/R$. Moreover, the site effects be represented by two filters

$$G(f) = A(f) \cdot D(f) \tag{A-23}$$

with $A(f)$ the local site response transfer function that accounts for propagation from bedrock to softer upper soil strata and $D(f)$, a filter to account for an observed decrease of the spectral levels at high frequencies, which is independent of the path and can be attributed either to source (Papageorgiou & Aki, 1983) or local site conditions (Hanks & McGuire, 1981). $A(f)$ need not be a frequency domain filter, in fact, some authors (Hartzell et al., 2002) use a type of nonlinear filter that accounts for hysteretic behavior in the soil layers. This filter requires careful study and calibration of the site conditions and ground response. On the other hand, $D(f)$ is usually chosen to be either

$$D(f) = \left[1 + (f/f_{\text{max}})^8\right]^{-1/2} \qquad \text{or} \qquad D(f) = \exp\{-\pi\kappa_0 f\} \tag{A-24}$$

denoted respectively f_{max} filter or the κ (kappa) filter. Both filters are interchangeable, as shown elsewhere (Boore, 1986), if $f_{\text{max}} = 1/(\pi\kappa_0)$.

Finally $I(f) = (j \cdot 2\pi f)^n$ represents the response of the instrument, with $n = 0$ for a displacement output, $n = 1$ for velocity, and $n = 2$ for acceleration output. An instrument transfer function is used typically to predict an instrumental response.

C.2. Low Frequency Pulse

The displacement sensitive component of our synthetic acceleration time-series are controlled by a deterministic low-frequency pulse given by the wavelet (Mavroeidis & Papageorgiou, 2003)

$$v(t) = \begin{cases} \frac{A}{2}\left[1 + \cos\left(\frac{2\pi f_p}{\gamma}(t - t_0)\right)\right]\cos\left(2\pi f_p(t - t_0) + \nu\right) & t_0 - \frac{\gamma}{2f_p} \le t \le t_0 + \frac{\gamma}{2f_p} \\ 0 & \text{, otherwise} \end{cases} \tag{A-25}$$

which corresponds to an amplitude modulated cosine with a prevailing frequency parameter f_p; A controls the peak velocity of the pulse (PGV); γ controls the oscillatory character of the pulse; t_0 is the time of occurrence of the peak of the envelope; and ν is the phase shift

of the modulated signal. All these parameters should be selected to be representative of the motion generated by earthquake being modeled at the site of measurement. By integrating the pulse with zero initial displacement, the final static displacement is given by

$$\Delta_{\text{static}} = \frac{A}{2\pi f_p} \cdot \frac{\sin(\pi\gamma)}{1-\gamma^2} \cos(\nu) \tag{A-26}$$

which equates with the final static displacement obtained from InSAR. The main hypothesis behind this model is that the high-frequency wave controls peak acceleration (PGA), while the pulse controls PGV, PGD, and final static displacement.

If f_p , γ and ν parameters were known, the static displacement requirement would be satisfied by solving for A in A-26. However, these parameters are not known a-priori and must be calibrated using the fault geometry, distance, moment and slip distribution.

C.3. Calibration of Wave Parameters

The work of Mavroeidis and Papageorgiou (Mavroeidis & Papageorgiou, 2003) present a scaling relationship for f_p with seismic moment of the form $\log T_P = 2.2 + 0.4M_w$, with where $T_p = 1/f_p$, assuming self-similar moment scaling.

Yet the database used to derive this relationship did not include stations with noticeable co-seismic displacement, which makes using it an unusable in this study as this is the main effect we seek to model. Instead, note that f_p is related with the time interval in Equation A-25 in which the pulse is defined and, by observation of real baseline-corrected time-series as shown in this study and in other studies (Emore et al., 2007; Mavroeidis & Papageorgiou, 2003), its length should be such that the co-seismic displacement occurs mainly within the time-span in which the strongest motions occur. This interval starts when the first S-waves arrive from the event nucleation and continues until all of the main asperities have slipped and the corresponding S-waves have reached the site. Intuitively if the rupture speed of the event is large (as in super-shear events) the co-seismic fling step pulse should resemble the step response of the crust or, if the rupture speed is very slow, then the co-seismic pulse should resemble the slip function convolved over the entire rupturing fault with the crustal impulse response. In general the observed co-seismic pulse should be something between

these to extremes, yet delimited to the time-span in which the strongest motion occurs. This work's proposal to obtain this time interval is to calculate a characteristic dimension of an equivalent fault with uniform slip equal to the average identified slip which outputs the same amount of total seismic moment as the real event. By using this characteristic length and the rupture speed, the pulse interval can be estimated, which is the time taken by a rupture with speed $y\beta$ to transverse this length. The characteristic length a that preserves the total released seismic moment and average slip is given by

$$a = \alpha\sqrt{\frac{M_0}{\mu\bar{D}}} \tag{A-27}$$

where $\bar{D}$ is the average slip on the extended fault model, μ the crustal shear modulus, M_0 the released seismic moment and α a shape factor. For a square fault shape $\alpha = 1$, whereas for a circular fault this factor is $\alpha = \frac{1}{\sqrt{\pi}}$. The chosen value for the Tocopilla event is $\alpha \approx 3$, which is equivalent to a rectangular fault with a 1:3 site aspect ratio. With the characteristic dimension, the model average rupture velocity (in the case of Tocopilla this is $y\beta = 3.09\,\frac{km}{s}$), and the fault to site geometry the pulse length is derived and the f_p parameter thus identified. The fault to site geometry produces a Doppler-like effect in the prevailing frequency because sites located in the rupture direction will experience a slightly higher prevailing frequency, due to coherent summation of traveling waves, which leads to a shorter pulse length. Sites orthogonal to rupture propagation will show no change in nominal f_p value while sites located away from rupture propagation will show a dilated pulse interval. This useful feature that models the directivity of the co-seismic pulse, in practise, has little effect on the final computed responses.

As noted by Papageorgiou, real ground motion records processed so as to preserve long-period motions show a fitted deterministic pulse γ parameters value close to unity while filtered records show values as high as 4 for this parameter. In this work the chosen value $\gamma = 1.1$, is somewhat arbitrary and should be the subject of careful study. The ν parameter provides additional modelling freedom as it controls the phase of the modulated waveform that comprises the pulse and, hence, the ratio of peak pulse displacement to final

static displacement. In this work it is made to vary, again somewhat arbitrarily but with physical sense in mind, with distance to site from 30° to 90° from the near to the far field, the 90° value implies no co-seismic deformation in the far-field. This variation models the physical fact that pulses which lead to a co-seismic displacement attenuate faster than directivity pulses, which are still seen in the far field, thus the far field will show the effects of a pulse which is co-seismic in genesis but yields no co-seismic displacement.

As mentioned earlier and based on another study (Emore et al., 2007) it is reasonable to expect that the co-seismic displacement occurs during the onset of strong motion which is governed by the arrival of the S-wave. Hence, the time delay t_0 for the peak of the pulse is chosen as the travel time for an S-wave from the main asperity to the observation site, which is found to be a reasonable assumption. This completes the calibration of the parameters of the chosen wavelet in Equation A-25.

Mavroeidis' work presents a complete parametric study of the wavelets in time and frequency domain which is useful for interpretation. For now, the feasibility of using this approach for earthquake modeling will be addressed and the subject of the correct scaling of these parameters for co-seismic and directivity pulses left for future research.

C.4. Combination of Waves

Spectra of high and low-frequency waves are combined into one single waveform which satisfies all of our conditions, i.e. to predict PGA levels for high frequencies with a reasonable accuracy and to double integrate to the observed co-seismic displacement. The stochastic high-frequency wave is filtered such that its spectrum does not overlap with the spectrum of the long-period wave. The wave is filtered by a non-causal bidirectional fourth order Butterworth high-pass filter so the phase of the signal remains unchanged. The cutoff frequency is chosen as $f_{\text{cut}} = 0.1\,\text{Hz}$.

The addition of both waves yields the final simulated ground-motion. Because stochastic simulation is unable to predict different ground motion components, the only difference between synthetic records will be found in the long-period wave which must integrate to

a different co-seismic displacement component value. Additional site features like topographic defects, softer strata, are not predicted by the model.

Appendix D. Additional Results

In what follows, the main results which support this thesis are presented in a graphical manner. Starting from interferometric results, through inverse processing and seismic record correction, to end with simulation results for Tocopilla 2007 results. The commentaries for these results can be found in the main document.

Additionally, some results for Pisco 2007 earthquake are presented yet these are not so favorably compared to available seismic records since these were not obtaine in rock. Still, results should prove valuable if a rational means for incorporating soil effects is implemented. They were generated using the same attenuation and duration model as the Tocopilla 2007 earthquake, and changing the faulting geometry to that of Pisco 2007 and simulating for the available sites (found at the CISMID website). There is little agreement due to soil modification of spectral amplifications. Still, the results are illustrative of the main differences between rock and soil sites.

D.1 Interferograms

Table D-1: SAR scene data for earthquakes used in this study. (D) denotes a descending pass and (A) an ascending pass.

Tocopilla 2007 Earthquake

Satellite	Master Date	Slave Date	Path	Frames	$B_\perp$ (m)	Pass
ALOS	10/14/2007	29/11/2007	103	6720, 6730, 6740	538	A
ENVISAT	5/11/2007	10/12/2007	096	4041, 4059, 4077	178	D
ENVISAT	20/10/2007	24/11/2007	368	4041, 4059, 4077	271	D

Pisco 2007 Earthquake

Satellite	Master Date	Slave Date	Path	Frames	$B_\perp$ (m)	Pass
ALOS	10/8/2007	25/9/2007	110	6890 to 6920	100	A
ALOS	12/7/2007	27/8/2007	111	6890 to 6920	100	A

Antofagasta 1995 Earthquake[†]

Satellite	Master Date	Slave Date	Path	Frames	$B_\perp$ (m)	Pass
ERS-1	16/4/1995	30/7/1995	096	4059, 4077, 4095	$\approx$200	D
ERS-1	14/7/1995	18/8/1995	368	4059, 4077	$\approx$50	D

[†] After Pritchard et. Al.

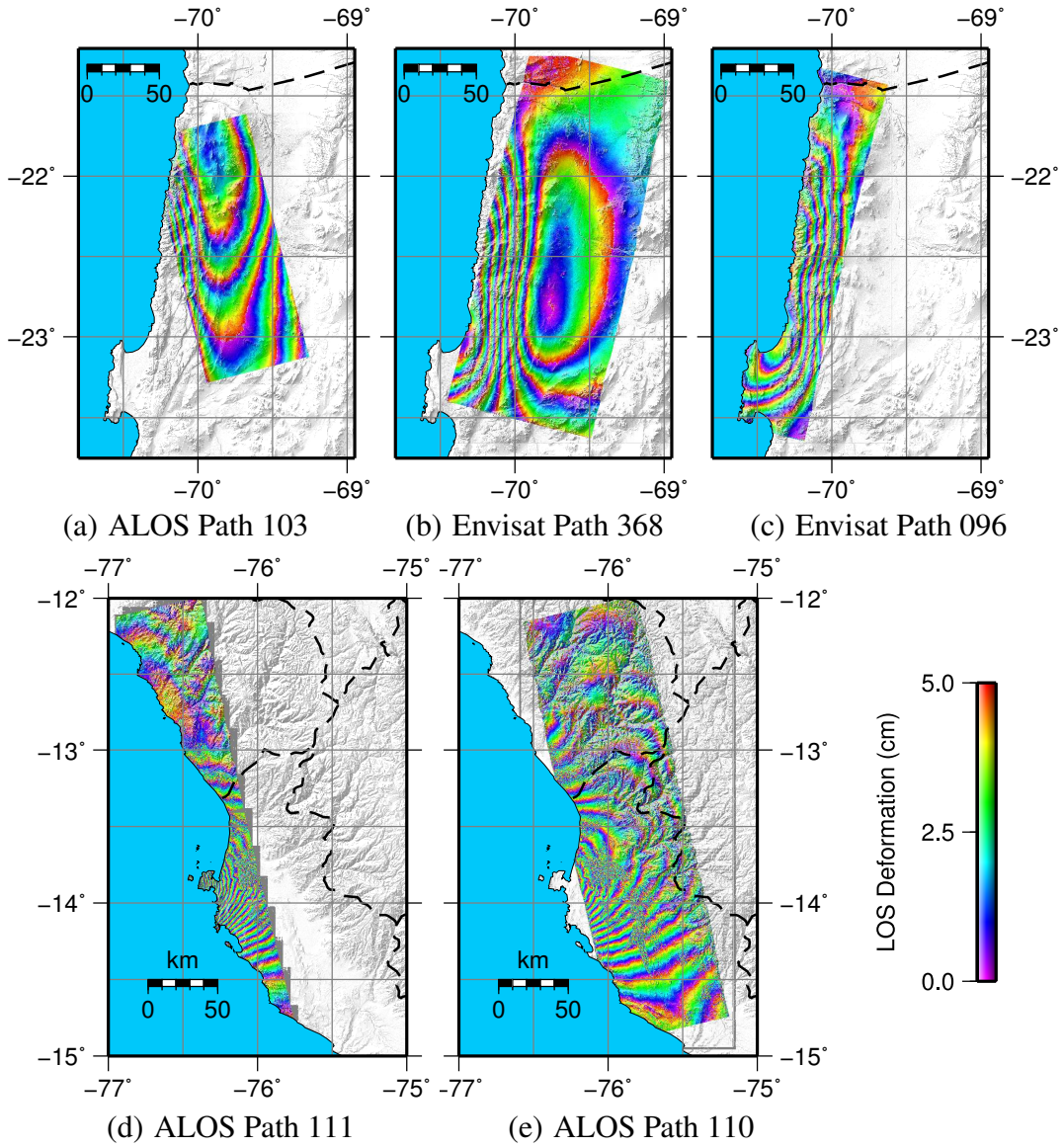

(a) ALOS Path 103 (b) Envisat Path 368 (c) Envisat Path 096

(d) ALOS Path 111 (e) ALOS Path 110

Figure D.1: Interferograms used for inversion of data. Figures (a), (b) and (c) show the images for the Tocopilla (2007) earthquake, and figures (d) and (e) the ones for the Pisco (2007) event.

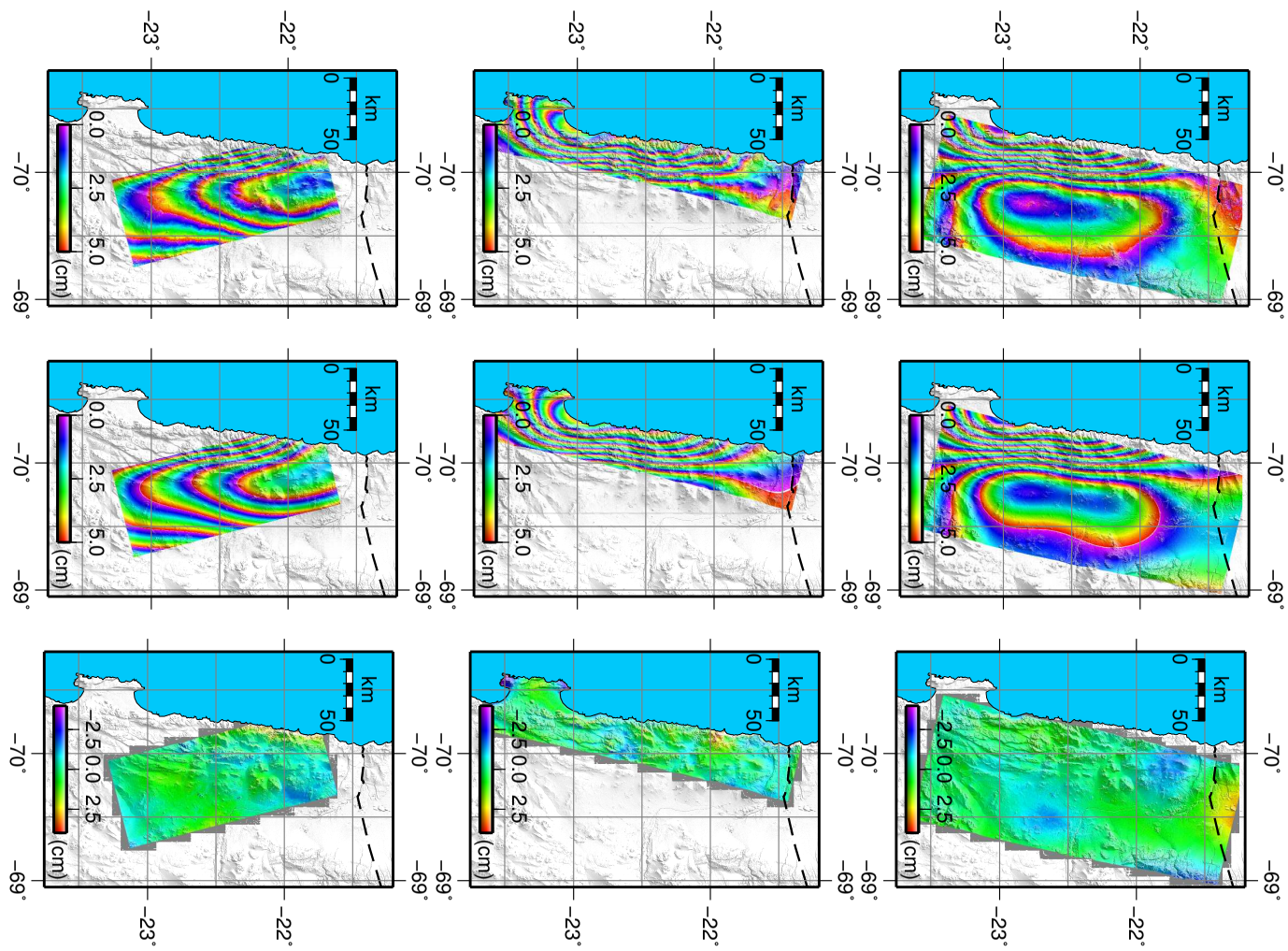

Figure D.2: Comparison of predicted InSAR interferograms with measured results for Tocopilla Earthquake. First column real interferogram, second column synthetic interferogram, third column shows inversion residuals. First row shows ENVISAT path 096, second ENVISAT path 368 and third ALOS Path 103

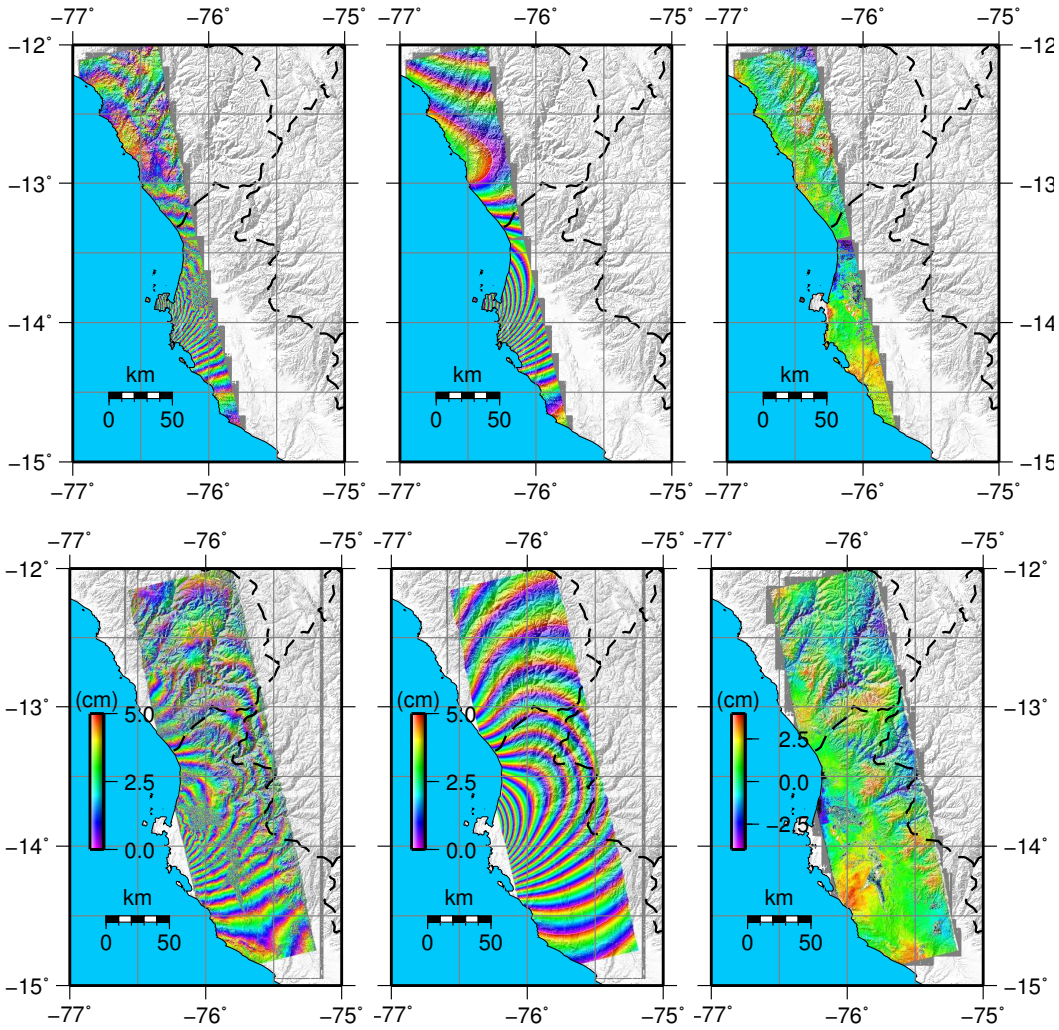

Figure D.3: Comparison of predicted InSAR interferograms with measured results for Pisco 2007 Earthquake. First column real interferogram, second column synthetic interferogram, third column shows inversion residuals. First row shows ALOS Path 110 and the second ALOS path 111

D.2 Inversion Results

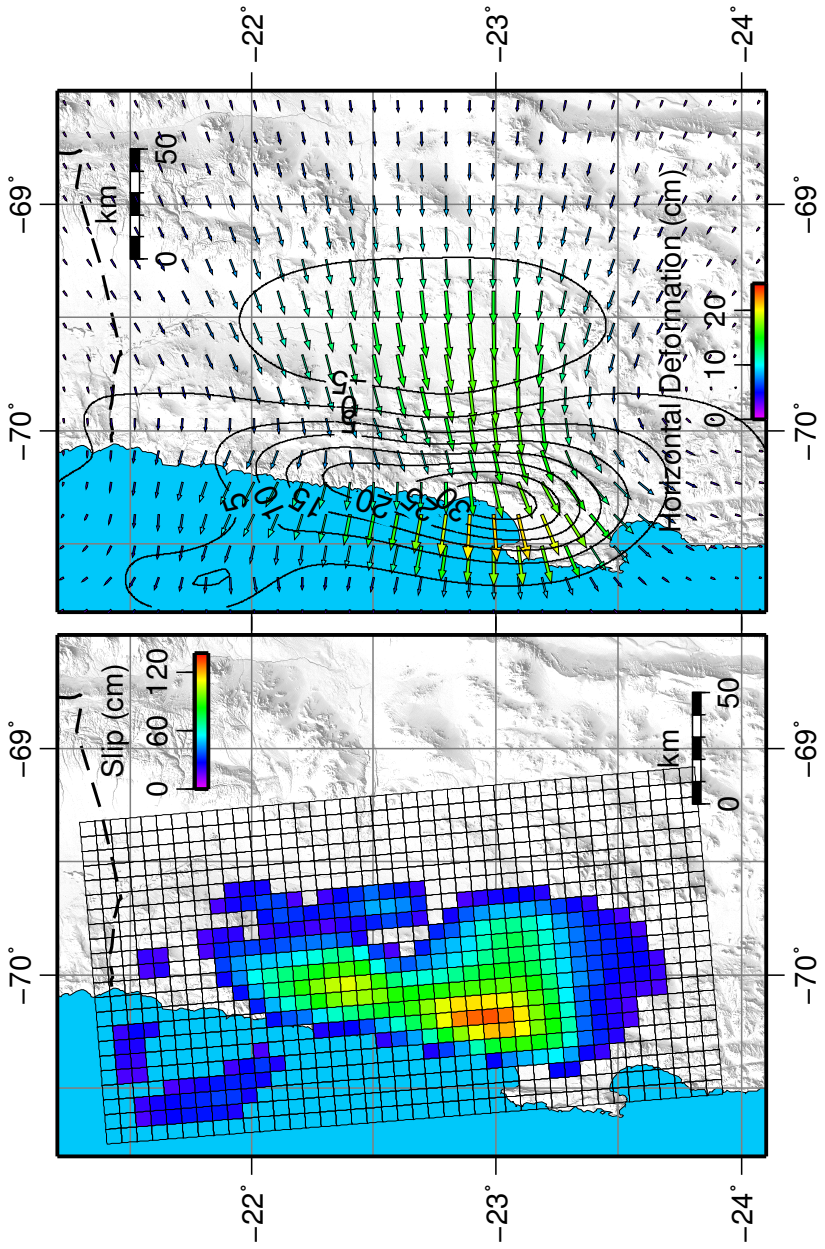

Figure D.4: Preferred slip model for Tocipilla 2007 earthquake derived from InSAR displacements and corresponding crustal deformation field.

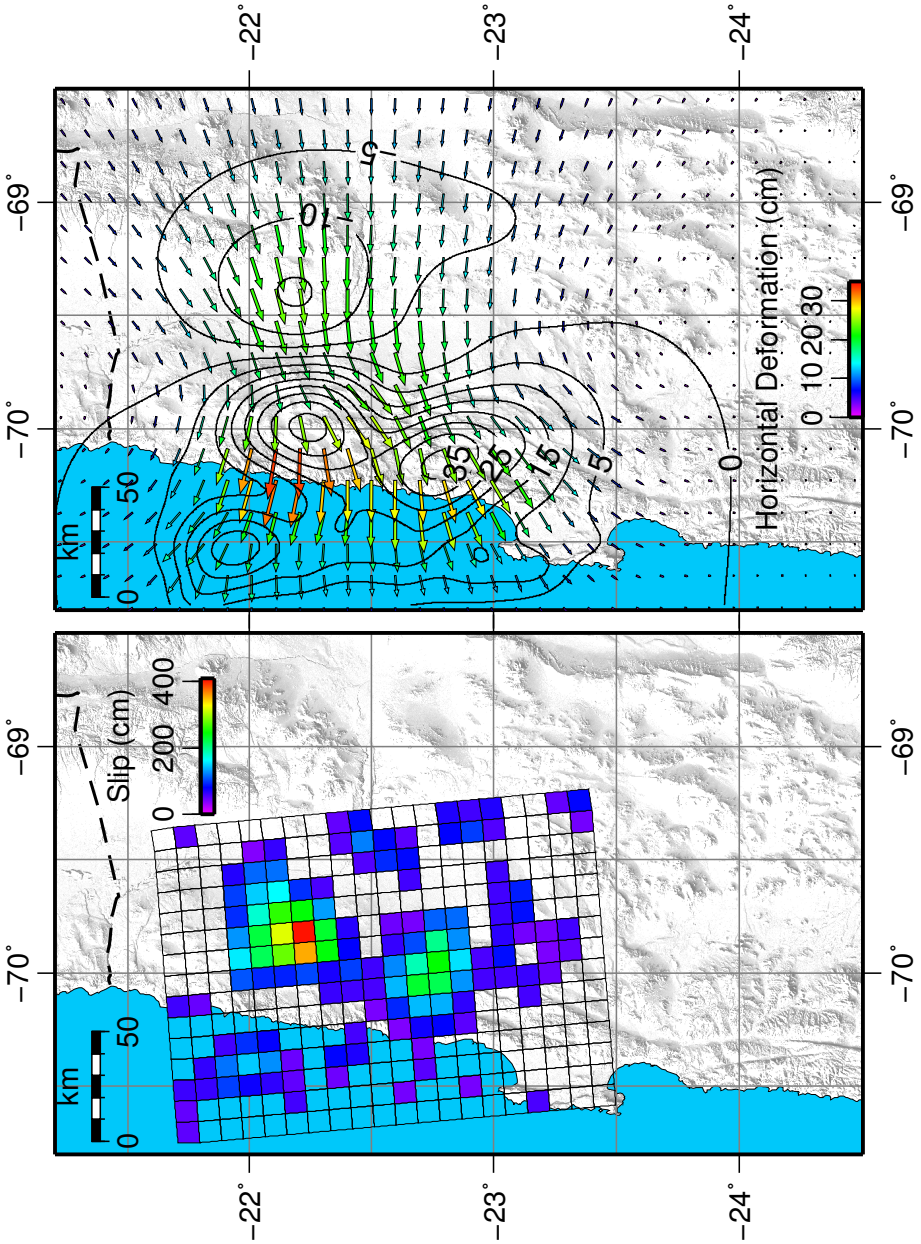

Figure D.5: For comparison purposes, the following is the slip model for the Tocopilla 2007 earthquake as derived from teleseismic waveform inversions (USGS) and it's implied crustal deformation field. Note the drastic differences from the preferred model which predicts the InSAR measurements well.

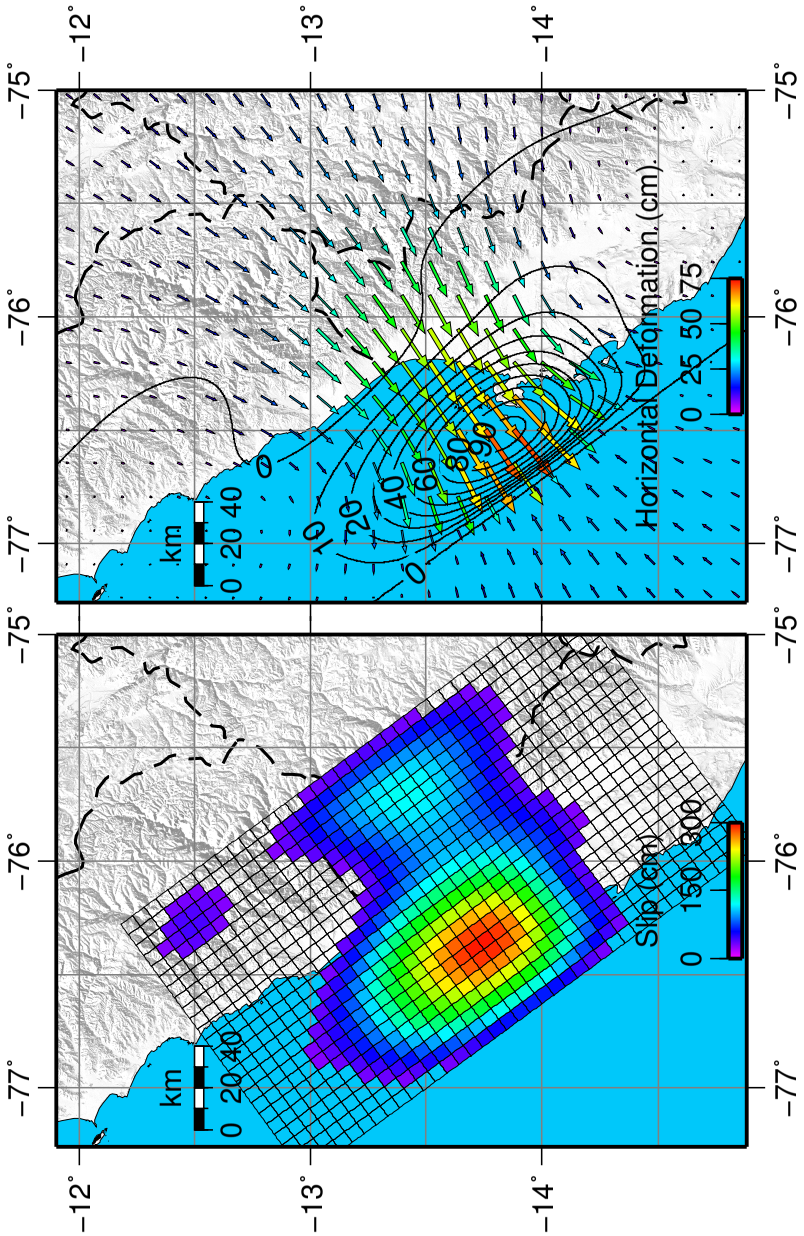

Figure D.6: Preferred slip model for the Pisco 2007 earthquake derived from InSAR displacements and corresponding crustal deformation field.

D.3 Acceleration Data

D.3.1 Tocopilla Earthquake: Station Layout

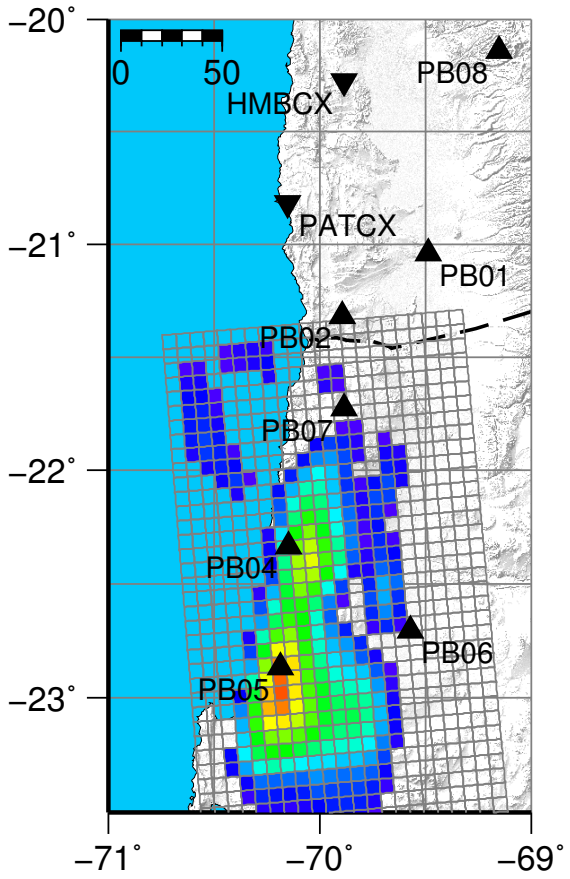

Figure D.7: The image shows station layout with respect to the identified faulting mechanism where ▲ represents GFZ Potsdam (German) stations and ▼ the IPGP (French) stations.

D.3 Acceleration Data

D.3.2 Tocopilla Earthquake: Baseline Correction

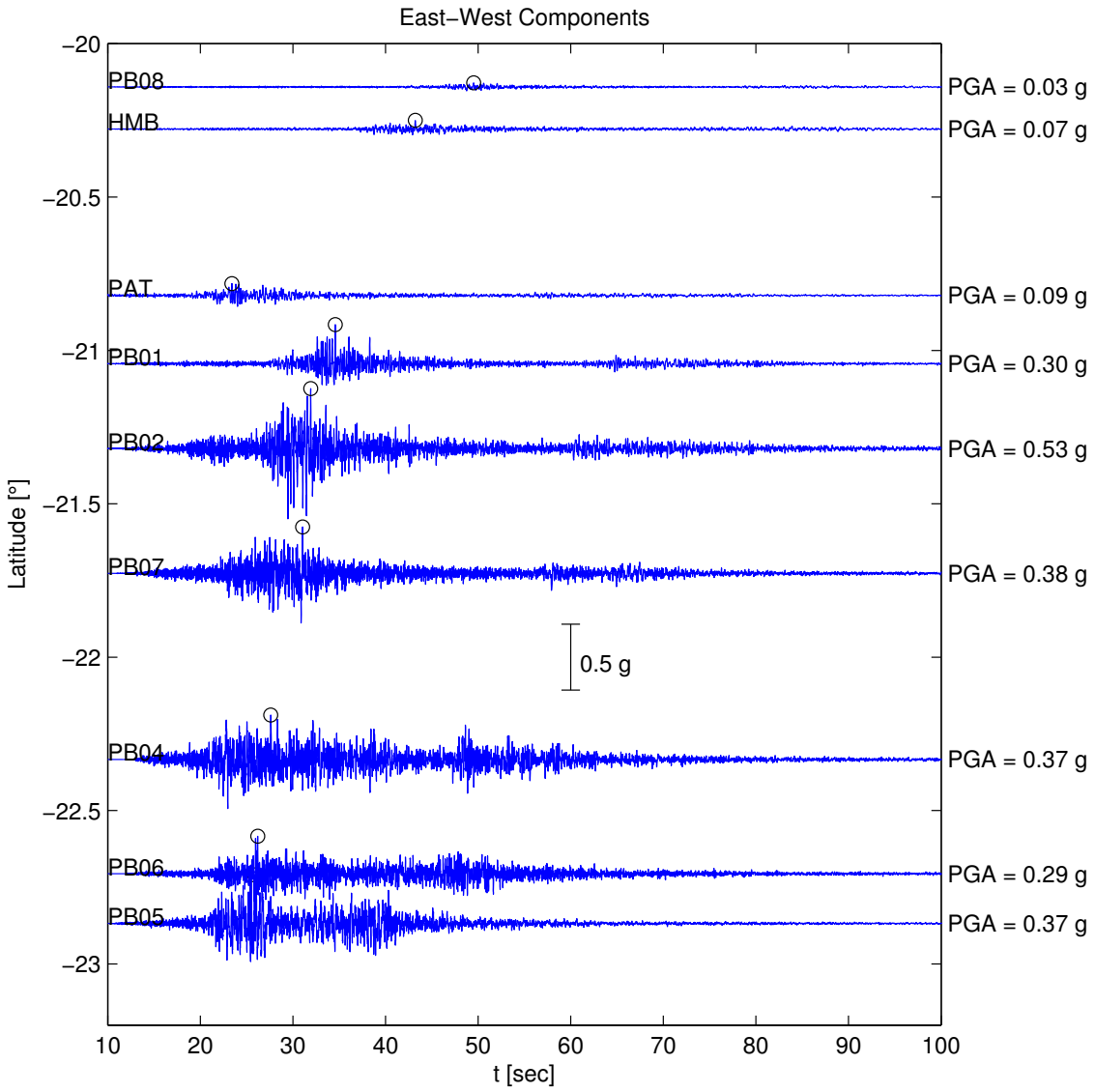

Figure D.8: Acceleration baseline correction results. The image shows the corrected east-west acceleration traces for the Tocopilla 2007 earthquake recorded on the IPOC network. On the vertical axis is the latitude coordinate of the stations, the acceleration traces are presented on a different scale.

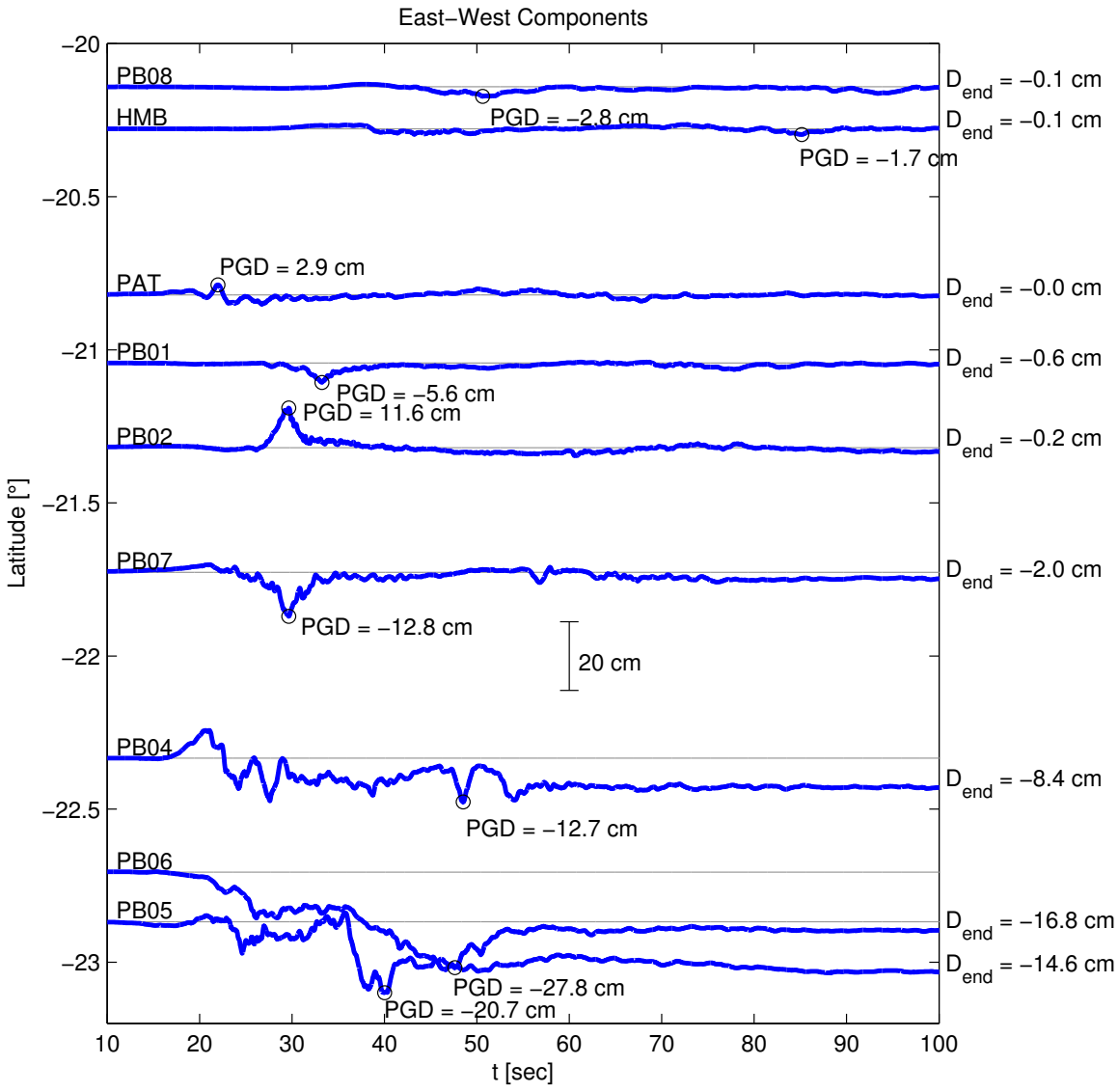

Figure D.9: Acceleration baseline correction results. The image shows the corrected east-west displacement traces for the Tocopilla 2007 earthquake recorded on the IPOC network. On the vertical axis is the latitude coordinate of the stations, the displacements are presented on a different scale.

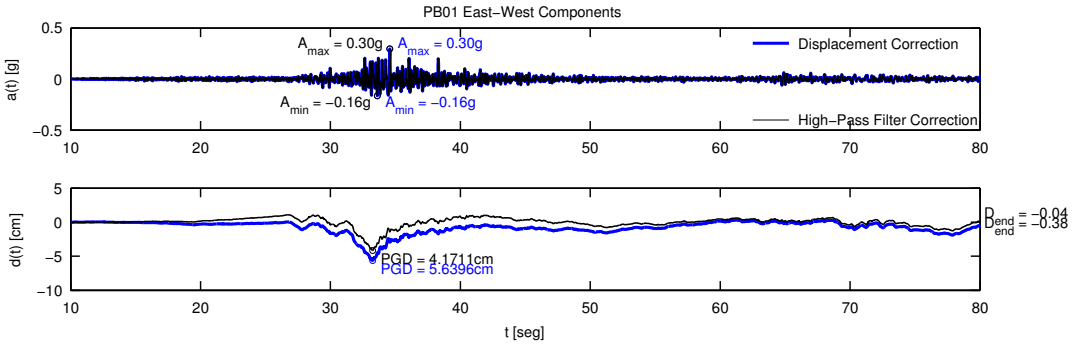

(a) East-West

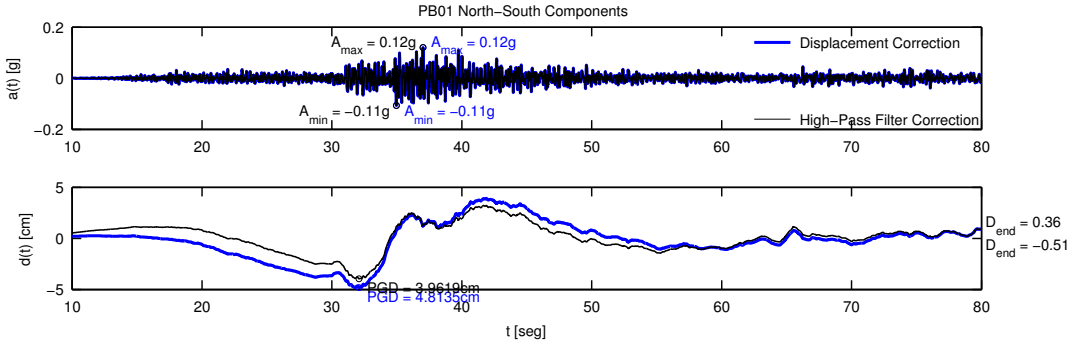

(b) North-South

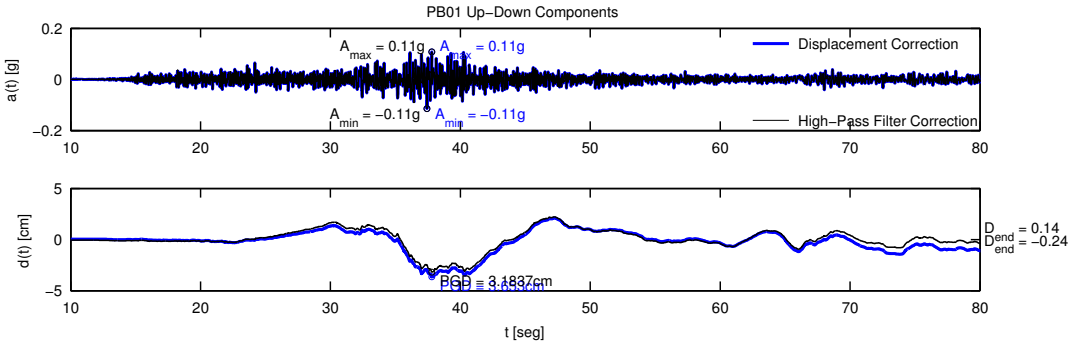

(c) Up-Down

Figure D.10: Comparison of resulting displacement and acceleration time series for station PB01 by correction with two methods. The black line represents theresulting time series by correction with bandpass filtering (0.01 - 25 Hz passband.), while the blue line represents the proposed baseline correction.

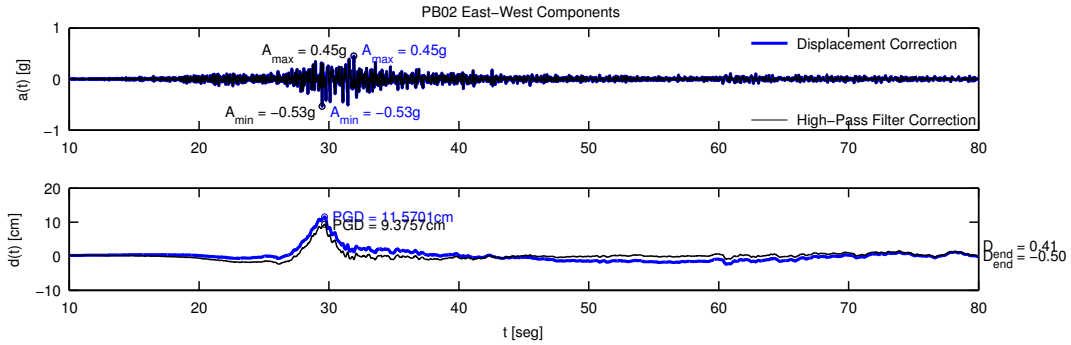

(a) East-West

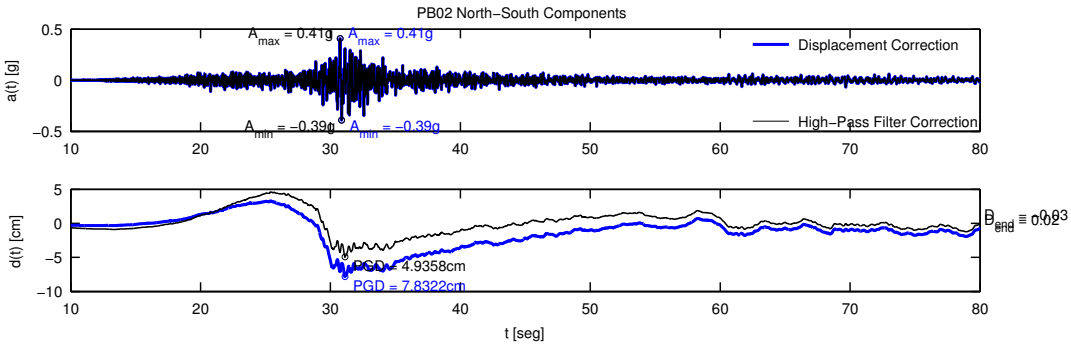

(b) North-South

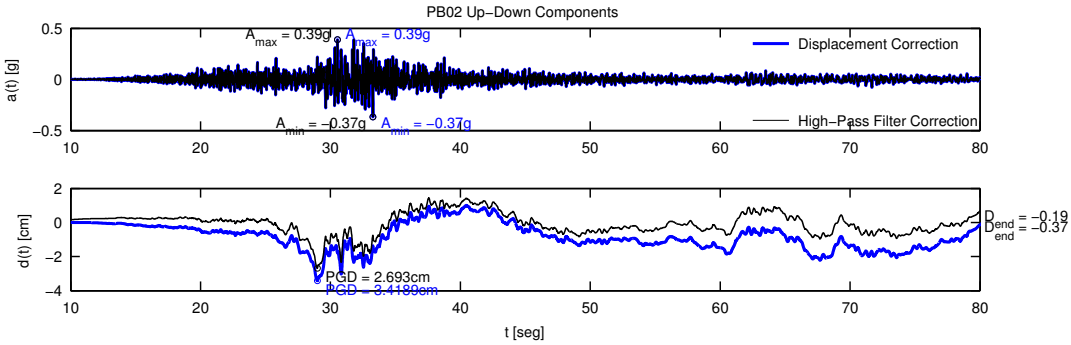

(c) Up-Down

Figure D.11: Comparison of resulting displacement and acceleration time series for station PB02 by correction with two methods. The black line represents theresulting time series by correction with bandpass filtering (0.01 - 25 Hz passband.), while the blue line represents the proposed baseline correction.

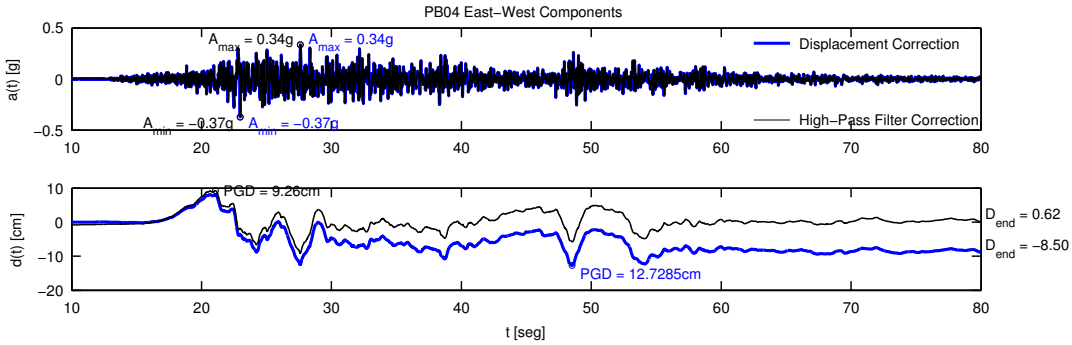

(a) East-West

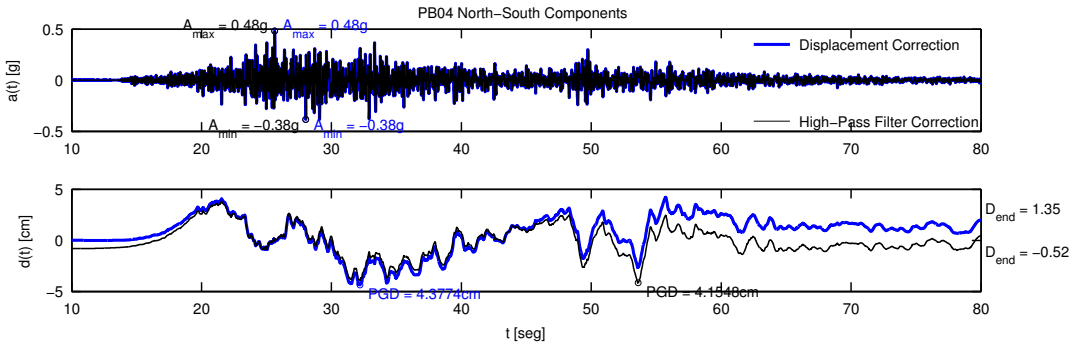

(b) North-South

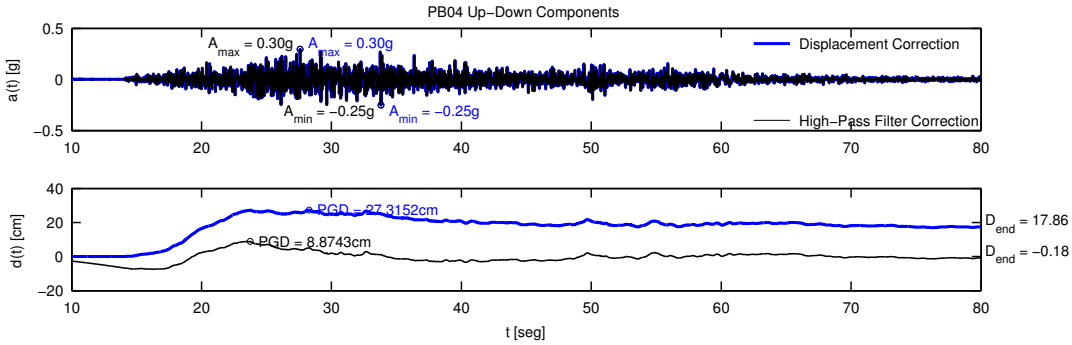

(c) Up-Down

Figure D.12: Comparison of resulting displacement and acceleration time series for station PB04 by correction with two methods. The black line represents theresulting time series by correction with bandpass filtering (0.01 - 25 Hz passband.), while the blue line represents the proposed baseline correction.

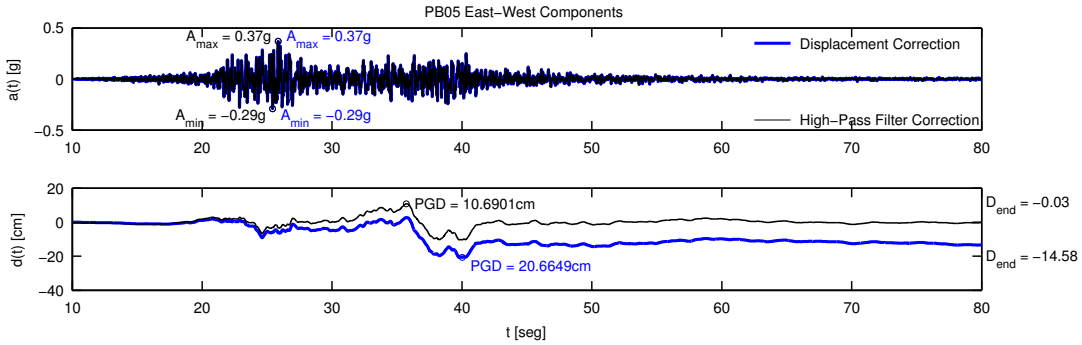

(a) East-West

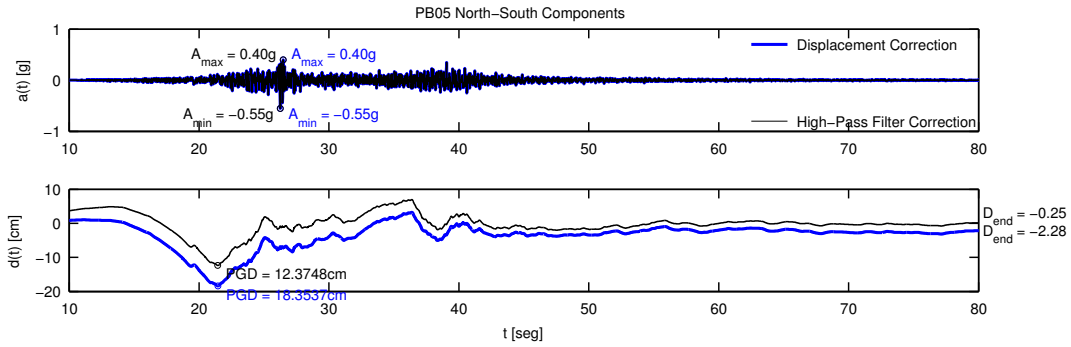

(b) North-South

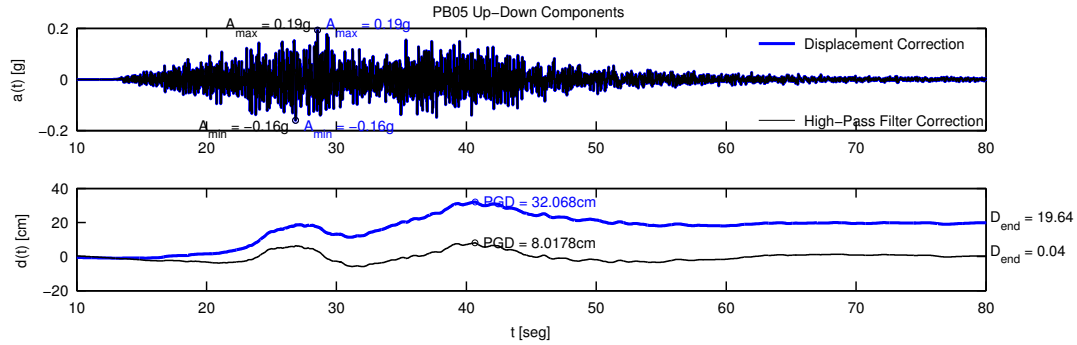

(c) Up-Down

Figure D.13: Comparison of resulting displacement and acceleration time series for station PB05 by correction with two methods. The black line represents theresulting time series by correction with bandpass filtering (0.01 - 25 Hz passband.), while the blue line represents the proposed baseline correction.

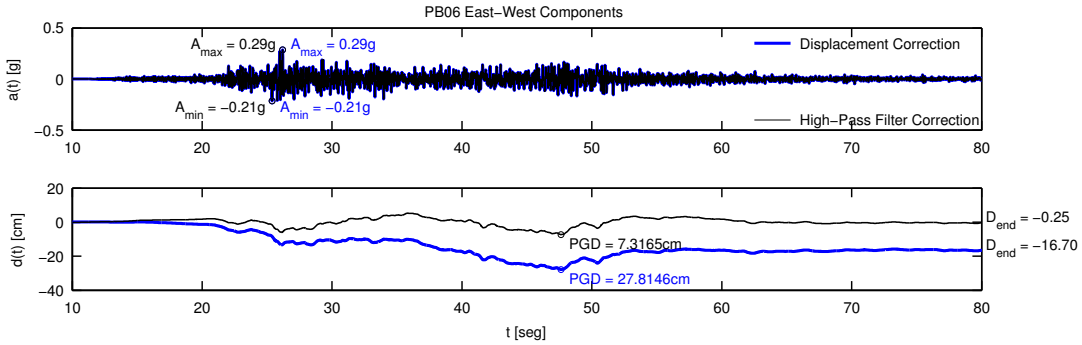

(a) East-West

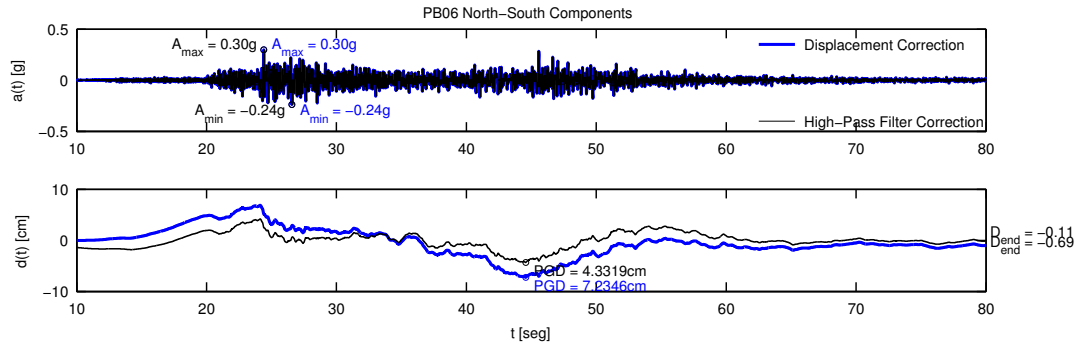

(b) North-South

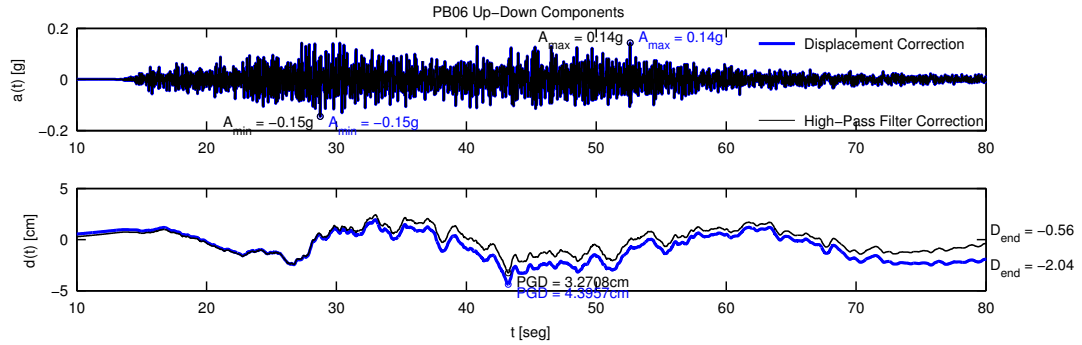

(c) Up-Down

Figure D.14: Comparison of resulting displacement and acceleration time series for station PB06 by correction with two methods. The black line represents theresulting time series by correction with bandpass filtering (0.01 - 25 Hz passband.), while the blue line represents the proposed baseline correction.

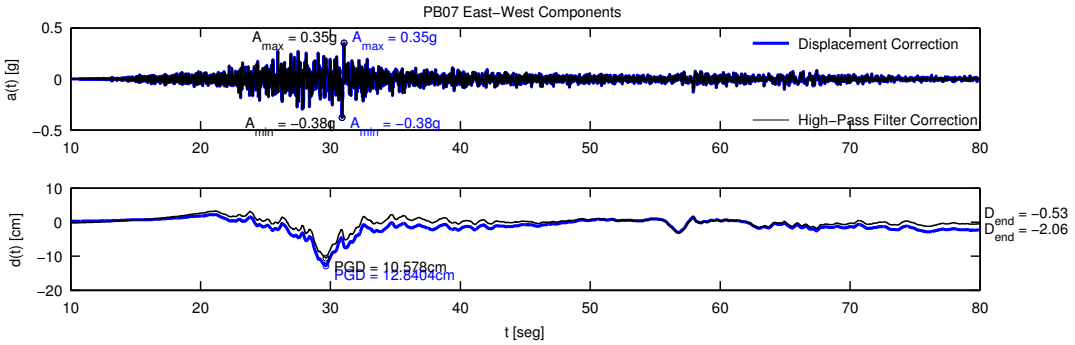

(a) East-West

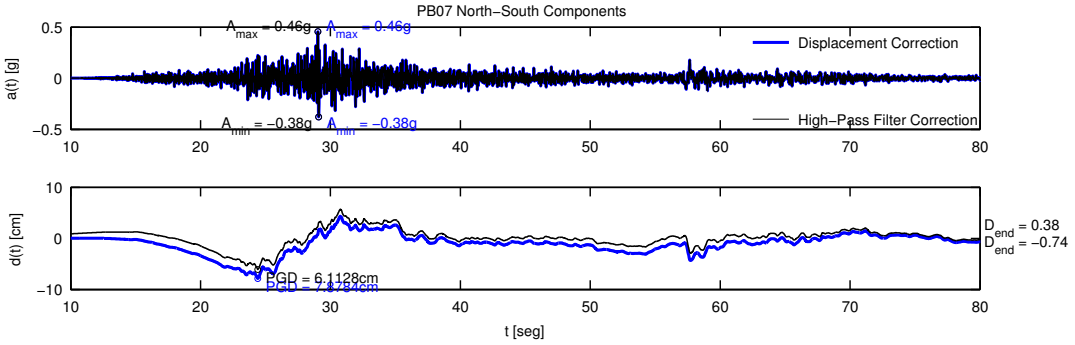

(b) North-South

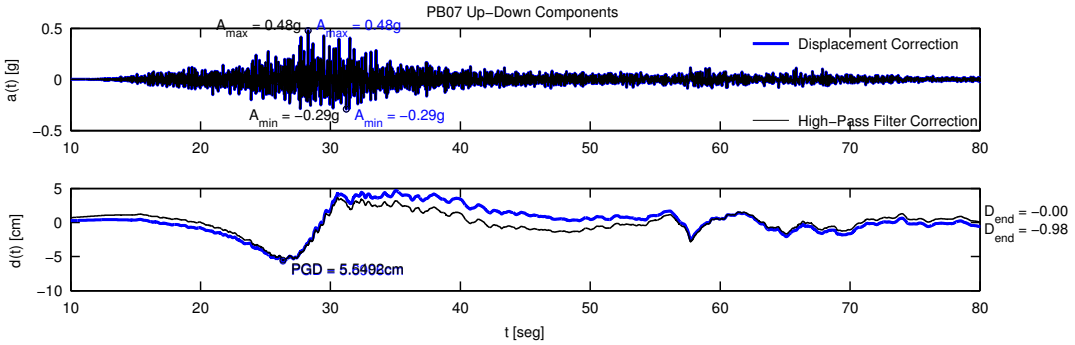

(c) Up-Down

Figure D.15: Comparison of resulting displacement and acceleration time series for station PB07 by correction with two methods. The black line represents theresulting time series by correction with bandpass filtering (0.01 - 25 Hz passband.), while the blue line represents the proposed baseline correction.

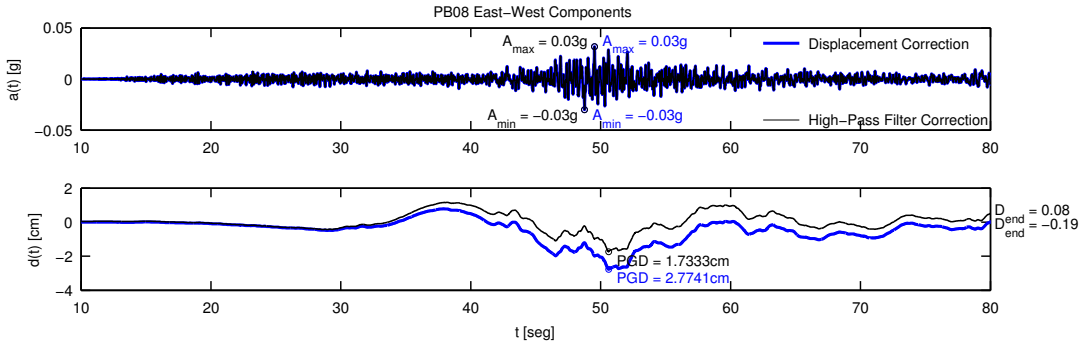

(a) East-West

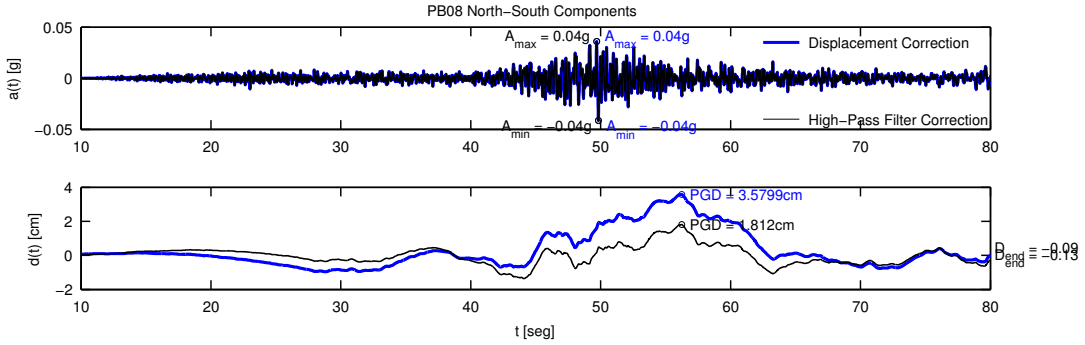

(b) North-South

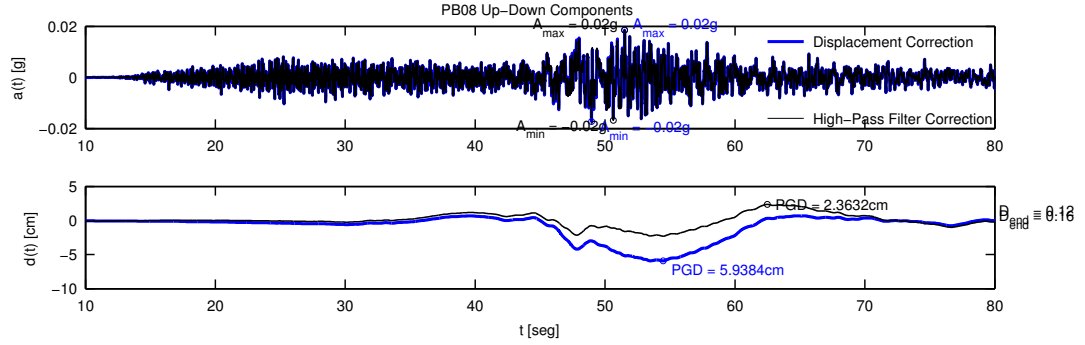

(c) Up-Down

Figure D.16: Comparison of resulting displacement and acceleration time series for station PB08 by correction with two methods. The black line represents theresulting time series by correction with bandpass filtering (0.01 - 25 Hz passband.), while the blue line represents the proposed baseline correction.

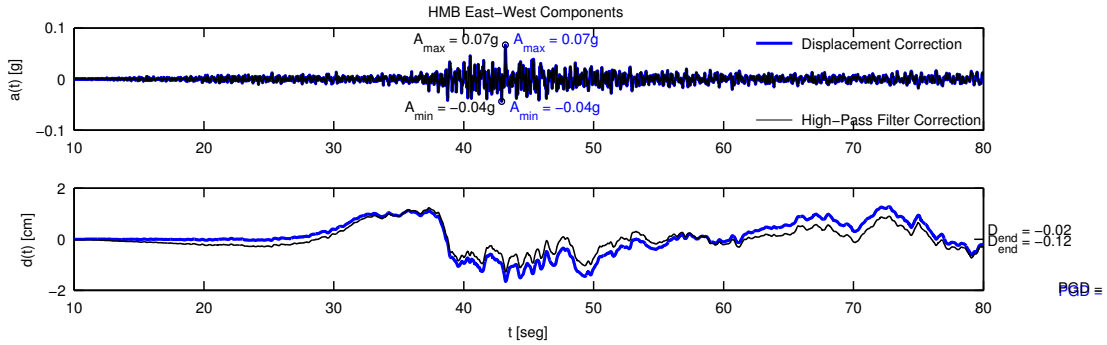

(a) East-West

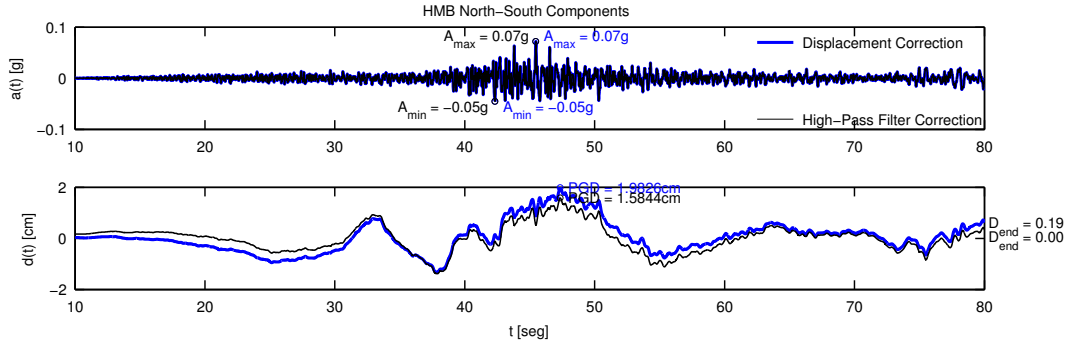

(b) North-South

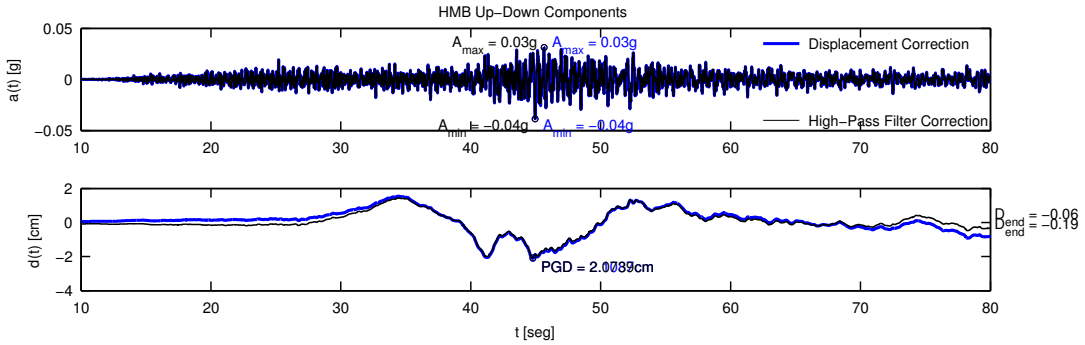

(c) Up-Down

Figure D.17: Comparison of resulting displacement and acceleration time series for station HMB by correction with two methods. The black line represents theresulting time series by correction with bandpass filtering (0.01 - 25 Hz passband.), while the blue line represents the proposed baseline correction.

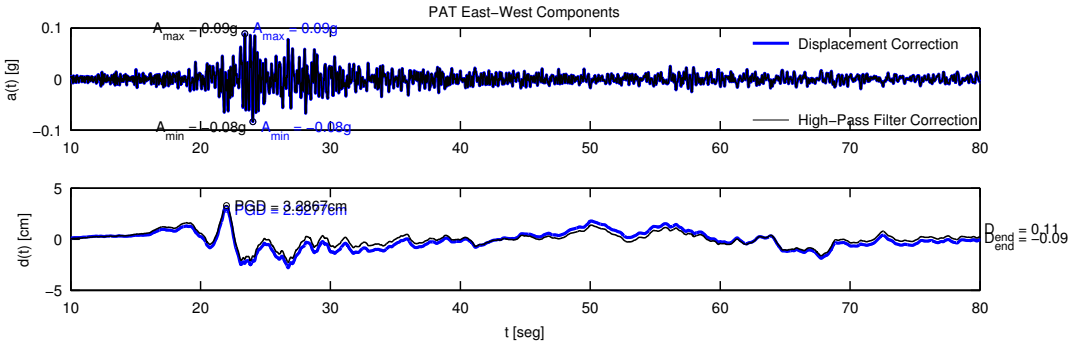

(a) East-West

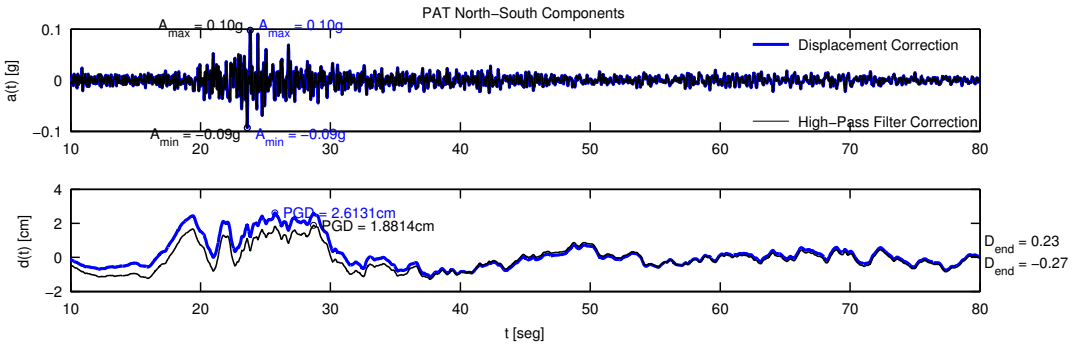

(b) North-South

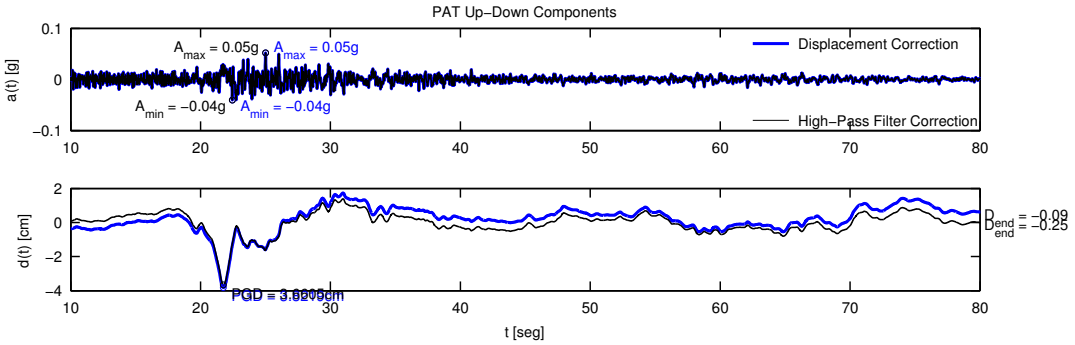

(c) Up-Down

Figure D.18: Comparison of resulting displacement and acceleration time series for station PAT by correction with two methods. The black line represents theresulting time series by correction with bandpass filtering (0.01 - 25 Hz passband.), while the blue line represents the proposed baseline correction.

D.3 Acceleration Data

D.3.3 Tocopilla Earthquake: Comparison of displacement spectra by two methods.

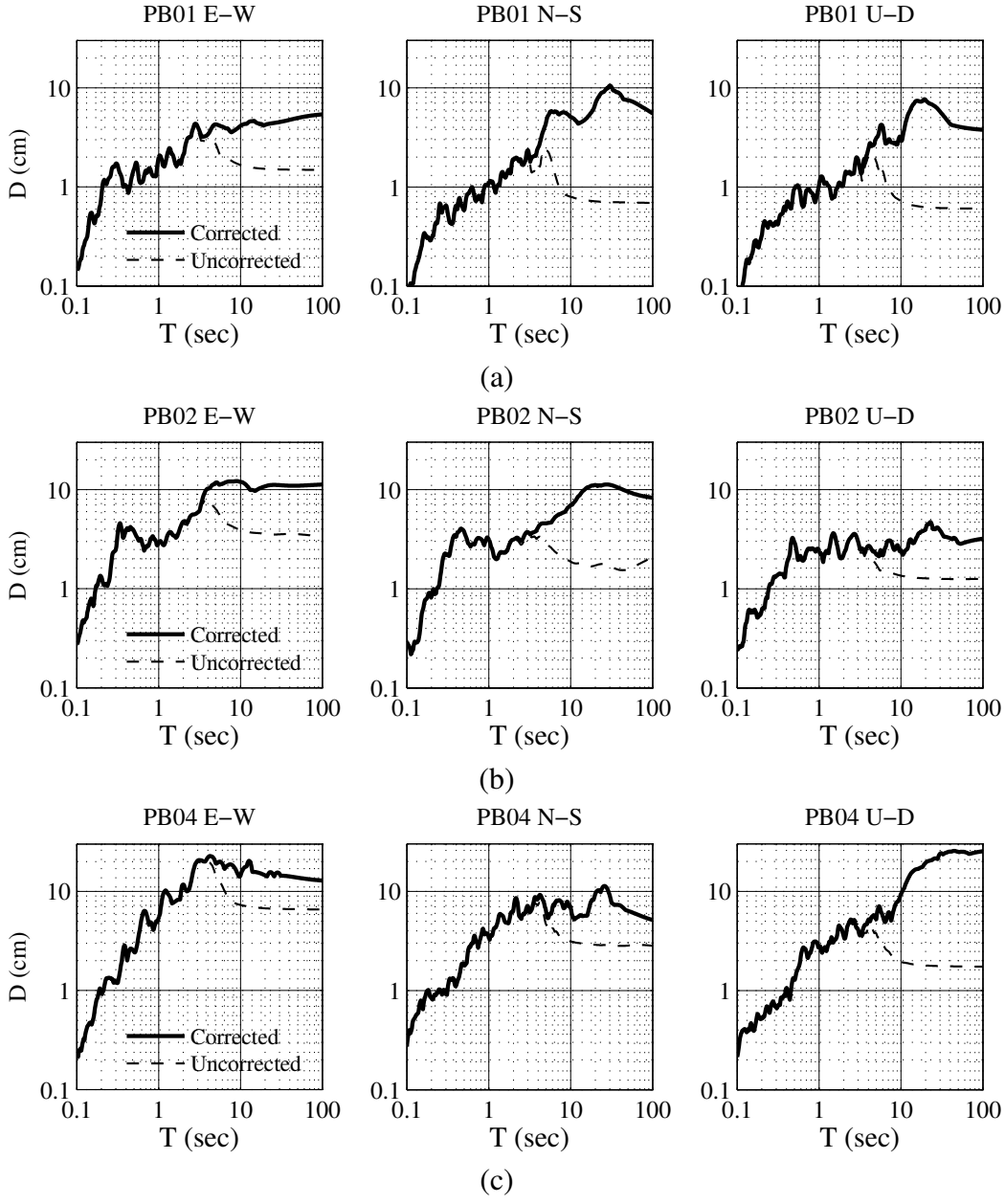

Figure D.19: The solid line represents the response spectra for stations PB01, PB02 and PB04 due to the Tocopilla 2007 earthquake when corrected with displacement-compatible method, the dashed line represents the case when the correction is done by classical filtering.

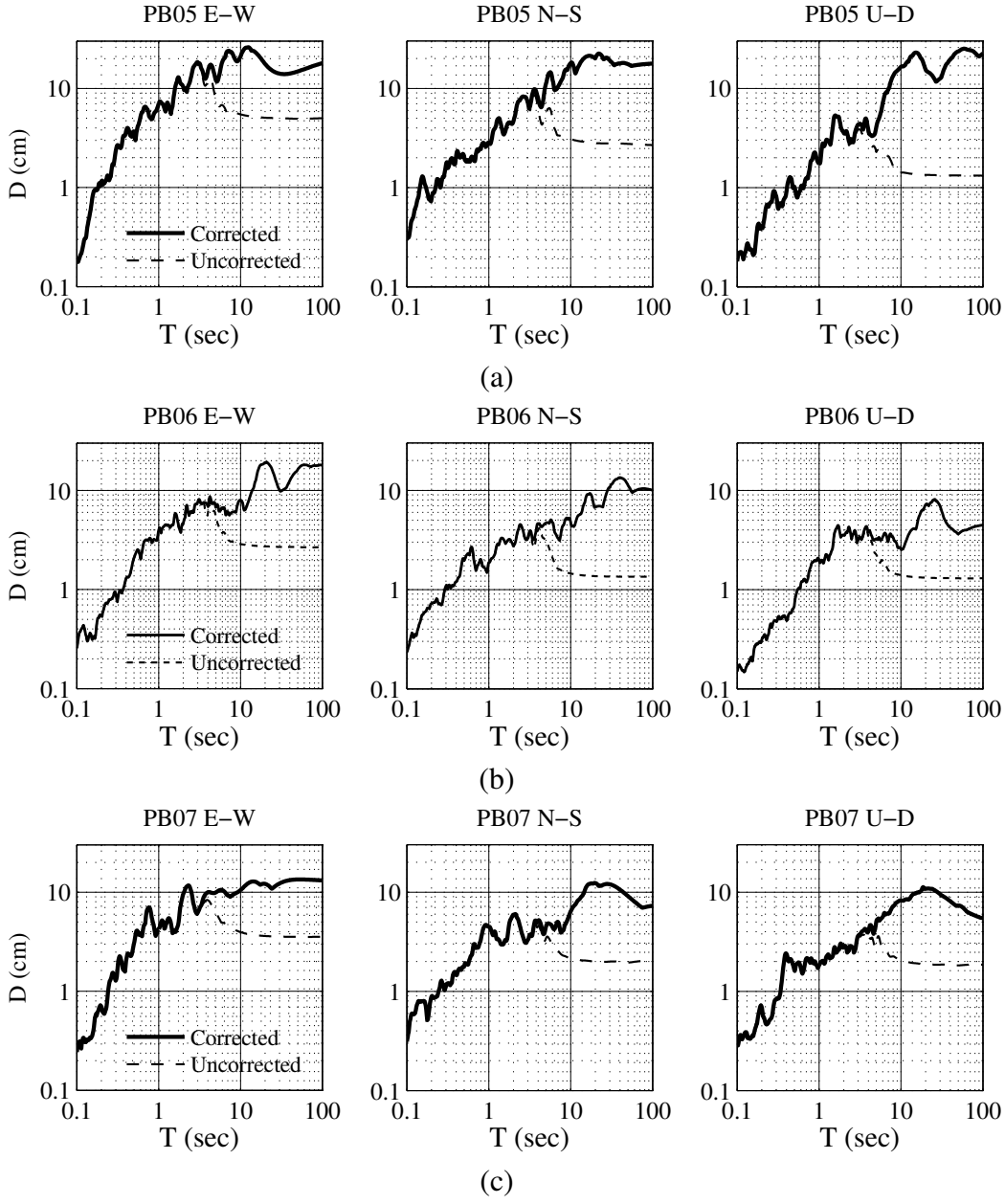

Figure D.20: The solid line represents the response spectra for stations PB05, PB06 and PB07 due to the Tocopilla 2007 earthquake when corrected with displacement-compatible method, the dashed line represents the case when the correction is done by classical filtering.

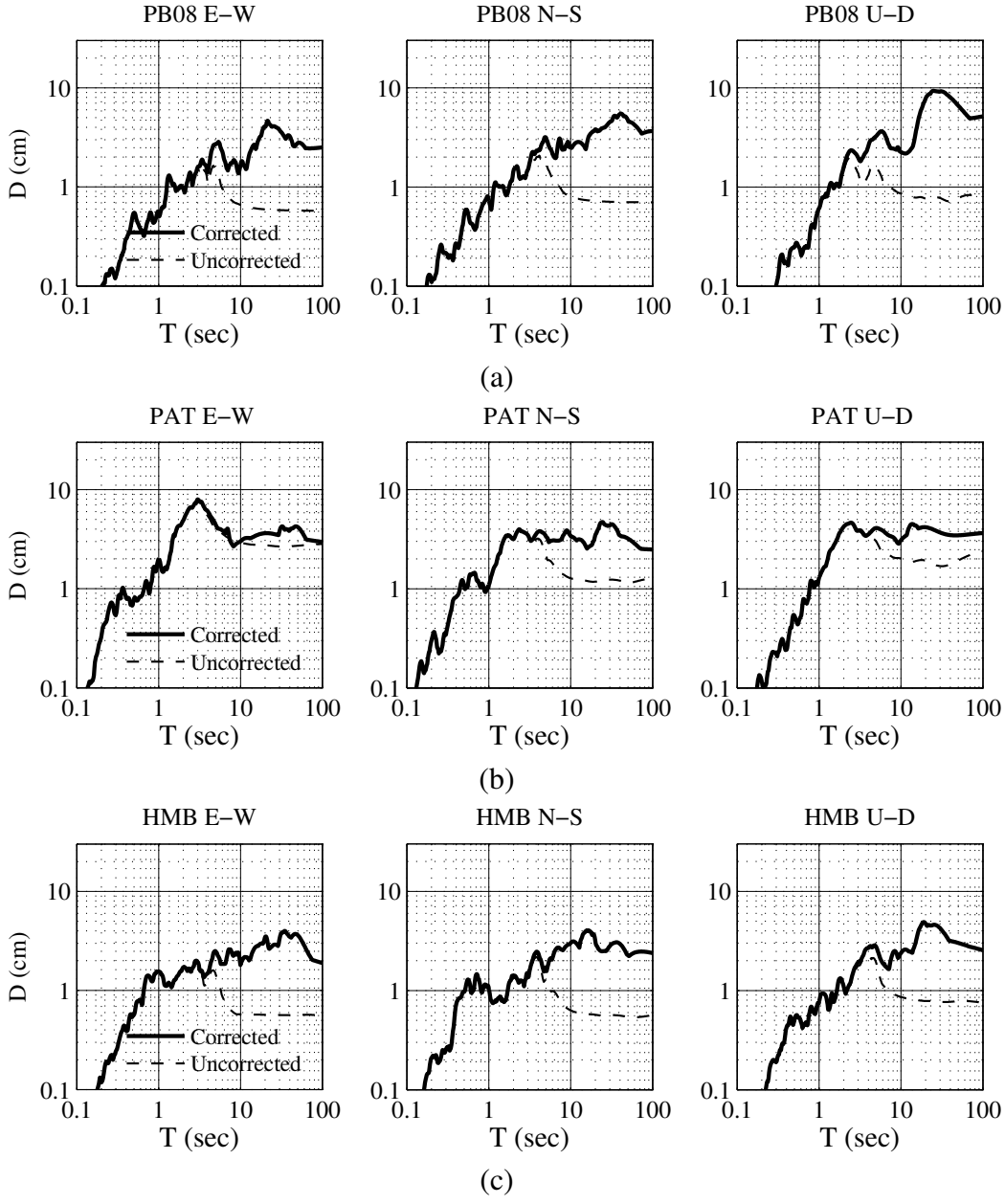

Figure D.21: The solid line represents the response spectra for stations PB08, PAT and HMB due to the Tocopilla 2007 earthquake when corrected with displacement-compatible method, the dashed line represents the case when the correction is done by classical filtering.

D.4 Acceleration Data

D.4.1 Tocopilla Earthquake: Corrected Tripartite Response Spectra

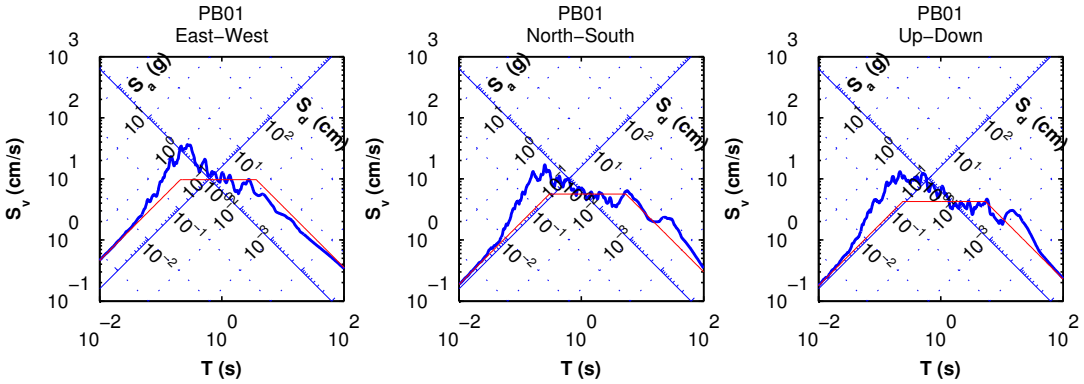

(a)

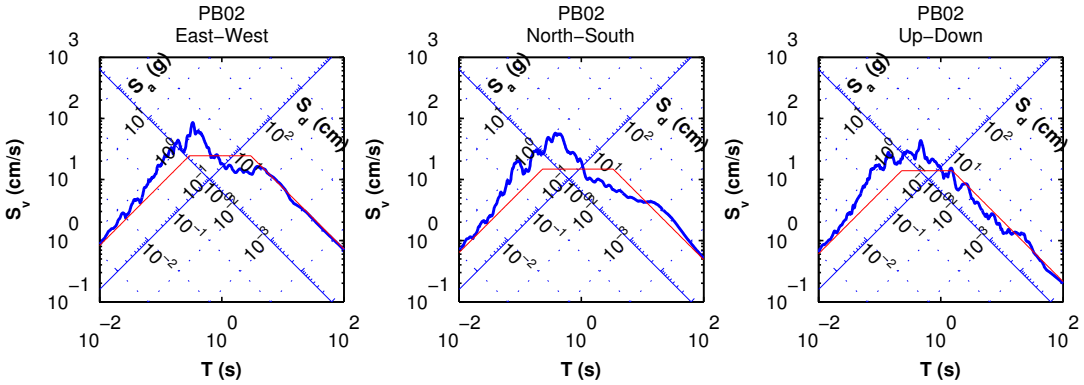

(b)

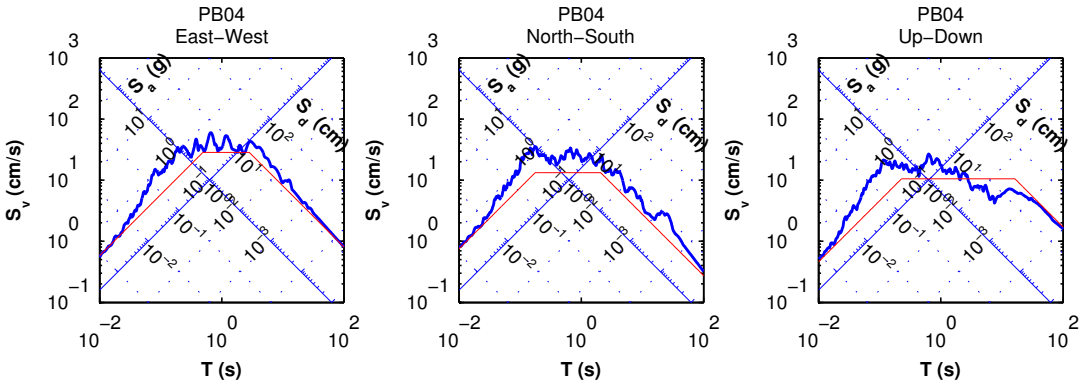

(c)

Figure D.22: Tripartite response spectra for stations PB01, PB02 and PB04 due to the Tocopilla 2007 earthquake when corrected with displacement-compatible method, the red lines represent the ground PGA, PGV and PDG.

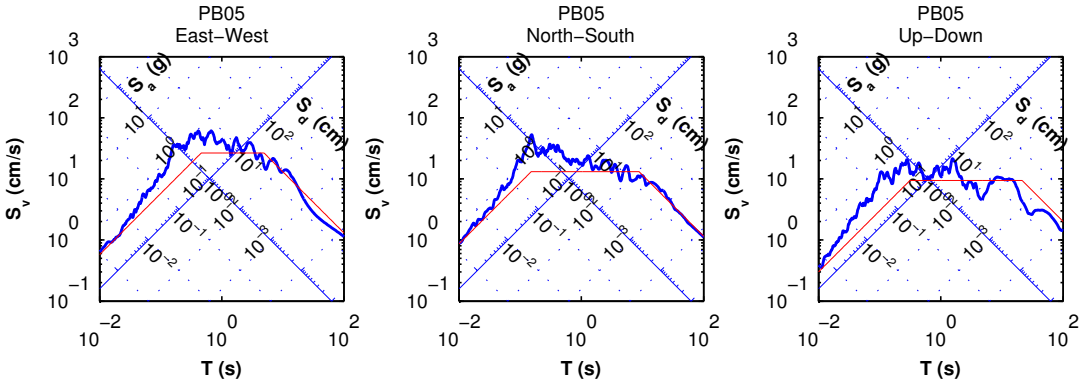

(a)

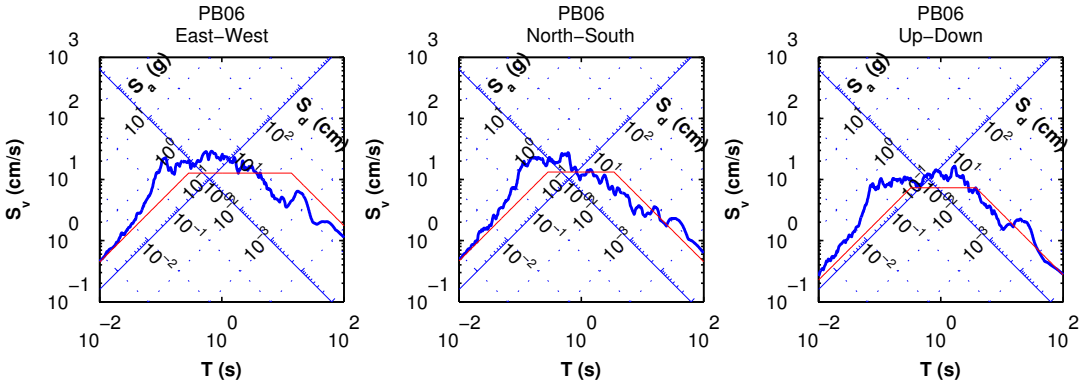

(b)

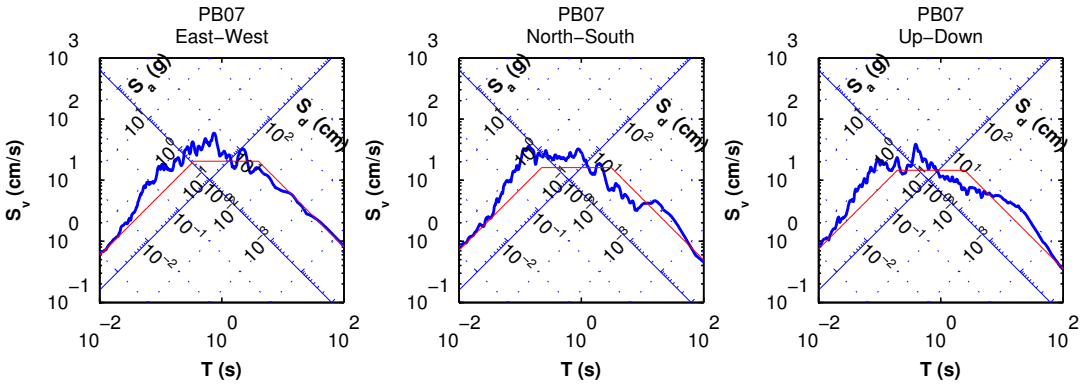

(c)

Figure D.23: Tripartite response spectra for stations PB05, PB06 and PB07 due to the Tocopilla 2007 earthquake when corrected with displacement-compatible method, the red lines represent the ground PGA, PGV and PDG.

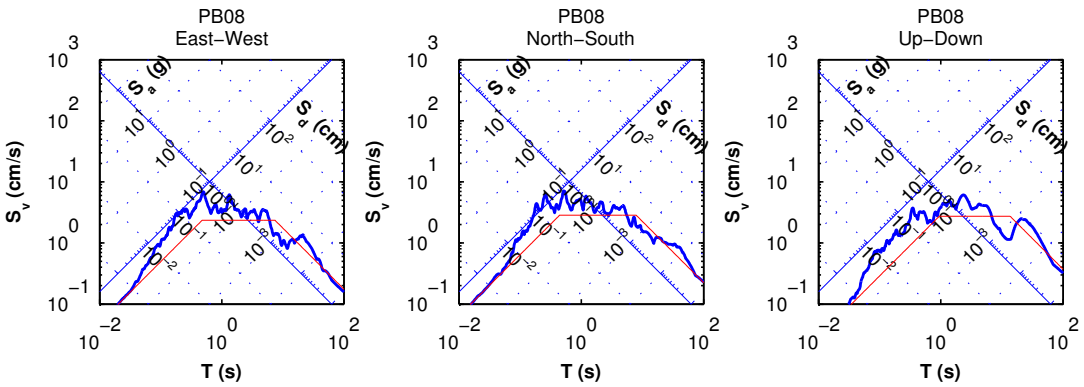

(a)

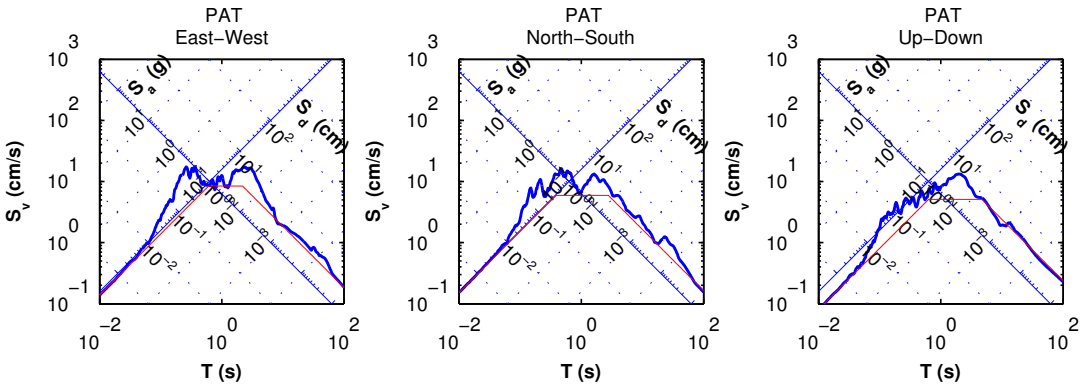

(b)

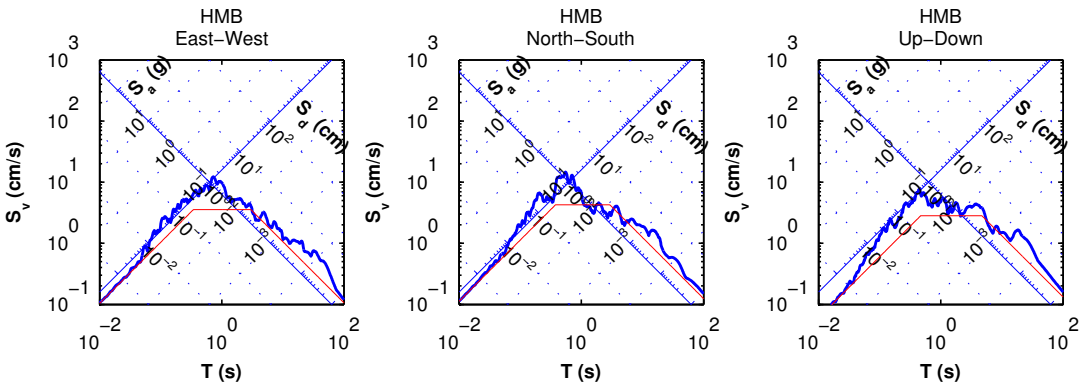

(c)

Figure D.24: Tripartite response spectra for stations PB08, PAT and HMB due to the Tocopilla 2007 earthquake when corrected with displacement-compatible method, the red lines represent the ground PGA, PGV and PDG.

D.4 Simulation Results

D.4.2 Tocopilla Earthquake: Fault Model

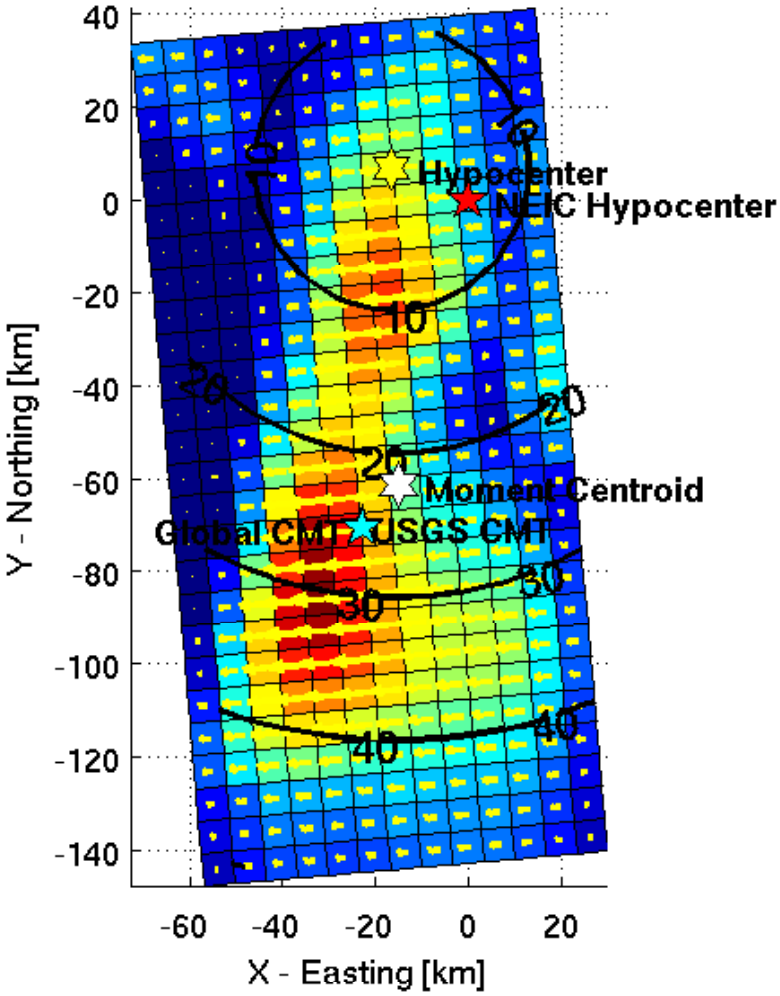

Figure D.25: The image shows a closer look at the fault model with the rupture isochrons and details of hypocenter and moment centroid with respect to those obtained from other sources.

Table D-2: Simulation parameters for Tocopilla 2007 earthquake used in this study.

Global Parameters		Attenuation	
$\beta = 3.63\,\text{km/s}$	$M_w = 7.7$	$Q_0 = 600$	$\eta = 0.4$
$\Delta\sigma = 75$	Pulsing Area $= 10\%$	$R_1 = 45\,\text{km}$	$p_1 = 1$
Hypocenter	$22.1417°S$, $70.0292°W$	$R_2 = 100\,\text{km}$	$p_2 = -0.1$
Depth:	$33.1595\,\text{km}$	$f_{\text{max}} = 10\,\text{Hz}$	$p_3 = 2$
$y = 0.85$	$\rho = 2.88\,\frac{\text{gr}}{\text{cm}^3}$		
Dip $= 16.65°$	Strike $= 355°$	Duration Model	
Length:	$182\,\text{km}$		
Width:	$91\,\text{km}$	$R_{\text{min}} = 45\,\text{km}$	$T_{\text{min}} = 0.5\,\text{s}$
Min. Depth:	$19\,\text{km}$	$R_1 = +\infty$	$b_1 = 0.04$

D.4 Simulation Results

D.4.3 Tocopilla Earthquake: Simulated Time Series

Table D-3: Station locations, hypocentral distance and elastic (Okada) coseismic displacements as implied by Tocopilla 2007 Earthquake finite fault model.

Station N°	Name	Lat [°]	Lon [°]	D_h [km]	δ_x [cm]	δ_z [cm]	δ_z [cm]
01	PB01	-21.043	-69.487	138.0	-0.66	-0.82	-0.44
02	PB02	-21.320	-69.896	097.8	-0.49	-0.25	-0.52
03	PB04	-22.334	-70.149	041.3	-10.51	+1.91	+23.57
04	PB05	-22.868	-70.186	088.5	-15.90	-2.12	+30.63
05	PB06	-22.706	-69.572	085.0	-18.31	-2.79	-10.56
06	PB07	-21.727	-69.886	058.6	-2.27	-0.79	-0.61
07	PB08	-20.141	-69.153	241.7	-0.23	-0.25	-0.15
08	HMB	-20.278	-69.888	209.5	-0.07	-0.04	-0.20
09	PAT	-20.821	-70.153	150.5	-0.07	+0.17	-0.28
10	PSG	-19.597	-70.123	283.8	-0.02	+0.02	-0.13

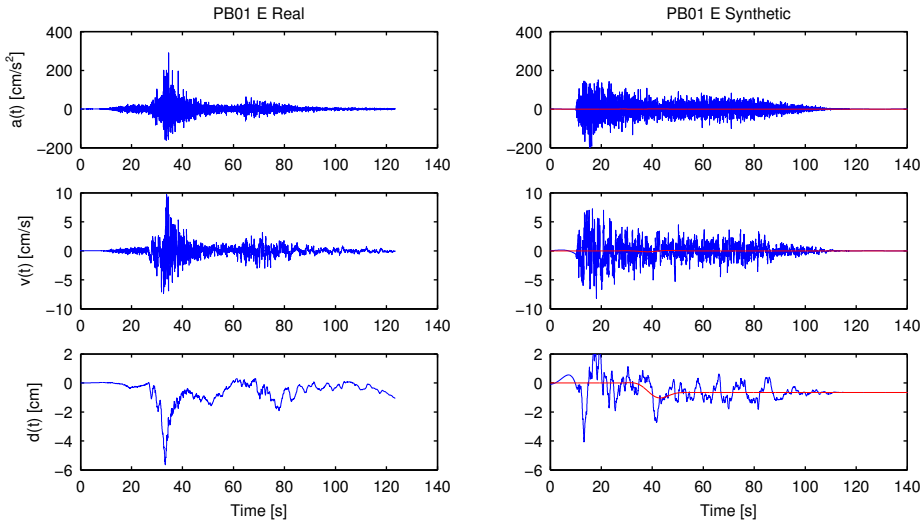

Figure D.26: Comparison simulated ground motion vs. true ground motion for station PB01 East-West component.

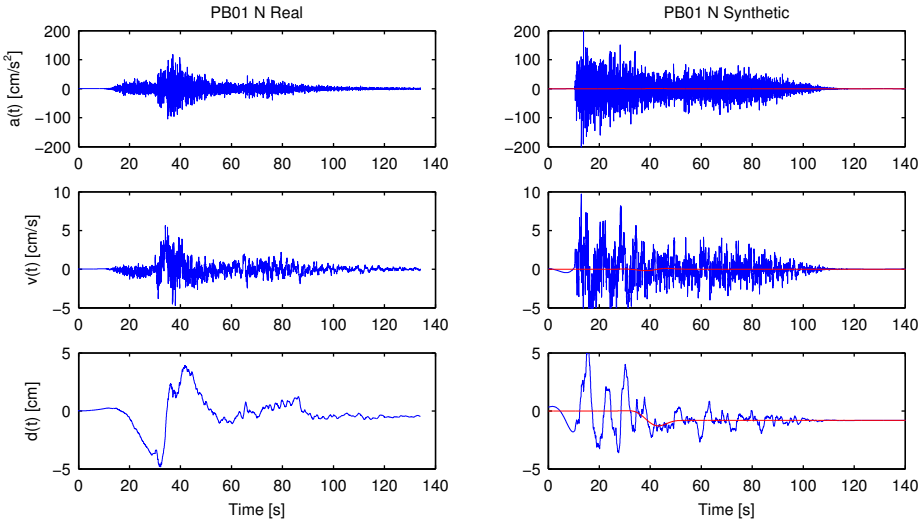

Figure D.27: Comparison simulated ground motion vs. true ground motion for station PB01 North-South component.

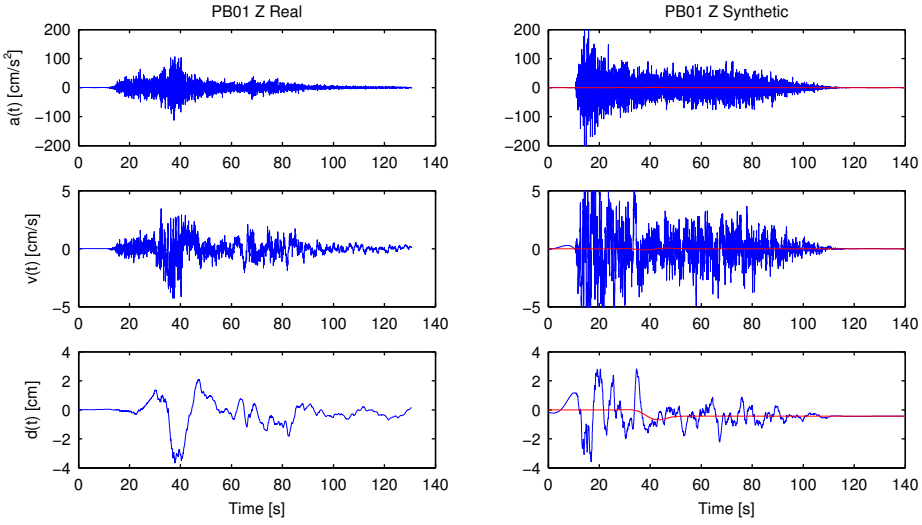

Figure D.28: Comparison simulated ground motion vs. true ground motion for station PB01 Up-Down component.

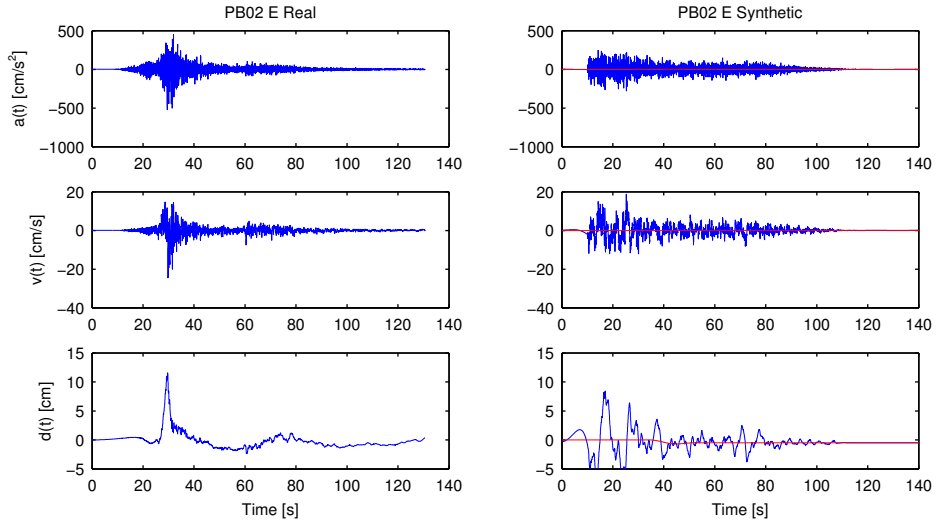

Figure D.29: Comparison simulated ground motion vs. true ground motion for station PB02 East-West component.

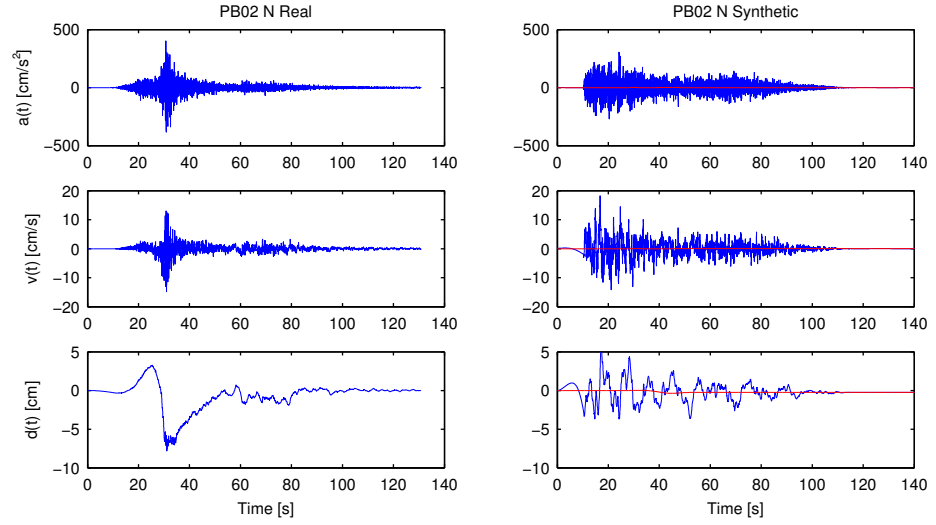

Figure D.30: Comparison simulated ground motion vs. true ground motion for station PB02 North-South component.

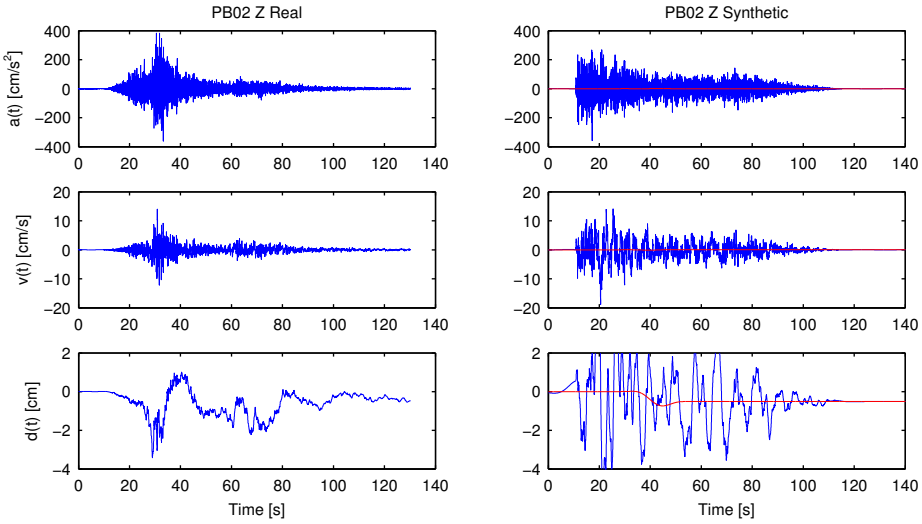

Figure D.31: Comparison simulated ground motion vs. true ground motion for station PB02 Up-Down component.

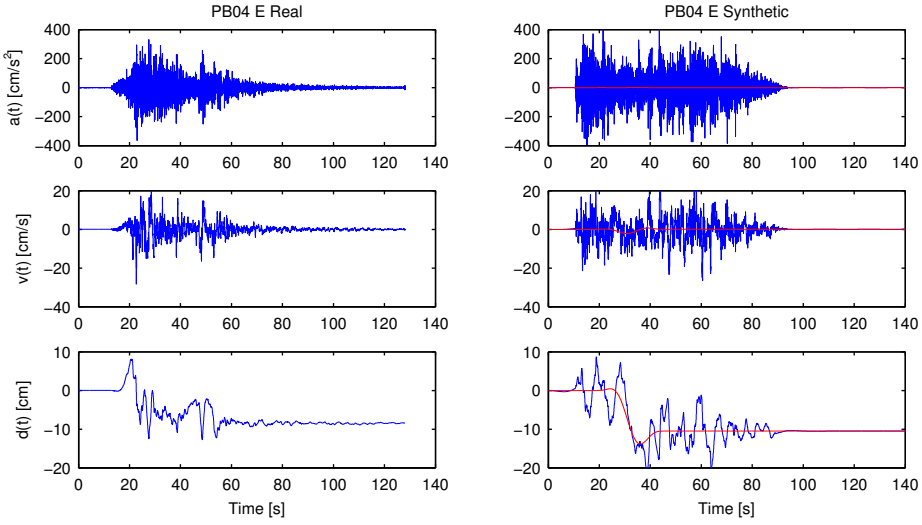

Figure D.32: Comparison simulated ground motion vs. true ground motion for station PB04 East-West component.

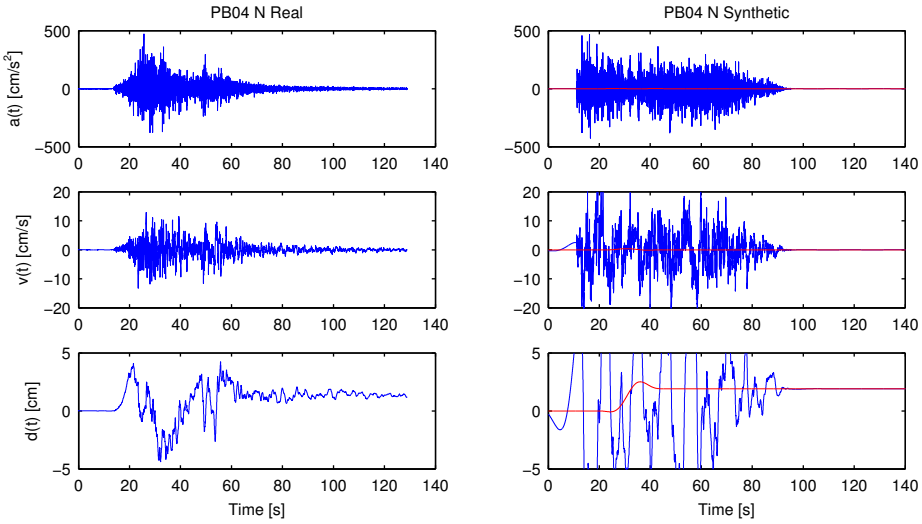

Figure D.33: Comparison simulated ground motion vs. true ground motion for station PB04 North-South component.

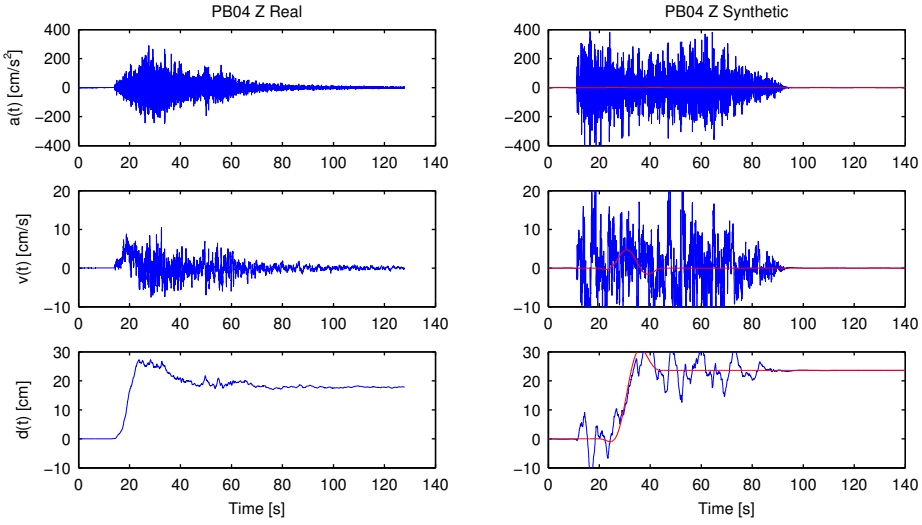

Figure D.34: Comparison simulated ground motion vs. true ground motion for station PB04 Up-Down component.

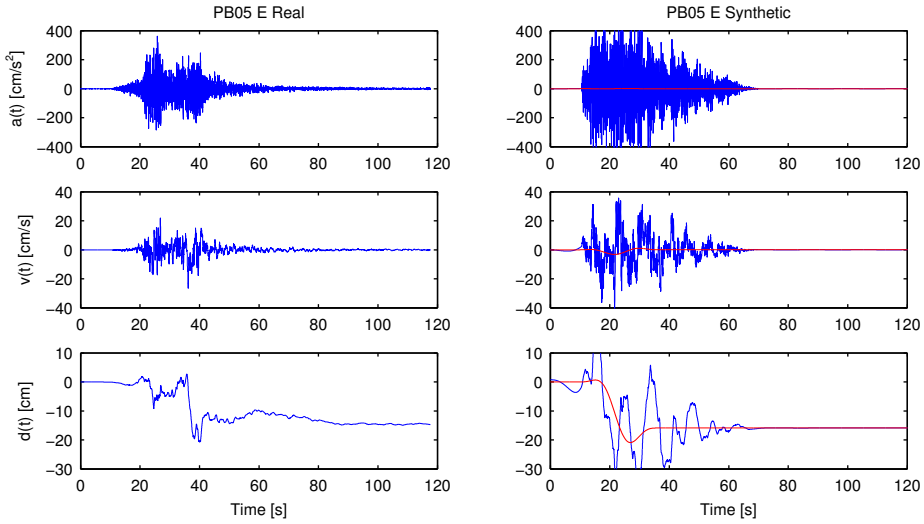

Figure D.35: Comparison simulated ground motion vs. true ground motion for station PB05 East-West component.

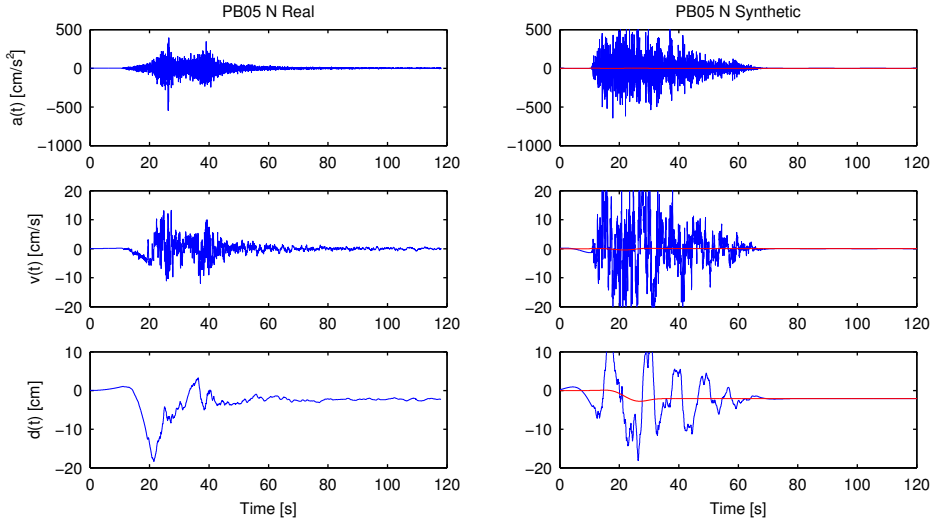

Figure D.36: Comparison simulated ground motion vs. true ground motion for station PB05 North-South component.

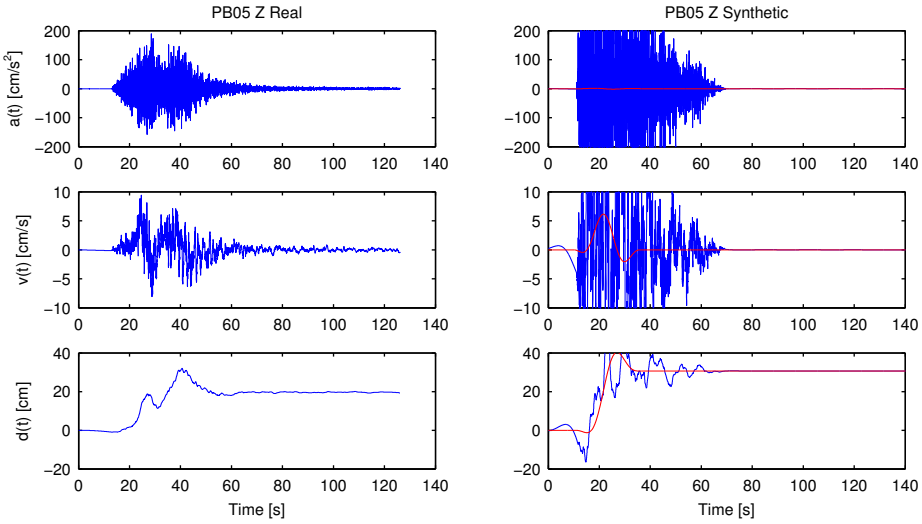

Figure D.37: Comparison simulated ground motion vs. true ground motion for station PB05 Up-Down component.

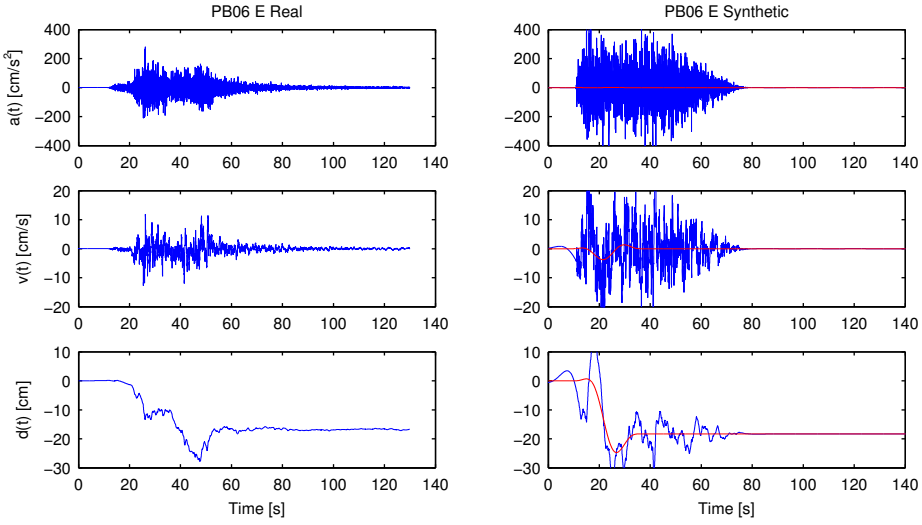

Figure D.38: Comparison simulated ground motion vs. true ground motion for station PB06 East-West component.

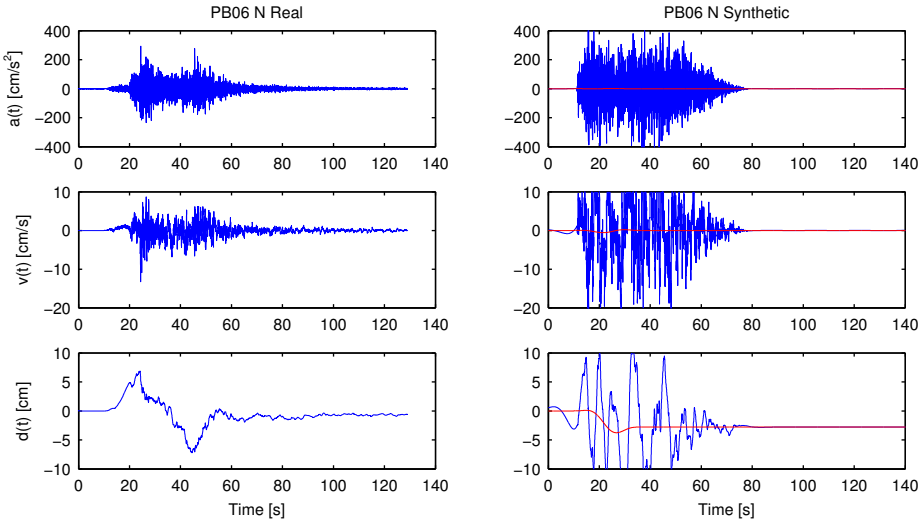

Figure D.39: Comparison simulated ground motion vs. true ground motion for station PB06 North-South component.

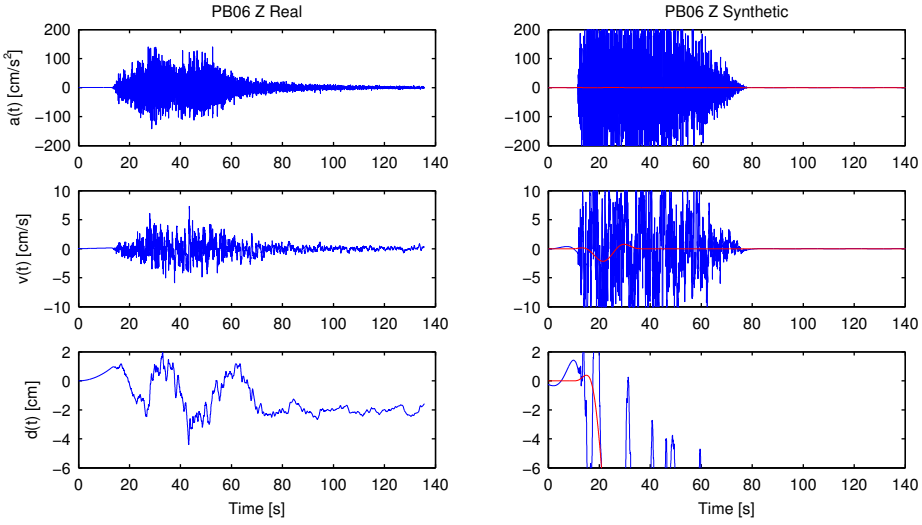

Figure D.40: Comparison simulated ground motion vs. true ground motion for station PB06 Up-Down component.

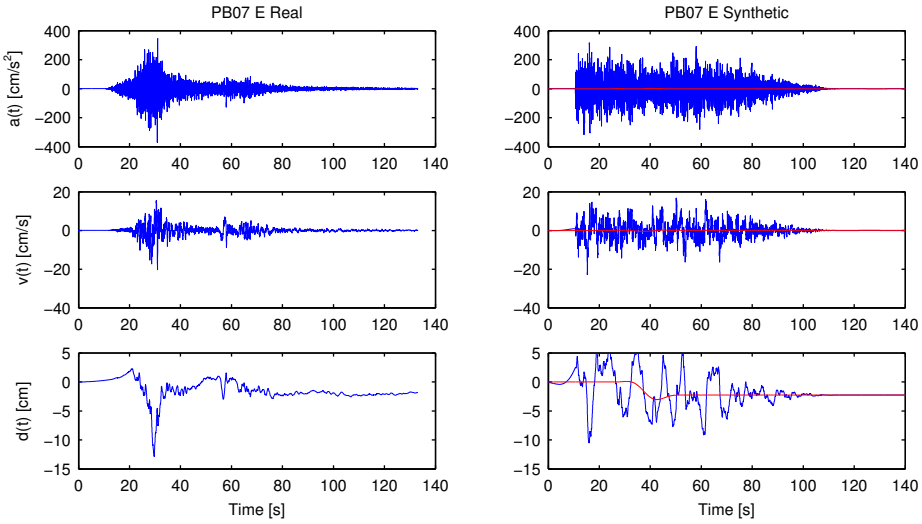

Figure D.41: Comparison simulated ground motion vs. true ground motion for station PB07 East-West component.

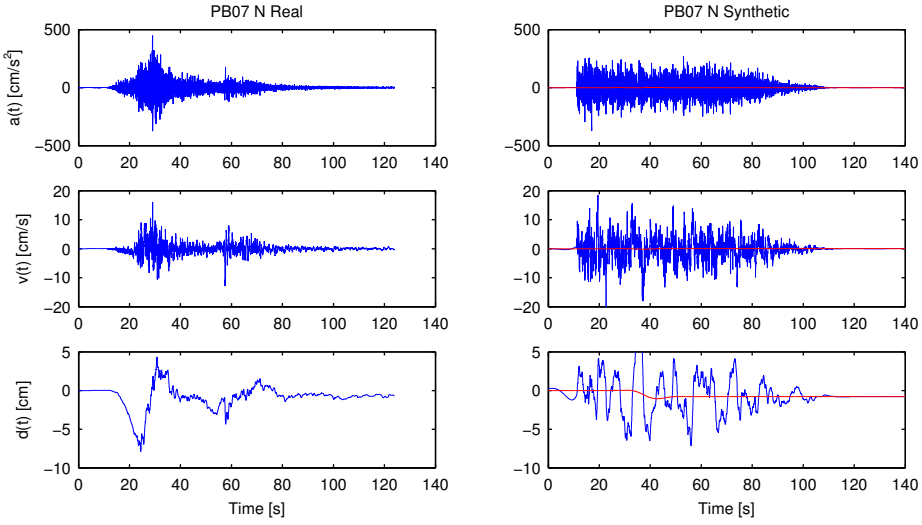

Figure D.42: Comparison simulated ground motion vs. true ground motion for station PB07 North-South component.

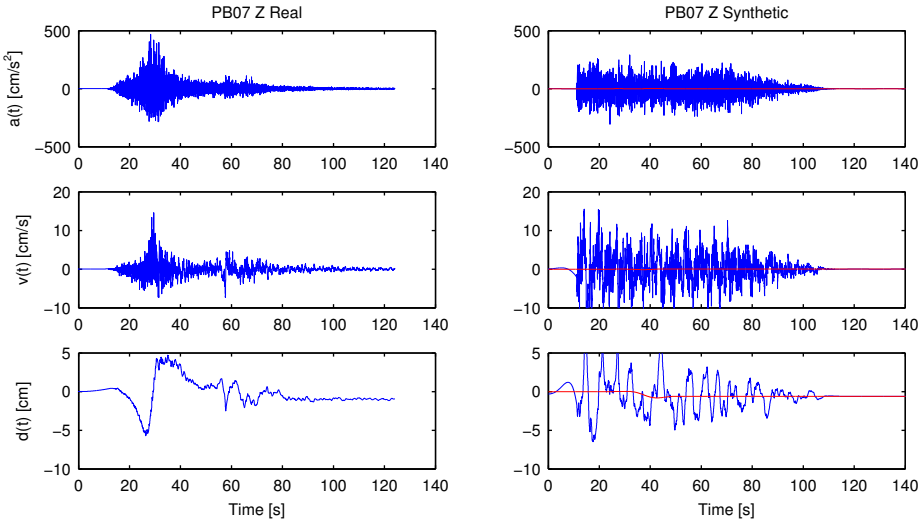

Figure D.43: Comparison simulated ground motion vs. true ground motion for station PB07 Up-Down component.

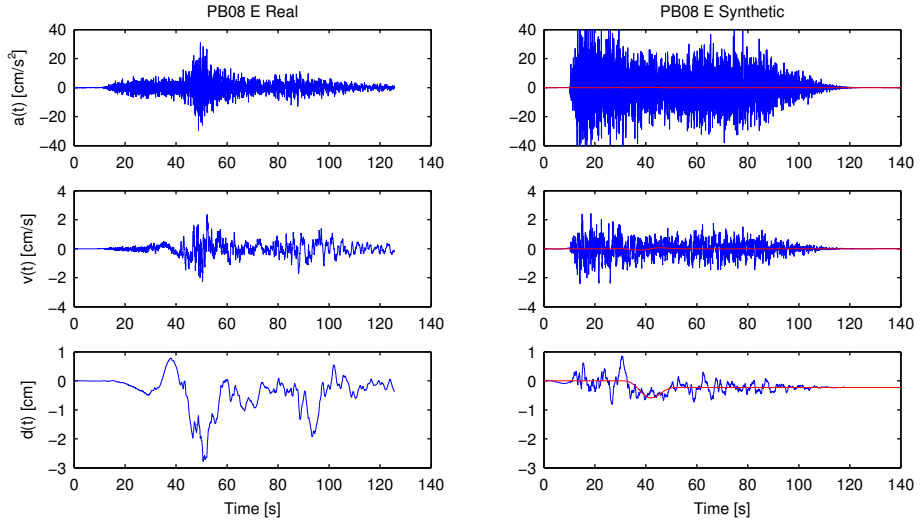

Figure D.44: Comparison simulated ground motion vs. true ground motion for station PB08 East-West component.

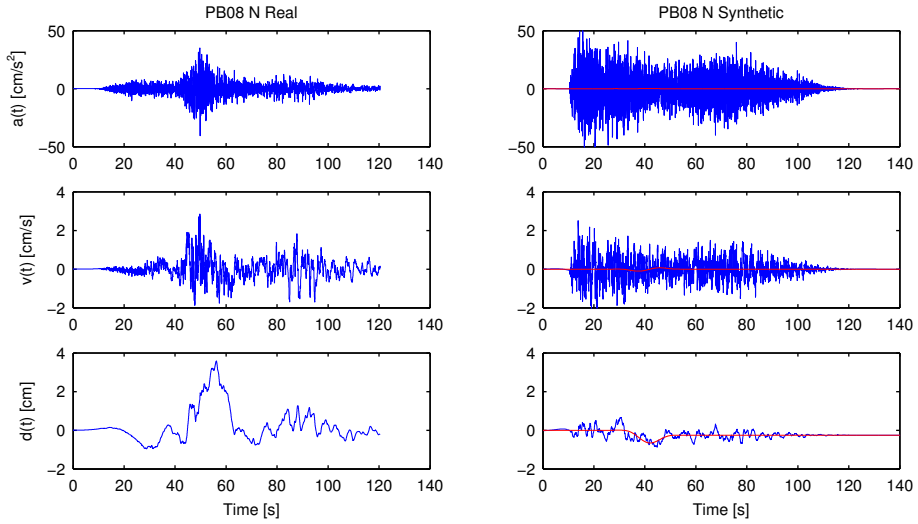

Figure D.45: Comparison simulated ground motion vs. true ground motion for station PB08 North-South component.

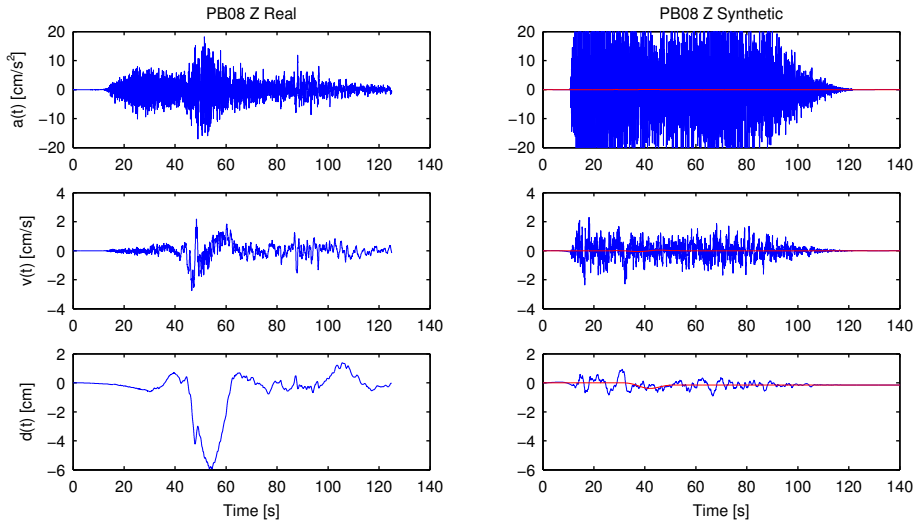

Figure D.46: Comparison simulated ground motion vs. true ground motion for station PB08 Up-Down component.

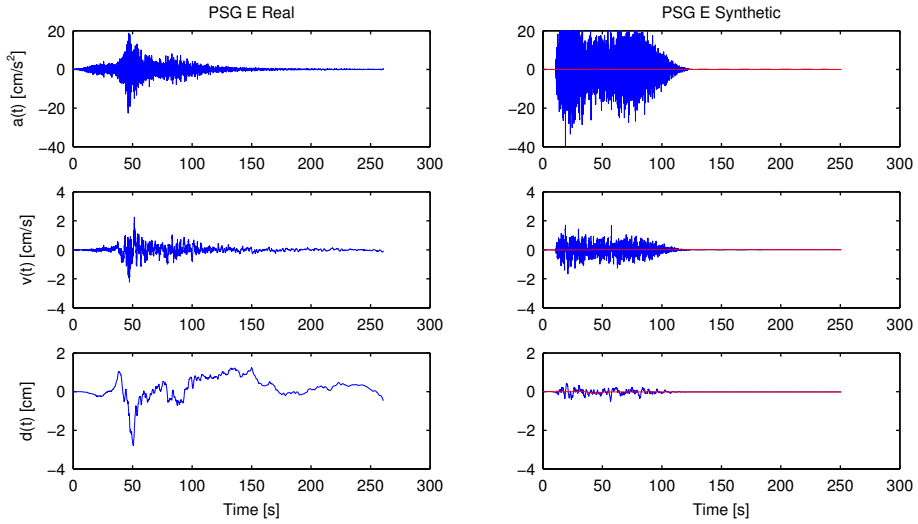

Figure D.47: Comparison simulated ground motion vs. true ground motion for station PSG East-West component.

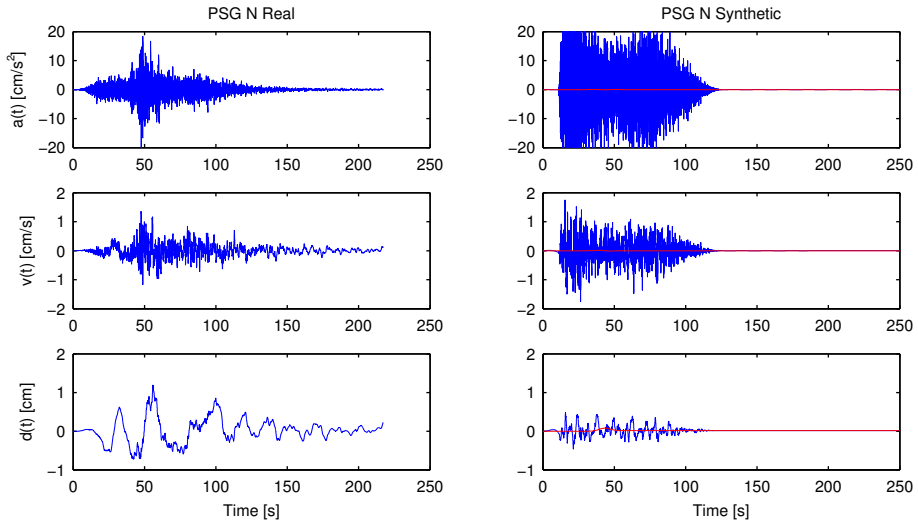

Figure D.48: Comparison simulated ground motion vs. true ground motion for station PSGCX North-South component.

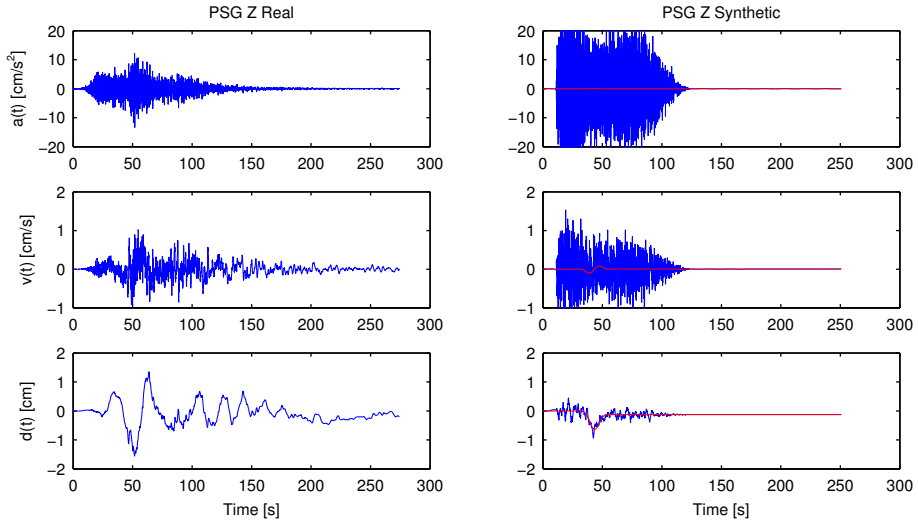

Figure D.49: Comparison simulated ground motion vs. true ground motion for station PSGCX Up-Down component.

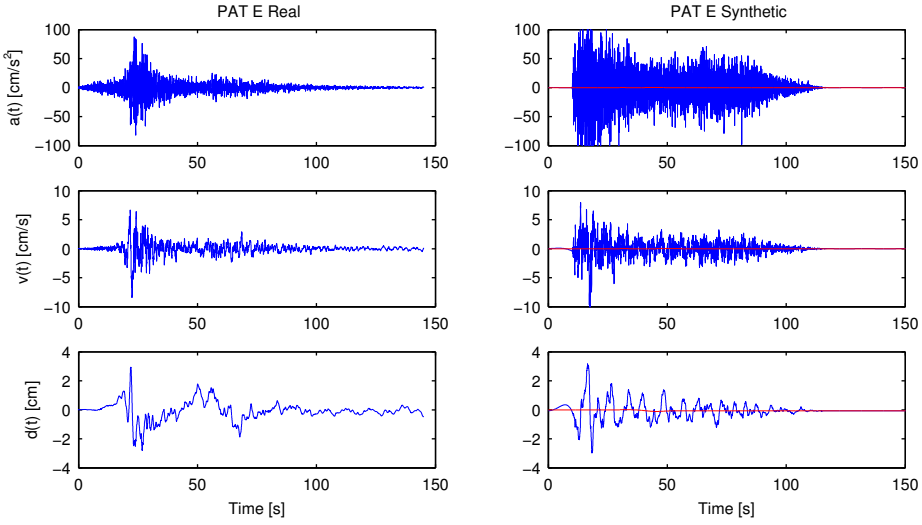

Figure D.50: Comparison simulated ground motion vs. true ground motion for station PAT East-West component.

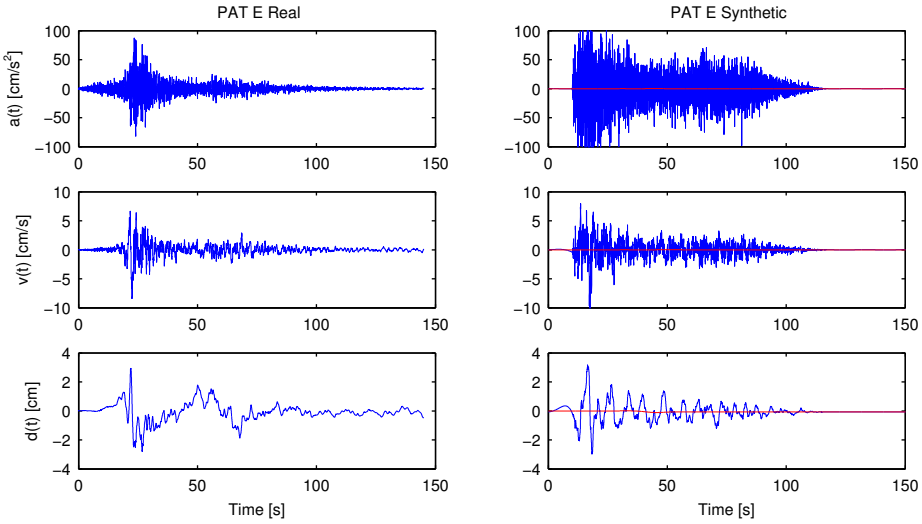

Figure D.51: Comparison simulated ground motion vs. true ground motion for station PAT North-South component.

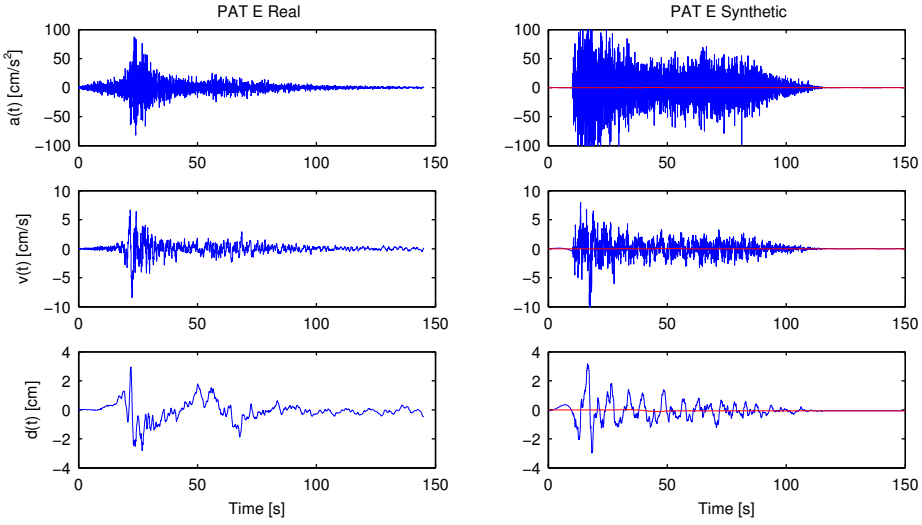

Figure D.52: Comparison simulated ground motion vs. true ground motion for station PAT Up-Down component.

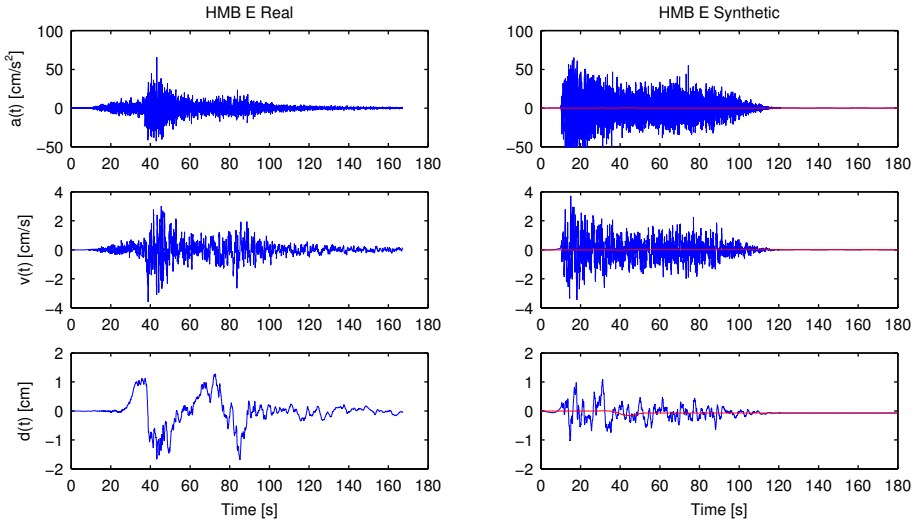

Figure D.53: Comparison simulated ground motion vs. true ground motion for station HMB East-West component.

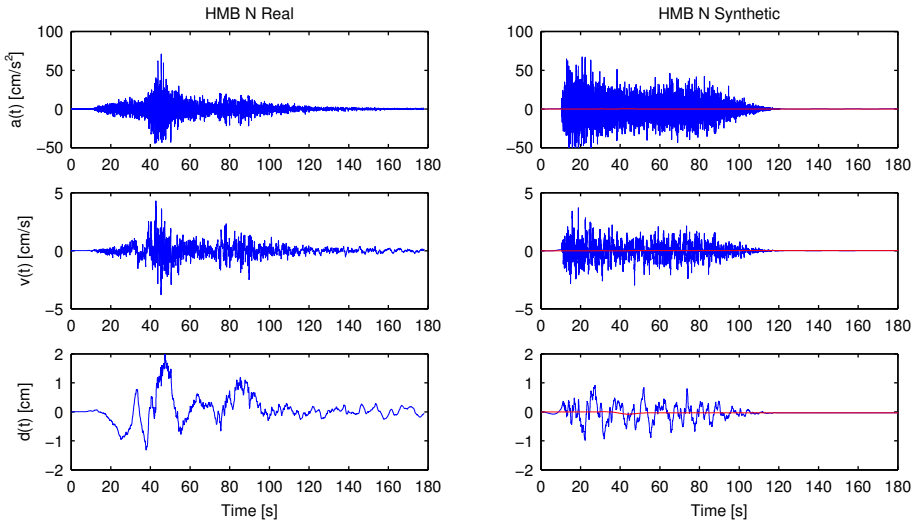

Figure D.54: Comparison simulated ground motion vs. true ground motion for station HMB North-South component.

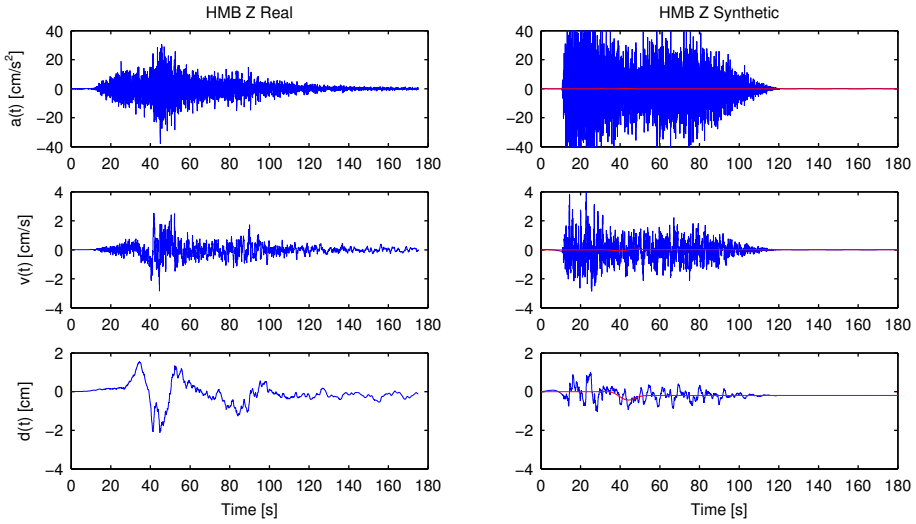

Figure D.55: Comparison simulated ground motion vs. true ground motion for station HMB Up-Down component.

D.4 Simulation Results

D.4.4 Tocopilla Earthquake: Simulated Dual Response Spectra

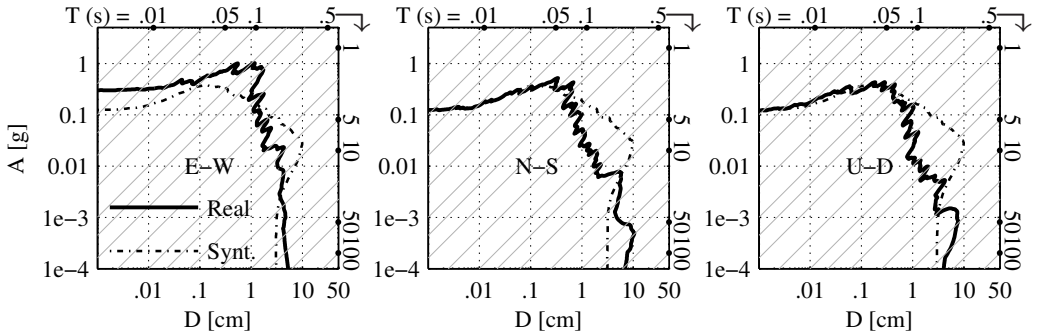

Figure D.56: Averaged simulated dual response spectrum (dotted) and true ground motion response (solid) for station PB01.

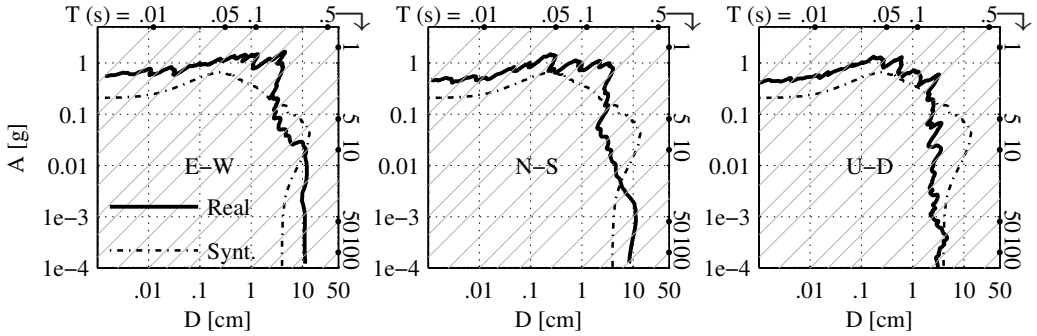

Figure D.57: Averaged simulated dual response spectrum (dotted) and true ground motion response (solid) for station PB02.

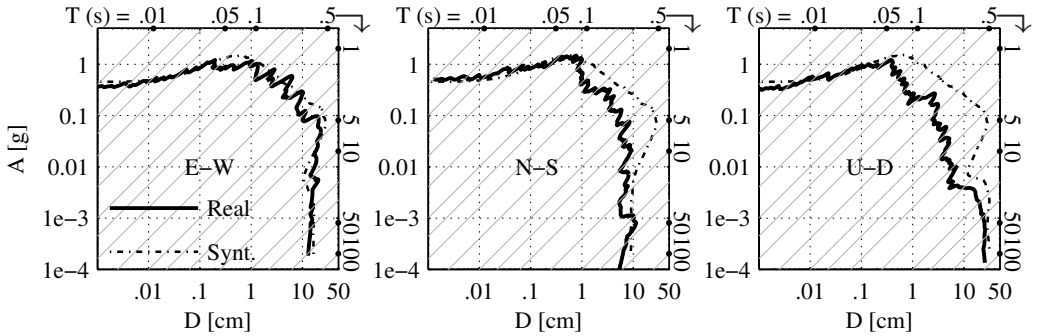

Figure D.58: Averaged simulated dual response spectrum (dotted) and true ground motion response (solid) for station PB04.

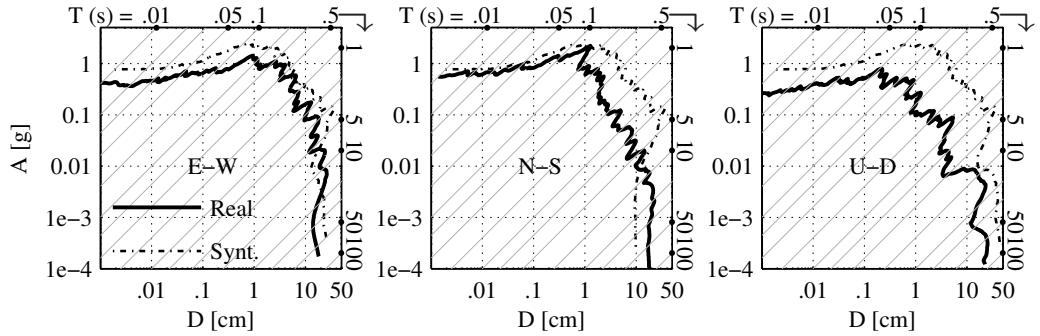

Figure D.59: Averaged simulated dual response spectrum (dotted) and true ground motion response (solid) for station PB05.

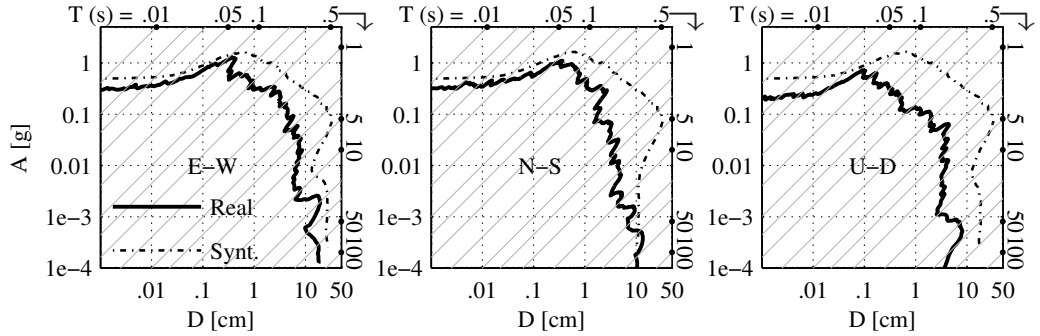

Figure D.60: Averaged simulated dual response spectrum (dotted) and true ground motion response (solid) for station PB06.

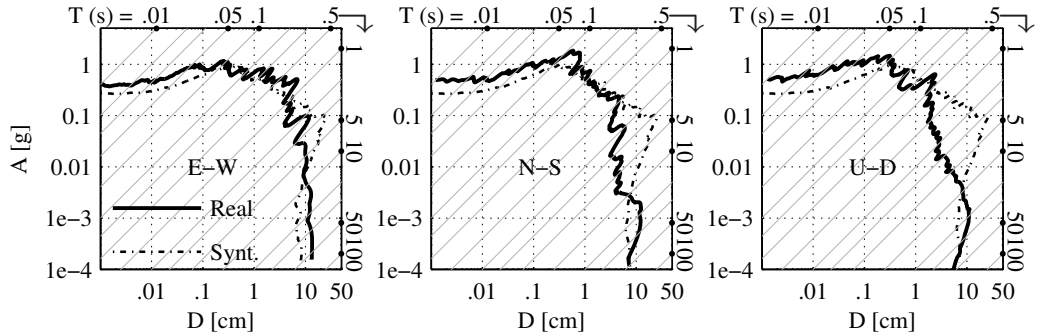

Figure D.61: Averaged simulated dual response spectrum (dotted) and true ground motion response (solid) for station PB07.

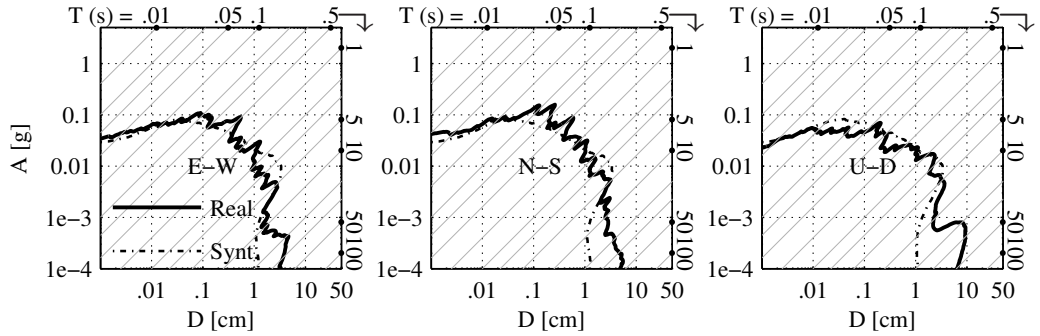

Figure D.62: Averaged simulated dual response spectrum (dotted) and true ground motion response (solid) for station PB08.

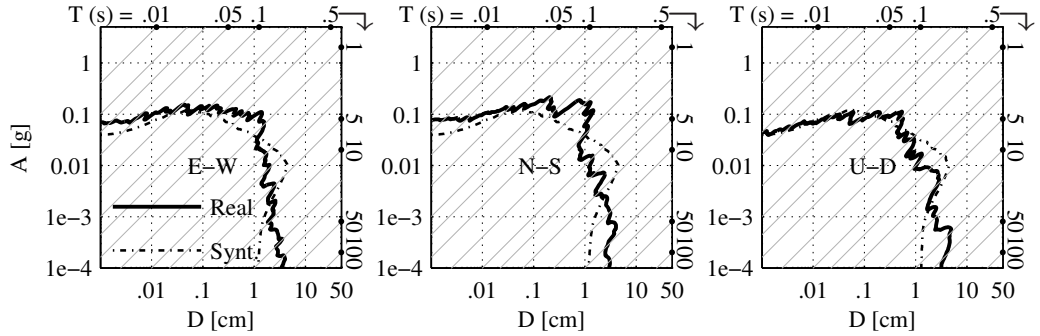

Figure D.63: Averaged simulated dual response spectrum (dotted) and true ground motion response (solid) for station HMB.

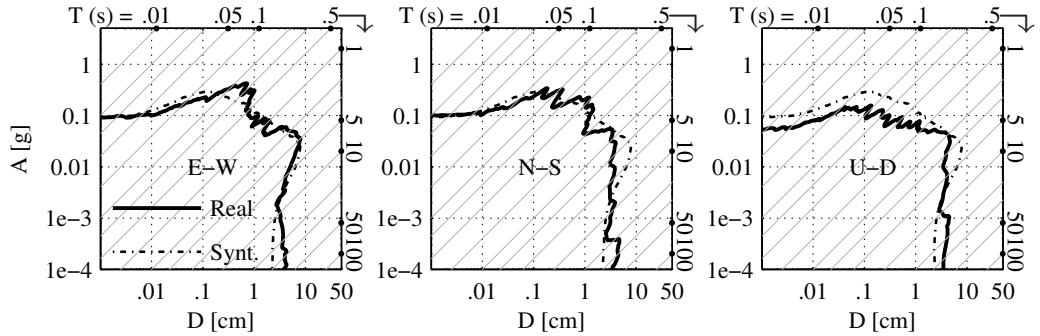

Figure D.64: Averaged simulated dual response spectrum (dotted) and true ground motion response (solid) for station PAT.

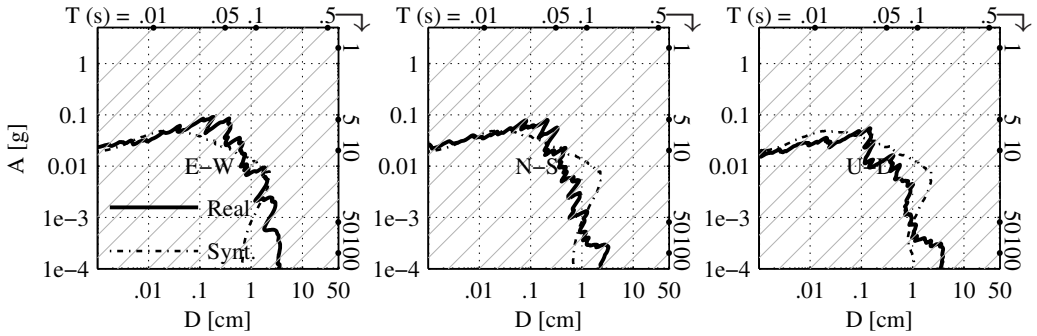

Figure D.65: Averaged simulated dual response spectrum (dotted) and true ground motion response (solid) for station PSG.

D.4 Simulation Results

D.4.5 Pisco Earthquake: Simulated Dual Response Spectra

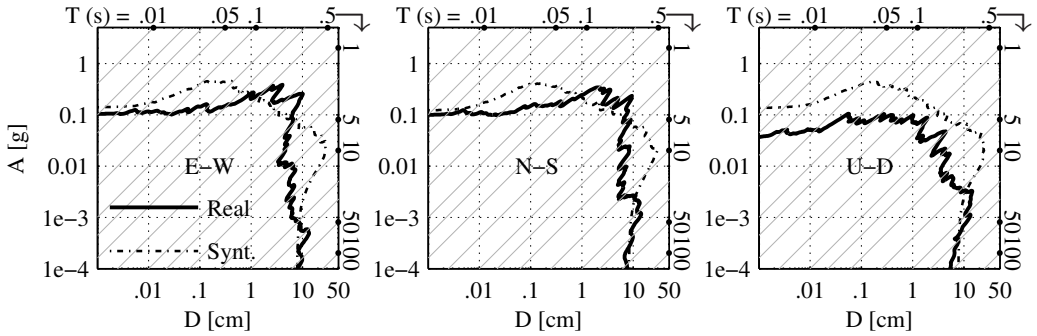

Figure D.66: Averaged simulated dual response spectrum (dotted line) and true ground motion response (solid line) for station CAL.

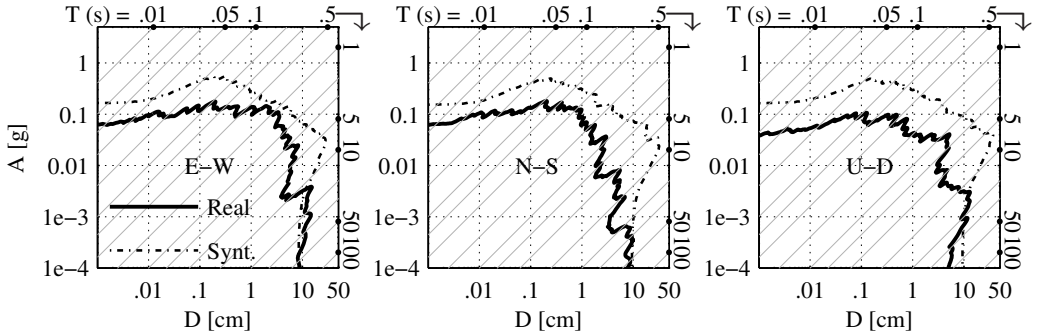

Figure D.67: Averaged simulated dual response spectrum (dotted line) and true ground motion response (solid line) for station CDLCIP.

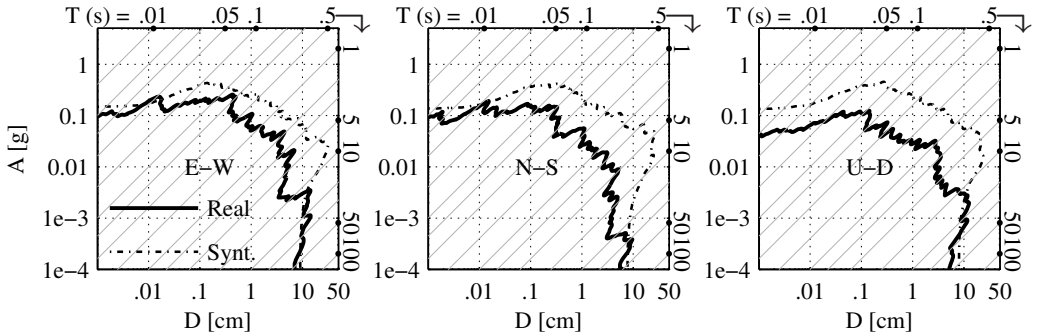

Figure D.68: Averaged simulated dual response spectrum (dotted line) and true ground motion response (solid line) for station CSM.

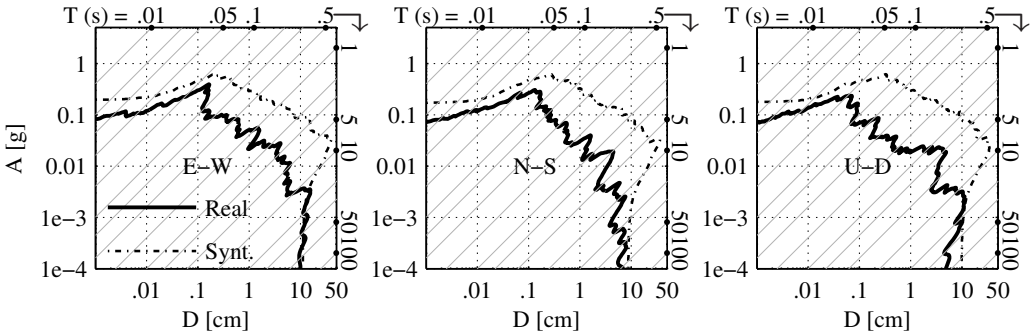

Figure D.69: Averaged simulated dual response spectrum (dotted line) and true ground motion response (solid line) for station MOL.

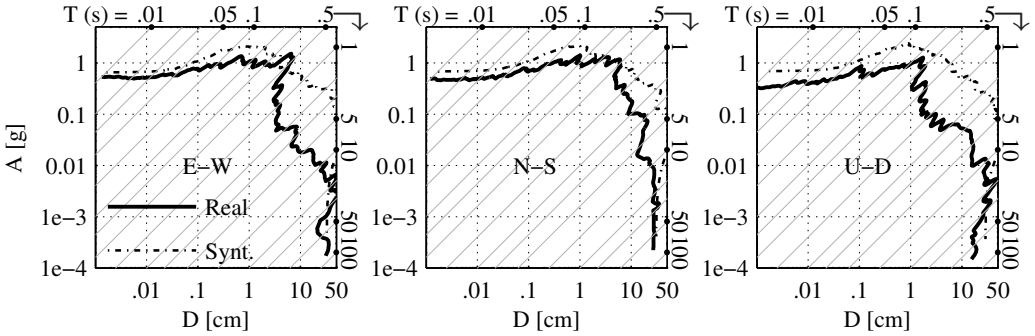

Figure D.70: Averaged simulated dual response spectrum (dotted line) and true ground motion response (solid line) for station PAR.